FFI RAPPORT

SAGNAC INTERFEROMETER FOR DIFFERENTIAL ROTATION RATE MEASUREMENT

Lasse Vines

FFI/RAPPORT-2001/05899

This page is intentionally left blank.

FFIE/793/116

Approved
Kjeller 22nd January 2002

Stian Løvold
Director of Research

SAGNAC INTERFEROMETER FOR DIFFERENTIAL ROTATION RATE MEASUREMENT

Lasse Vines

FFI/RAPPORT-2001/05899

FORSVARETS FORSKNINGSINSTITUTT
Norwegian Defence Research Establishment
P O Box 25, N-2027 Kjeller, Norway

This page is intentionally left blank.

FORSVARETS FORSKNINGSINSTITUTT (FFI)
Norwegian Defence Research Establishment
P O BOX 25
2027 KJELLER, NORWAY

UNCLASSIFIED

SECURITY CLASSIFICATION OF THIS PAGE (when data entered)

REPORT DOCUMENTATION PAGE

1) PUBL/REPORT NUMBER	2) SECURITY CLASSIFICATION	3) NUMBER OF PAGES
FFI/RAPPORT-2001/05899	UNCLASSIFIED	
1a) PROJECT REFERENCE	**2a) DECLASSIFICATION/DOWNGRADING SCHEDULE**	
FFIE/793/116		107

4) TITLE

SAGNAC INTERFEROMETER FOR DIFFERENTIAL ROTATION RATE MEASUREMENT

5) NAMES OF AUTHOR(S) IN FULL (surname first)

Lasse Vines

6) DISTRIBUTION STATEMENT

Approved for public release. Distribution unlimited (Offentlig tilgjengelig)

7) INDEXING TERMS

IN ENGLISH	IN NORWEGIAN
a) fibre optic gyroscopes	a) fiberoptisk gyroskop
b) vibration measurement	b) vibrasjonsmåling
c) light interferometry	c) interferometri

THESAURUS REFERENCE:Inspec Thesaurus 1999

8) ABSTRACT

The development of a fiber optic sensor for measurement of the differential rotation rate between two parallell axis is reported. Different designs based on the Sagnac Interferometer are considered, and a design for use in hull monitoring systems are recomended and demonstrated with the use of two standard interrogation techniques for optical gyroscopes. The recomended design consists of two fiber coils connected in series in a way such that light waves propagating in one direction in one coil, will propagate in opposite direction in the other coil. Since the two coils are connected by optical fiber, the sensor system are designed to measure oscillations or vibrations. The rotation rate sensor is insensitive to rotations equal for the two coils. The application at hand is measurement of vibration modes(e.g torsion) for use in hull monitoring systems in large sized objects such as ships and airplanes, where the amplitude of torsion oscillations indicates the load of the object.

9) DATE	AUTHORIZED BY This page only	POSITION
22nd January 2002	Stian Løvold	Director of Research

ISBN-82-464-0575-6

UNCLASSIFIED

SECURITY CLASSIFICATION OF THIS PAGE (when data entered)

This page is intentionally left blank.

CONTENTS

PAGE

SAGNAC INTERFEROMETER FOR DIFFERENTIAL ROTATION RATE MEASUREMENT

1 INTRODUCTION

1.1 Background

A gyroscope measures angular velocity, and is an important component in many stabilizing units and in navigation systems. They are used in a wide range of applications, from navigating floor cleaning robots in shopping malls to navigation support in aeroplanes such as Boing 777 and stabilization of rocket missiles.

The first gyroscopes built were mechanical. They usually take the form of a disc shaped object with a large, heavy rim. The disc is spun on its axis at high speed and will, according to Newton's laws, resist movement in certain directions. This resistance is measured.

The effect that gave rise to the optical gyroscope was discovered in 1913 by Sagnac [1]. The principle is that two ligthbeams moving in opposite directions in a closed loop will experience different path length of one lap if the system is rotating. The Sagnac effect is very small, so when it was discovered, it was not usable for any practical application. The invention of the laser enabled the Sagnac effect to be detectable however. The development of the optical gyroscope had started. When the optical fiber was invented, a new type of optical gyroscope started its development, the fiber optic gyroscope.

One of the main advantages of the optical gyroscope compared to its mechanical counterpart is the absense of rotating parts. This makes the optical gyro potentially longer lasting. The optical gyro can also be designed to detect the dynamic range of interest by for example varying the length of the fiber. One of the most promising designs was the interferometric fiber optic gyro, I-FOG, and its development followed the advances in components lead by the telecommunication industry.

Fiber optic gyroscopes are mainly used for navigation and stabilization purposes. In this thesis however, the gyroscope is used for a different application. In health monitoring of the ship hulls one measures how the hull of the boat bends in the water in different sea states. Strain sensors are normally used for this application, and some fiber optic systems based on Bragg gratings have been developed [2], [3]. It would be very usefull however, if one could measure the torsion angle of the hull directly, and this is the motivation for this thesis.

The idea is to put a fiber optic gyroscope in each end of a ship, and look at the difference between these two. This difference is equal to the difference in rotation rate, which is the derivative of the torsion angle. The angle obtained after integration of the rotation rate is the torsion between the two points where the sensors are located. A problem finding the torsion angle is that the entire boat moves in the water which gives a rotation. The hope is therefore to retain a small differential rotation signal buried in a large common rotation (a rotation equal for the two sensors/gyroscopes).

The system developed can of course be applied to other areas than health monitoring of the hull in ships. The concept can be used in applications where one wants to find a relative rotation between two planes, and this rotation is limited (for example to 360^o). One example is in rotating antennas (especially when they are mounted on moving objects), where the rotation compared to the ground (or moving object) is crucial.

This thesis is organized in the following way. At the end of this chapter, a overview of the final system which was the result of this work is given. Chapter 2 reviews theory of the differential gyroscope and its application in structure monitoring. Chapter 3 contains the experimental part of this thesis, while the results are given and discussed in chapter 4. At the end of chapter 4, recommendations for further development are made. Basic theory for the components used in the experiments and which are important for understanding the operation of the differential gyroscope, are discussed in appendix A.

A literature study on differential gyroscopes showed little activity on the subject. Mochalov et. al. [4] have used two ordinary laser gyroscopes in monitoring the deviation between two points on large sized moving objects, but they did not build the optics around a differential study.

1.2 Definition of terms used in this thesis

Some words will be used with a particular meaning in this thesis, and will be defined here. First of all, rotation rate will in this text have the same meaning as angular velocity. By “common mode” (rotation) is meant rotation that is equal in the two sensor coils. If the word “differential gyroscope” is used, it should be understood here as a sensor measuring the difference in angular velocity between two points. With the word “stable-bias” we mean the configuration where a specific modulation techique is used. Similarily, for the term “3x3 demodulation”, which it should be read as the configuration involving a 3x3 coupler and its demodulation technique. When “spool” is used, the physical spool without fiber is meant, while when “coil” is used, it means the spool with fiber wrapped around it.

1.3 Overview of the selected gyro concept

In this section, the system developed is descibed briefly, to give a better overview when reading the theoretical and experimental part. Details can be found in chapter 2.

The sensor part of the fiber-optic gyroscope mainly consists of fiber wrapped around a cylinder. Light propagates in both directions in the coil. If the coil is at rest in an inertial frame of reference, the counterpropagating light will use equal amounts of time through the coil. At the output the two beams will interfere constructively. If the coil is rotated, the light propagating against the rotation will use shorter time through the fiber coil than the light propagating in the same direction as the rotation. The time difference of the counterpropagating lightwaves is proportional to the rotation rate. At the output the two counterpropagating waves will interfere, and the interference equation will have the form [5]

$$I = A + V \cdot \cos(\Delta\phi_R + \varphi) \ , \ \Delta\phi_R = \frac{2\pi LD}{\lambda_0 c_0}\Omega \tag{1.1}$$

where A is a constant, V is the visibility, $\Delta\phi_R$ is the induced phase shift proportional to the angular velocity (see Appendix A.1), L is the length of the fiber coil, D is the diameter of the fiber coil, λ_0 is the wavelength used, c_0 is the speed of light in vacuum, Ω is the rotation rate, and φ a phase constant ($\varphi = 0$ in the 2x2 setup and $\varphi = \frac{2\pi}{3}$ for the 3x3 setup).

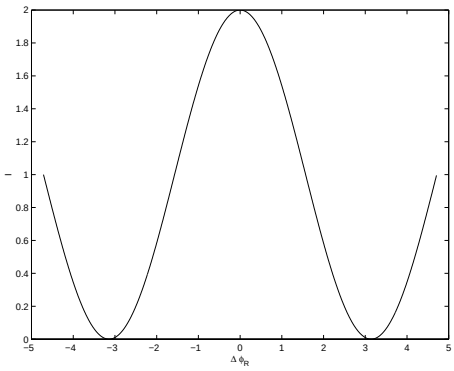

Figure 1.1: Simple graphical representation of the interference equation. $I = V = 1$

The interference curve is given as a raised cosine curve (Figure 1.1). Consequently, the difference in output signal is very low for low rotation rates (when $\varphi = 0$). To operate the system at a point where a small angular velocity gives a larger signal response (the quadrature point) a modulation of the light has to be applied. One such modulation/demodulation technique is described in section 2.2.

The motivation for this sensor is finding the torsion angle in ships. If two rotation sensors are aligned compared to each other as illustrated in Figure 1.2.A, they will both experience a rotation due to rigid body motion of the boat. If the boat were totally rigid, this rotation would be equal in the two sensors, but if torsion exist, there will be a difference between the two sensors, and this thesis aims at developing a sensor which can measure this differential rotation.

After some preliminary investigations, a serial configuration of the sensor described above was chosen. In Figure 1.2.B, the coiling direction of the fiber are shown schematically. The connecting fiber (Fiber 1,2 and 3) must be close together to avoid a Sagnac interferometer from these fibers, but this is not shown in the figure (see section 2.3). In Figure 1.2.A the orientation of the coils with colinear axis for torsion measurement is shown. The type of illustration shown in Figure 1.2.B will be given throughout this text, since it gives a better picture of the design of the system, but the reader should keep in mind the 3D alignment shown in Figure 1.2.A.

The idea is that light propagating in the clockwise direction in one coil, is propagating in the counterclockwise direction in the opposite coil. This compensates for the rotation which is common to both gyroscopes, and the differences in rotation is consequently the only rotation that gives rise to the time difference described above.

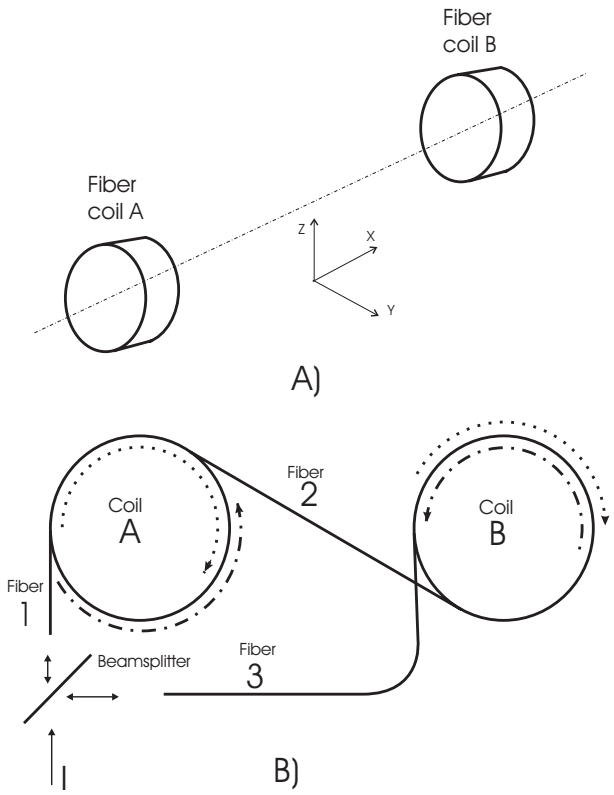

Figure 1.2: A) 3D view of the alignment of the two sensor coils. B) 2D representation of the serial configuration

To retrieve the rotation signal, different approaches have been used. The two most common is the open loop “minimum configuration” and a closed loop configuration shown in Figure 1.3. For the open loop approach, a fixed modulation frequency and amplitude is applied, and the signal is retrieved by synchronous detection. The closed loop configuration uses a feedback to the modulator to obtain maximum response for all rotation rates. This approach is not persued in this text, as it is a relatively expensive method. The reason for using two couplers is that only the input port is reciprocal (see Appendix A.2).

For low to medium performance gyroscopes, a configuration with a 3x3 coupler instead of two 2x2 couplers is becomming increasingly more common. This design is shown schematically in Figure 1.4

The two fiber coils work as in the example above, but the two 2x2 couplers are replaced by a single 3x3 coupler. In this setup, no modulation is needed, because here the interference pattern naturally varies around the quadrature point, the point where the response is highest for low angular velocities (section 2.2). This means that the configuration is all passive, which is an advantage in terms of simplicity and cost.

In conclusion, two modulation/demodulation techiques have been pursued with the serial configuration (both theoretically and experimentally); the open-loop minimum configuration (later called stable bias modulation) and the passive demodulation using a 3x3 coupler.

The system has been developed and demonstrated with both demodulation techniques.

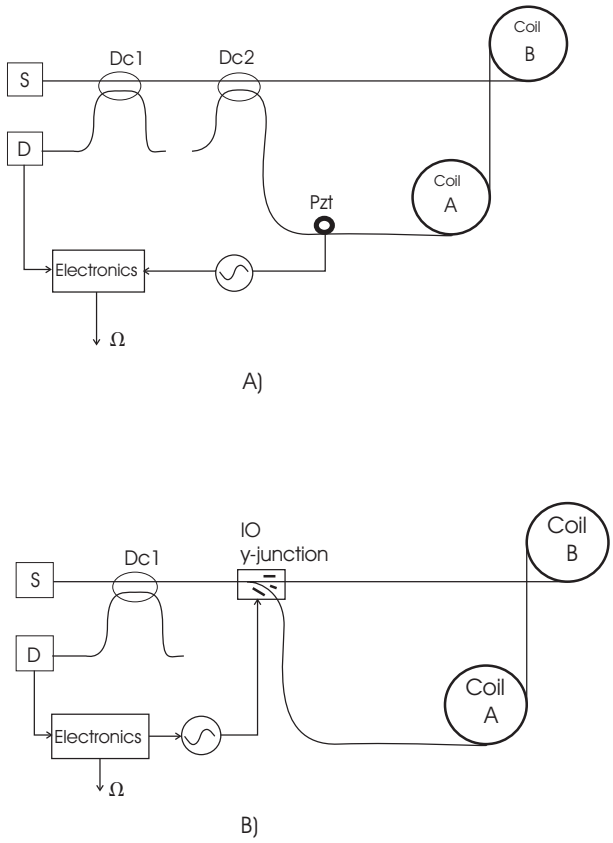

Figure 1.3: A) Example of open loop configuration B) Example of closed loop configuration. The S in the figure represent the source, the D represent the detector, and Dc represent the directional coupler

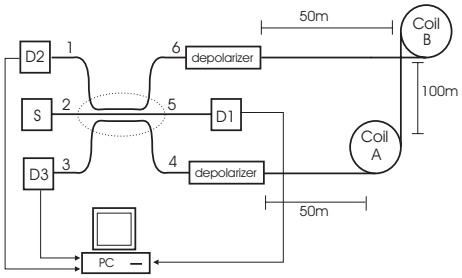

Figure 1.4: Example of differential gyroscope with a 3x3 coupler

Furthermore, the modulation strategies have been compared.

As mentioned earlier, the application motivating this development is monitoring the torsion angle in large sized objects such as vessels as part of a structure monitoring system. Some ideas about how the differential gyroscope will operate have consequently been followed up. Estimates show that vertical bending of a ship might limit the performance.

2 THEORY OF THE DIFFERENTIAL GYROSCOPE

2.1 The Sagnac effect

In Appendix A.1 the Sagnac effect is discussed. When two counterpropagating waves propagate in a circular disc/path, they will experience a different length of the path if the disc is rotating. This difference in length result in a difference in phase when the waves interfere at a common output. The difference in phase $\Delta\phi_R$ are given by

$$\Delta\phi_R = \frac{2\pi L \cdot D}{\lambda_0 c_0}\Omega \tag{2.1}$$

where L is the length of the disc/path at rest, in this case the length of the fiber, D is the diameter of the disc, λ_0 is the wavelength of the light, c_0 is the speed of light in vacuum, and Ω is the angular velocity or rotation rate of the disc. The disc is in this text a coil of fiber.

The phase difference is consequently proportional to the rotation rate. It is important to notice that the length L, the diameter of the coil D, and the wavelength λ_0 can be changed to reduce or increase the sensitivity to the rotation rate. From this it follows that the dynamic range can be changed to fit the application of interest.

An alternative way to write the formula in equation 2.1 is

$$\Delta\phi = \frac{8\pi N \cdot A}{\lambda_0 c_o}\Omega \tag{2.2}$$

Here, A is the area of the coil, and N is the number of turns of fiber. The equation states that the Sagnac effect is proportional to the effective area of the coil ($N \cdot A$).

Another important factor in the Sagnac interferometer is the reciprocity, and is discussed in appendix A.2. The idea is that the two counterpropagating waves propagate in the same fiber. Effects changing the phase of the light will consequently change both waves equally, and only nonreciprocal effects will be detected as a phase difference at the output. To obtain total reciprocity, the Sagnac interferometer must use the same port as both input and output port. To accomplish this, two 2x2 directional couplers are connected in series.

2.2 Different designs

In this thesis, three different setups have been proposed and investigated. A first question is the degree of integration between the two sensor systems (one for each coil). In one end of this range one has two fully separated gyroscopes where the output rotations are electronically differentiated. Mochalov et. al. has persued this idea [4]. On the other hand, one might also construct a differential gyro where everything but the rotating coils are shared.

One idea behind the project was to design the sensor system specially for the measurement of the torsion angle. This made the use of two separate gyroscopes less attractive.

Three representative designs are investigated and compared, to conclude which design is more suited for measuring torsion angles.

2.2.1 Fourwave interferometry

It would be very advantagous if it were possible to extract the phase-delay due to differential rotation directly. One idea was to let the signals from the two coils constituting the gyroscope interfere. One setup is shown in Figure 2.1

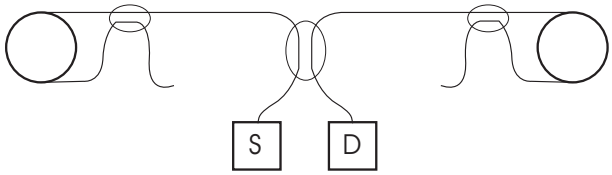

Figure 2.1: Possible configuration of a differential gyroscope

The problem is that we get interference from four waves instead of two, two directions in two coils. The signal at the output becomes (see appendix B for derivation)

$$I_{tot} = A^2(4 + 2cos(\Delta\phi_c) + 4cos(\frac{\Delta\phi_d}{2}cos(\theta)) + 4cos(\Delta\phi_c + \frac{\Delta\phi_d}{2})cos(\theta)$$
$$+2cos(\Delta\phi_c)cos(\Delta\phi_d) - 2\sin(\Delta\phi_c)\sin(\Delta\phi_d))$$

Here, A is a constant dependent on the input power, $\Delta\phi_c$ is the Sagnac phase shift induced by common mode rotation, $\Delta\phi_d$ is the Sagnac phase shift induced by differential rotation (torsion). From this result it follows that it is not trivial to separate the common and differential rotation with the proposed setup. The differential rotation will be buried in the common mode rotation, the latter several orders of magnitude larger than the former. If the common mode has different frequencies than the differential rotation, it might be possible to retrieve the differential rotation with proper use of modulation and signal processing techniques, but this has not been investigated.

2.2.2 Differential gyroscope with multiplexing

The setup above (Figure 2.1) can also be used such that four wave interference is suppressed or the four wave interference is neglible. If the signals from the two Sagnac interferometers are separated in some way (i.e. in time), one can retrieve the signals from each interferometer by using an appropriate demodulation technique. The differentiation will then be done using electronics.

There are several ways to separate the signals. One of the simplest methods is using a pulsed source, and having different overall fiberlength in each sensorcoil, so that the

returning lightwaves arrive at the detector at different times. This is called time division multiplexing (TDM). A second method is wavelength division multiplexing, but since broadband sources are commonly used in gyroscopes, this method turns out to be quite complex, and induces a lot of crosstalk. A third method assumes the use of a stable bias modulation/demodulation technique. The idea is to use different modulation frequencies, and then separate the interference signals by the use of proper electronic filtering in the detection circuit. Here, one still has four wave interferometry, but one of the signals will dominate at the modulation frequency. A multiplexing method closely related to the last method is to simply turn the modulation on and off in certain intervals. This is a form of TDM. There are also some multiplexing methods for a closed loop operation of the gyroscope, but they will not be dealt with here [6].

The use of the techiques described above requires some electronics, but reduces the cost by sharing source, detector and some electronics.

With the use of time division multiplexing, the two signals that are subtracted will be slightly separated in time, and this will introduce errors. However, this time delay between the two sensors will be neglible compared to the expected rotation rate.

A problem with this approach is that the total rotation is measured, and not only the differential rotation. This requires high dynamic range sensors, since one might have to extract a 1mrad amplitude from a total rotation amplitude of 0.1 rad (crude estimate). One possible solution for enhancing the dynamic range may be to count the interference fringes. The Phase Generated Carrier (PGC) modulation/demodulation technique would be interesting here.

2.2.3 Serial configuration

Another possibility is to connect the two sensor coils as outlined in the introduction. This reduces the system to a single interferometer, and consequently simplifies the configuration substantially. The idea is that by interchanging the input and output fibers in one of the two coils, phase shift due to common rotation (common mode) should cancel each other out optically in the two coils and consequently give no rotational signal. This is done by letting the light that propagates in the clockwise direction in one sensor coil, propagate in the counterclockwise direction in the other sensor coil, and vice versa. This is illustrated in Figure 2.2. The coils in the figure have been rotated 90^o to make the configuration easier to illustrate. The two coils should be aligned in space as illustrated in Figure 1.2.A in chapter 1.

Incoming light from point I_0 that first enters coil A will experience a total phase shift when it has returned to point I_0 of

$$\Phi_1 = \phi_t + \phi_1 + \phi_{1a} + \phi_2 + \phi_{2b} + \phi_3 + \phi_r \tag{2.3}$$

and the light first entering coil B

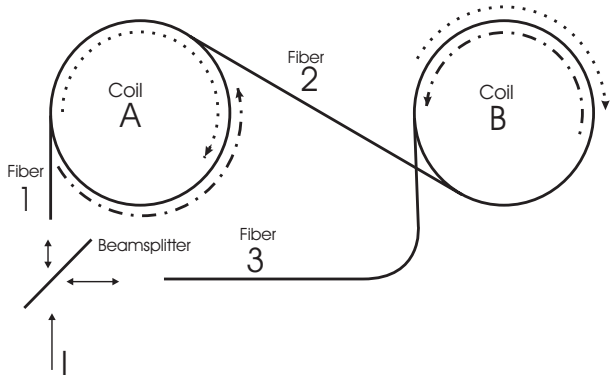

Figure 2.2: Possible setup of a differential gyroscope using a serial configuration

$$\Phi_2 = \phi_r + \phi_3 + \phi_{1b} + \phi_2 + \phi_{2a} + \phi_1 + \phi_t \tag{2.4}$$

where ϕ_i (i=1,2,3) is the phase difference due to fiberlength i, ϕ_t and ϕ_r are phase shifts due to transmission and reflection through the beamsplitter respectively, and ϕ_{1a}/ϕ_{1b} are the phase shifts the clockwise propagating lightwave experience in coil A/B, propagation in the same direction as the rotation of the coil. The phase shift the lightwave propagating in counterclockwise direction experience in coil A/B, is denoted ϕ_{2a}/ϕ_{2b}, propagation in the opposite direction of the coil rotation. Clockwise and counterclockwise rotation is illustrated in Figure 2.3, where the two coils have been placed on top of each other

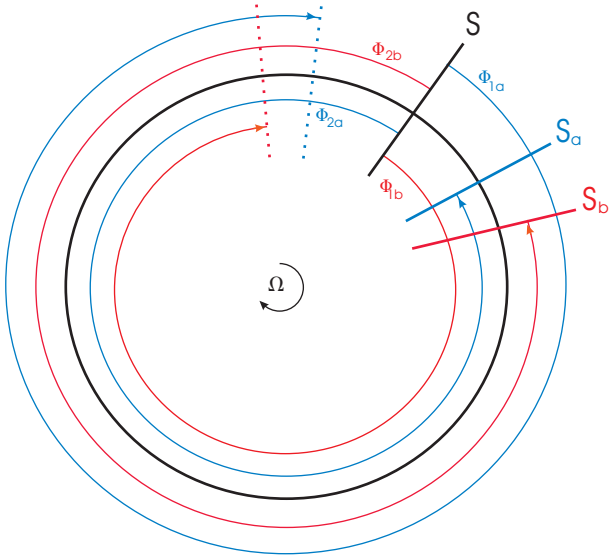

Figure 2.3: Simplified model of two Sagnac interferometers in series (put on top of eachother

The difference in phase shift in the two counterpropagating waves becomes

$$\Delta\phi = \Phi_1 - \Phi_2 = \phi_{1a} + \phi_{2b} - \phi_{1b} - \phi_{2a} = \Delta\phi_b - \Delta\phi_a \tag{2.5}$$

The only term contributing to the interference signal is the differential phase shift.

To determine how well the common mode is rejected in the experimental part of this thesis, a factor called common mode rejection factor will be defined.

$$\xi(\Omega) = \frac{measured\ rotation\ rate\ in\ \text{differential}\ mode}{measured\ rotation\ rate\ in\ common\ mode} \tag{2.6}$$

The idea is first to measure the signal when the system is rotating in the differential mode at a specific rate. Then let the system rotate at the same angular velocity, but in common mode, and measure the signal again. The common mode rejection factor will then be obtained by dividing the two results. The higher ξ is, the better does the system reject common mode rotation. Ideally , ξ should be infinity.

The magnitude of the common mode rejection factor is inversely proportional to the difference in effective area, $N \cdot A$, for the two coils. If the difference is large, the factor ξ becomes small, and vice versa.

Assuming it is possible to make the difference in length between the two coils less than 3cm, and the difference in diameter within 0.5mm, this would produce an uncertainty in the rotation rate of

$$\delta\Omega = \frac{\lambda_0 c_0}{2\pi}\left(\frac{1}{L_1 D_1} - \frac{1}{L_2 D_2}\right)\Delta\phi \approx 0.04 \cdot 10^{-3}\Delta\phi \tag{2.7}$$

This result means that the uncertainty in length and diameter in the worst case gives an error of 4% of the rotation rate measured. If the winding machine gives correct number of turns, the length uncertanty should be below the estimation made here, and the diameter uncertanty should be within reach as well (see section 3.1).

By inserting the above expression into the expression for ξ one obtains

$$\xi = \frac{\Omega}{\Delta\Omega} = \frac{\frac{\lambda_0 c_0}{2\pi L_1 D_1}\Delta\phi_R}{\frac{\lambda_0 c_0}{2\pi}\left(\frac{1}{L_1 D_1} - \frac{1}{L_2 D_2}\right)\Delta\phi_R} = \frac{1}{1 - \frac{L_1 D_1}{L_2 D_2}} \tag{2.8}$$

It could be argued that the average length and diameter should be used in the nominator, but one of the coils is somewhat arbitrarily chosen in order to simplify the experimental measurements.

In this discussion, effects contributing to phase shifts have been assumed to be time invariant. This is not exactly true. The counterpropagating light passes through each coil at different times. Therefore, a rotation change within the time of flight between the coils, or time varying external effects changing the phase in a section of the fiber in the system, will be seen as a nonreciprocal phase shift. This will consequently distort the signal.

First, consider external effects working on a local region of the fiber and consequently changing the phase of the waves. For simplicity, assume the system to be fairly symmetric

around the directional coupler. This is not an unnatural assumption, because by placing the sensor coils in each end of the large sized object, and placing the source and detector unit in the middle, a symmetric system is accomplished. The consequence of this assumption is that when a clockwise beam of light propagates in coil A, the counterclockwise beam of light propagates in coil B, and likewise with the fiber connecting the coils to the coupler (fiber 1 and 3 in Figure 2.2). The time constant of interest is consequently the time of flight between the two coils and the time the light uses between the fibers connecting the coils and the coupler. In the time of flight between the two coils, half of the fiber in each coil are accounted for as an example, since there is no point in examining local perturbations in every section of the fiber coil. Equivalent for the fiber connecting the coils to the coupler.

$$\tau_{AB} = \frac{n}{c_0}(L_{coilA}/2 + L_2 + L_{coilB}/2) \tag{2.9}$$

$$\tau_{13} = \frac{n}{c_0}(L_1/2 + L_{coilA} + L_2 + L_{coilB} + L_3) \tag{2.10}$$

where τ_{AB} is the time constant between the two coils, τ_{13} is the time constant between fiber 1 and fiber 3 defined in Figure 2.2, n is the index of refraction, c_0 is the speed of light in vacuum, L_{coilX} is the length of one coil X $(X = A, B)$, and L_i $(i = 1, 2, 3)$ is the length of the connecting fiber i defined in Figure 2.2.

The system has the greatest responsivity to external effects of frequency f [7]

$$f = \frac{1}{2 \cdot \tau} \tag{2.11}$$

where τ is the time constant.

The fiber connecting the two coils (fiber 2 in Figure 2.2), is placed in the middle of the fiber system, and the time constant has to be very small since two counterpropagating beams pass each other in this section. Therefore, effects working on this region must have a very high frequency if it is going to introduce nonreciprocal errors.

To give an order of magnitude to the time constants, assume fiber 1 and 3 (in Figure 2.2) to be 50m, fiber 2 100m, the length of fiber coils 700m, and the index of refraction $n = 1.47$. The total length of fiber is then 1.6km. The time light uses from fiber 1 to fiber 3 is (taken from the middle of the fiber of interest)

$$\tau_{AB} = 3.9 \cdot 10^{-6} s$$

$$\tau_{13} = 7.6 \cdot 10^{-6} s$$

Consequently, the fiber connecting the coils to the directional coupler are most responsive to frequencies f_{13}

$f_{13} \approx 65kHz$

and the two coils are most responsive to external effects with frequencies f_{AB}

$f_{AB} \approx 130kHz$

These are very high frequencies, and most time-varying effects are therefore neglible. External effects can have smaller frequencies for fiber 1 and 3 compared to the coils, but effects usually work on a much shorter section of fiber than in the case of the coils.

In the setup with two 2x2 couplers, a delay coil was used to reduce the modulation frequency, since the ideal modulation frequency depended on the delay coil (Eq. 2.11). However, there is a disadvantage to using such a delay coil. First of all, the delay coil can itself pick up noise (non-reciprocal), but with proper winding and shielding, this noise is expected to be reduced. A greater problem is the fact that more fiber in the system makes it more responsive to acoustic noise as described above. A fiber with optimal modulation frequency of 40 kHz will of course also be very responsive to all time-varying effects with frequency around 40 kHz. In fact, this responsivity can be used to detect acoustic signals instead of rotation rate [8], [9]. Such sensor systems are used as underwater acoustic sensors, and there are experimental systems based on this effect. In these systems an even longer delay line is used (10km - 40km), to reduce the optimum modulation frequency. Compared to the more common hydrofon based on a Mach-Zehnder interferometer, the Sagnac interferometer has the advantage of a stable bias point, a reduced conversion of source phase noise into intensity noise, and a frequency response that matches the ambient ocean noise [10]

The length of the fiber used in gyroscopes is much shorter than those used for acoustic detection, but some of the effects can appear as noise in the system. It is important to notice that the length of fiber used in a differential gyroscope based on a serial configuration will be longer than ordinary gyroscopes, both because it uses two instead of one fiber coil and because of the fiber connecting the different parts of the system. This connecting fiber can be up to several hundred meters.

In the test setup, a delay line of around 1550m was used, making the entire system 2410m long. This made the system responsive to time-varying effects of around 42kHz. In the demonstrator, no delay line was needed since the fiber length now was long enough to make the optimum modulation frequency low enough for the phase locked amplifier. The optimum modulation frequency was here around 65 kHz.

As mentioned previously in this section, a second problem with the long fiber used in the serial configuration is that the rotation rate will change within the time the light uses from one coil to the other. The serial configuration makes the assumption that the light propagates much faster than the rotation of interest, so that the rotation rate can be seen as constant within the time the light uses in the fiber. In principle, if the common mode rotation is high, the rotation rate will have changed within the time the light spends from one coil to the other.

In the case where the system is symmetric, the two counterpropagating waves will observe an equal change in rotation rate between the two coils, and consequently compensate each other. Therefore, in the case of a symmetric system, the common mode rotation could theoretically have an infinite rotation rate and still be rejected. This is a strong argument for using a symmetric setup as assumed above. The effect of change in rotation rate apply for the measurement of the differential rotation as well, but with the rotation rates expected for the application of hull monitoring, the errors introduced will be neglible.

In conclusion, the serial configuration gives correct results in a symmetric system, has a very simple design, and the errors introduced by time varying effects are expected to be small. Therefore, this design has been investigated in the rest of this study.

2.3 Demodulation

The rotation signal in a gyroscope can be retrieved in many ways, depending on how one designs the system.

Two different types of demodulation will be investigated, demodulation when using a 3x3 coupler, and open loop minimum configuration. The latter will from now on be called stable bias, which is a well-known approach for gyroscopes. Both techniques are investigated experimentally as well.

2.3.1 Reciprocal Biasing Modulation-Demodulation

Consider the configuration shown in Figure 2.4.

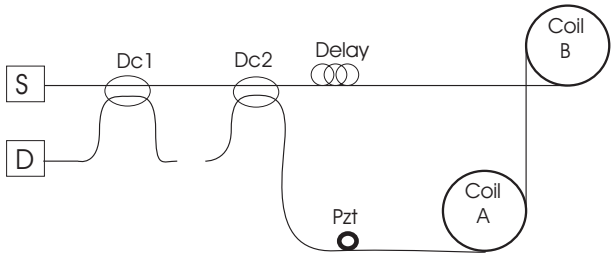

Figure 2.4: Differential gyroscope with two 2x2 couplers

At the output, D, an interference signal is observed. The piezoceramic crystal changes the length of the fiber, and even though the two counterpropagating ligthwaves propagate in the same fiber, they travel past the pzt at different times. In other words, both interfering waves carry the exact same phase modulation, but shifted in time. This timedifference is equal to the group transit time between the long and short paths that connect the modulator and the splitter, which in turn gives a phase difference by

$$\Delta\phi_m(t) = \phi_{cw}(t) - \phi_{ccw}(t - \Delta\tau_g) \tag{2.12}$$

The ideal interference pattern with a configuration as described above will look like:

$$P(\Delta\phi_R) = P_0\left[1 + \cos(\Delta\phi_R + \phi_m(t))\right] \tag{2.13}$$

where P_0 is the input power, $\Delta\phi_R$ is the phaseshift due to rotation, and ϕ_m is the phase shift induced by the pzt.

It is important to notice the time dependence in Eq. 2.12. In contrast to modulation in a Mach-Zender or Michelson interferometer, the Sagnac interferometer is much more dependent on the frequency of the modulation signal, since both the interfering waves propagate through the modulator.

First, consider the use of a square-wave modulation signal

$$\phi_m = \pm(\phi_b/2)$$

where ϕ_b is a phase constant, and the half period is equal to the group transit time. Using Eq. 2.12 when the gyro-coil is at rest, one obtains the signal

$$P(0, -\phi_b) = P(0, \phi_b) = P_0(1 + \cos\phi_b)$$

and under rotation

$$P(\Delta\phi_R, \phi_b) = P_0\left[1 + \cos(\Delta\phi_R + \phi_b)\right]$$

$$P(\Delta\phi_R, -\phi_b) = P_0\left[1 + \cos(\Delta\phi_R - \phi_b)\right]$$

By taking the difference between the two states one obtains

$$\Delta P(\Delta\phi_R, \phi_b) = P_0\left[\cos(\Delta\phi_R - \phi_b) - \cos(\Delta\phi_R + \phi_b)\right] = 2P_0\sin(\phi_b)\sin(\Delta\phi_R)$$

Maximum sensitivity is obtained when $\phi_b = \frac{\pi}{2} \Rightarrow \sin(\phi_b) = 1$.

The interferometer is now being operated in the linear region of the cosine pattern, where the sensitivity to rotation is at its maximum.

One disadvantage with the use of a square wave modulation is the need for a very flat response from the phase modulator. This can be a problem when using a pzt, especially when very high frequencies are involved. Therefore, an alternative approach is to use a sine wave in the modulation (a pzt can follow a sine wave with good accuracy for the frequencies involved here).

$$\Delta\phi_m(t) = \phi_b\cos(2\pi f_m t) \tag{2.14}$$

Inserting this into the interferometer equation 2.12, and using the identity $\cos(x + y) = \cos(x)\cos(y) - \sin(x)\sin(y)$, the output response is found to be

$$P(\Delta\phi_R) = P_0\left[1 + \cos(\Delta\phi_R + \phi_b\cos(2\pi f_m T))\right] \tag{2.15}$$

$$P(\Delta\phi_R) = P_0\left[1 + \cos(\Delta\phi_R)\cos(\phi_b\cos(2\pi f_m t)) - \sin(\Delta\phi_R)\sin(\phi_b\cos(2\pi f_m t))\right] \tag{2.16}$$

This expression can be expanded in Bessel functions

$$P(\Delta\phi_R) = P_0 + P_0\cos(\Delta\phi_R)\left[J_0(\phi_b) + 2J_2(\phi_b)\cos(4\pi f_m t) + ...\right] + \tag{2.17}$$

$$P_0\sin(\Delta\phi_R)\left[2J_1(\phi_b)\sin(2\pi f_m t) + 2J_3(\phi_b)\sin(6\pi f_m t) + ...\right] \tag{2.18}$$

From this equation one can see that the even harmonics are still proportional to $\cos(\Delta\phi_R)$, while the odd harmonics are proportional to $\sin(\Delta\phi_R)$. By synchronous demodulation the fundamental mode becomes

$$P_1(\Delta\phi_R) = 2P_0 J_1(\phi_b)\sin(\Delta\phi_R) \tag{2.19}$$

From the above equation one can observe that the optimal modulation depth no longer is $\frac{\pi}{2}$ but $\phi_b = 1.8$ rad because

$$\frac{dJ_1(x)}{dx} = 0 \rightarrow \phi_b = 1.8$$

$J_1(1.8) = 0.53$, so the price to pay for using a sine wave instead of a square wave is reduced contrast. A graphical representation of the sine wave modulation is shown in Figure 2.5

In Figure 2.5.A the system is at rest. A modulation is applied, and at the output a simple sinusoidal wave of twice the modulation frequency is observed. The phase difference between the interfering lightwaves will vary between ± 1.8. When the system is rotated, as in b), a "first harmonic" of the modulated signal appears at the output. This is the signal one wants to measure and its form is given by Eq. 2.19. A more extensive derivation is given in [11] and [7].

Synchronous detection, the detection of the fundamental mode or the ΔP for the square wave modulation, is done using a lock-in amplifier.

The lock-in amplifier uses a reference signal, in this case the modulation signal, to generate its own sine and cosine wave.

$$V_{gen1} = V_L\sin(f_L t + \theta_{ref}) \tag{2.20}$$

$$V_{gen2} = V_L\cos(f_L t + \theta_{ref}) \tag{2.21}$$

where V_L is the generated amplitude and f_L is the generated frequency (equal to the reference frequency), θ_{ref} is the initial phase of the generated signal.

The generated signal is multiplied with the detected signal (the signal containing the Sagnac phase shift). Two phase sensitive detectors then detect

$$V_{psd1} = V_{sig}V_L\sin(\omega_r t + \theta_{sig})\sin(f_L t + \theta_{ref})$$

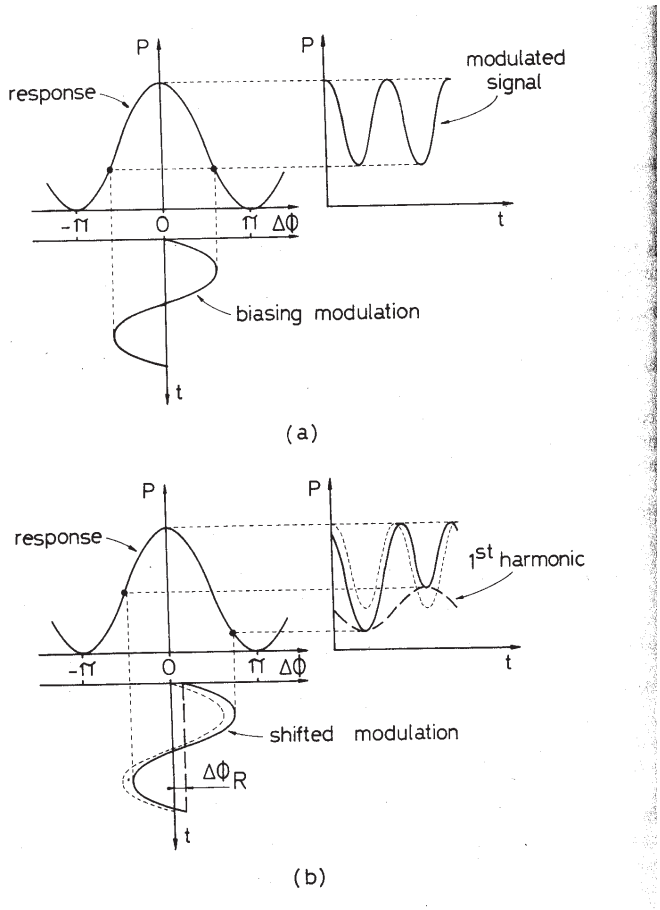

Figure 2.5: Graphical illustration of the stable bias principle [7]

$$V_{psd2} = V_{sig} V_L \cos(\omega_r t + \theta_{sig}) \cos(f_L t + \theta_{ref})$$

By using trigonometric identities, these equations can be written [12]

$$V_{psd1} = \frac{1}{2} V_{sig} V_L \cos((\omega_r - f_L)t + \theta_{sig} - \theta_{ref}) - \frac{1}{2} V_{sig} V_L \cos((\omega_r + f_L)t + \theta_{sig} + \theta_{ref}) \quad (2.22)$$

$$V_{psd2} = \frac{1}{2} V_{sig} V_L \sin((\omega_r - f_L)t + \theta_{sig} - \theta_{ref}) - \frac{1}{2} V_{sig} V_L \sin((\omega_r + f_L)t + \theta_{sig} + \theta_{ref}) \quad (2.23)$$

where $V_{sig} = 2P_0 \sin(\phi_b) \sin(\Delta\phi_R)$ is the Sagnac signal one wants to retrieve, $\omega_r = 2\pi f_m$ is the modulation frequency, and θ_{sig} is the phase of the modulation signal. It is important to keep in mind that this detected signal is in the electrical domain, since direct phase information is hard to detect in the optical domain.

Each phase-sensitive detector now detects two AC-signals, one at the difference frequency ($\omega_r - f_L$) and one at the sum frequency ($\omega_r + f_L$). The output is then lowpass filtered to remove these two terms, and the only thing left is a DC-term. This DC-term arises from the frequency component $\omega_r = f_L$, since the cosine in this case becomes a constant. What is left is then

$$V_{psd1} = \frac{1}{2} V_{sig} V_L \cos((f_L - f_L)t + \theta_{sig} - \theta_{ref}) = \frac{1}{2} V_{sig} V_L \cos(\theta_{sig} - \theta_{ref}) \tag{2.24}$$

$$V_{psd2} = \frac{1}{2} V_{sig} V_L \sin((f_L - f_L)t + \theta_{sig} - \theta_{ref}) = \frac{1}{2} V_{sig} V_L \sin(\theta_{sig} - \theta_{ref}) \tag{2.25}$$

By taking the square root of the square sum of the two outputs one obtains

$$\begin{aligned} V &= \sqrt{V_{psd1}^2 + V_{psd2}^2} = \sqrt{(\frac{1}{2} V_(sig) V_L \cos(\theta_{sig} - \theta ref)^2 + (\frac{1}{2} V_{sig} V_L \sin(\theta_{sig} - \theta_{ref}))^2} \\ &= \frac{1}{2} V_{sig} V_L = V_L P_0 J_1(\phi_b) \sin(\Delta\phi_R) \end{aligned} \tag{2.26}$$

The sign of the signal (V_{sig}) is lost in the last operation, but can be found by observing the phase difference $\theta_{sig} - \theta_{ref}$

$$\theta_{sig} - \theta_{ref} = tan^{-1}(\frac{V_{psd2}}{V_{psd1}}) \tag{2.27}$$

The signal is now proportional to the sine of the rotation rate and can be found by taking the inverse sine or, since the interferometer now operates in its linear region, just neglect the sine alltogether. Another important aspect is the fact that the signal now operates perfectly around zero, which makes the integration from rotation rate to angle of rotation much easier.

2.3.2 Analysis of an I-FOG using a 3x3 fiber coupler

The configuration used in this analysis is shown in Figure 2.6.

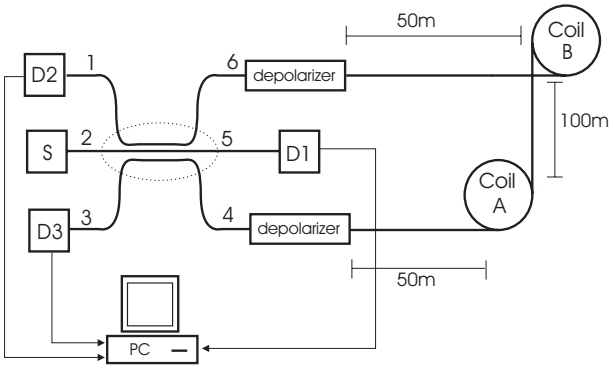

Figure 2.6: Differential gyroscope with a 3x3 coupler

Light is emitted from the source S into the 3x3 coupler. The coupler splits the light into the three output ports 4,5 and 6. The light coming out of port 4 and 6 enters opposite ends of

the fiber coil, and reenters the 3x3 coupler at the other end. The light now coming into port 4 and 6 is once again split in the coupler and comes out at port 1, 2 and 3. There are detectors mounted at port 1, 3 and 5. The first two detectors (D2 and D3) will observe a Sagnac phase shift, while the last (D1) will not.

In the following a quasi-monochromatic approach will be used to set up the Jones matrices for the system.

Assume that the light emitted from the source S is partially polarized in the x direction. This gives the coherence matrix

$$J_S(\lambda) = \begin{bmatrix} \frac{1+P}{2} & 0 \\ 0 & \frac{1-P}{2} \end{bmatrix} I_0(\lambda) \tag{2.28}$$

where P is the degree of polarization and I_0 is the spectral intensity distribution of the lightwave.

The light enters the system described in Figure 2.6. If this system can be characterized by the Jones matrix G, the coherence matrix at the i'th output is given by

$$J_{out,i} = G \cdot J_S \cdot G^{\dagger} \tag{2.29}$$

Here † means the Hermitian conjugate, and $i = 1, 3, 5$.

By tracing each lightwave to its output the Jones matrices of the outputs are found to be

$$G_1 = A_{25} \tag{2.30}$$

$$G_3 = A_{41} S_{cw} A_{26} + A_{61} S_{ccw} A_{24} \tag{2.31}$$

$$G_5 = A_{43} S_{cw} A_{26} + A_{63} S_{ccw} A_{24} \tag{2.32}$$

Here A_{ij} denotes the Jones matrix of the 3x3 coupler from i to j, S_{cw} the clockwise transmission properties of the fiber coil, and S_{ccw} the counterclockwise transmission properties.

Assuming the coupler to be polarization independent, the matrices for the coupler becomes

$$A_{ij} = a_{ij} \begin{bmatrix} 1 & 0 \\ 0 & 1 \end{bmatrix} = r_{ij} e^{j\Phi_{ij}} \begin{bmatrix} 1 & 0 \\ 0 & 1 \end{bmatrix} \tag{2.33}$$

This assumption might not hold in real life, but makes the deduction much simpler.

The properties of the fiber coil can be described by [13]

$$S_{cw} = e^{j\phi_R/2} S_{0cw} \tag{2.34}$$

$$S_{ccw} = e^{-j\phi_R/2} S_{0ccw} \tag{2.35}$$

If one can assume the coil and splices to be lossless, then

$$\Rightarrow S_{0cw} = \begin{bmatrix} -\sqrt{1-\alpha e^{-j\xi}} - \sqrt{\alpha} & e^{-j\eta} \\ -\sqrt{\alpha} & e^{j\eta} + \sqrt{1-\alpha e^{j\xi}} \end{bmatrix} \tag{2.36}$$

Here α is the effective coupling strength between the x- and y-polarizations, and ξ and η are effective phase shifts induced by birefringence and coupling effects in the coil.

It is not possible to get a lossless system in the experiments, but with well aligned splices and a fiber coil with a not too small diameter, the approximation is reasonable. By using equation 3.30 through 3.36 in equation 3.29 one obtains the Jones matrices at the detector outputs. The intensity at these ends are given by the trace of the Jones matrices

$$I_i(\lambda) = Tr\{J_{out,i}(\lambda)\} = Tr\{G_i(\lambda) \cdot J_s(\lambda) \cdot G_i^+(\lambda)\} \tag{2.37}$$

The optical power is the integral of the intensity

$$\mathcal{P} = \int I dA$$

The current in the detector is given by the responsivity $i_p = \Re \cdot \mathcal{P}$, and with a load resistance R_f the voltage observed at the output is

$$V_1 = v_1 D_1 I_0 \tag{2.38}$$

$$V_2 = v_2 \left[A_2 + kB_2 \cos(\phi_R - C_2 + \Phi_F)\right] D_s I_0 \tag{2.39}$$

$$V_3 = v_3 \left[A_3 + kB_3 \cos(\phi_R - C_3 + \Phi_F)\right] D_s I_0 \tag{2.40}$$

where $v_i = R_f \Re A$ are the convertion constant between light intensity and observed voltage.

The factor A_i is a constant given by the splitting ratios of the 3x3 coupler:

$$\begin{aligned} A_2 &= r_{26}^2 r_{41}^2 + r_{24}^2 r_{61}^2 \\ A_3 &= r_{26}^2 r_{43}^2 + r_{24}^2 r_{63}^2 \end{aligned} \tag{2.41}$$

The factor B_i determines the amplitude of the output signal and is given by

$$\begin{aligned} B_2 &= 2 r_{26} r_{41} r_{24} r_{61} \\ B_3 &= 2 r_{26} r_{43} r_{24} r_{63} \end{aligned} \tag{2.42}$$

C_i is the phase angle introduced by the 3x3-coupler.

$$\begin{aligned} C_2 &= \Phi_{26} + \Phi_{41} - \Phi_{24} - \Phi_{61} \\ C_3 &= \Phi_{26} + \Phi_{43} - \Phi_{24} - \Phi_{63} \end{aligned} \tag{2.43}$$

The factor D is the splitting ratio of the 3x3 coupler from port 2 to 5

$$D = r_{25}^2 \tag{2.44}$$

The factor d_s is the attenuation factor of the fiber coil and splices, I_0 is the intensity of the light source, Φ_F the phase angle introduced by the coupling effects

$$\Phi_F = arctan(P\frac{\alpha\sin(2\eta)}{1-\alpha+\alpha\cos(2\eta)}) \tag{2.45}$$

The contrast factor, k of the interference signal is given by

$$k = \sqrt{(1-\alpha+\alpha\cos(2\eta))^2 + P^2(\alpha\sin(2\eta))^2}, \tag{2.46}$$

and Φ_R is the Sagnac phase shift (see appendix A)

An ideal symmetrical coupler has $r_{ij} = \sqrt{1/3}$ for all i and j, and phase shifts $\Phi_{ij} = -\frac{2\pi}{3}$ or $\Phi_{ij} = 0$. This makes

$$A_2 = A_3 = \frac{2}{3}$$

$$B_2 = B_3 = \frac{2}{9}$$

$$C_2 = \frac{2\pi}{3}$$

$$C_3 = -\frac{2\pi}{3}$$

$$D = \frac{1}{3}$$

If in addition the fiber splices and coils are lossless and without coupling effects, then $k = 1$ and $\Phi_F = 0$, and the outputs become

$$V_1 = \frac{v_1 I_0}{3}$$

$$V_2 = \frac{2v_2 I_0}{9}\left(3 + \cos(\phi_R - \frac{2\pi}{3})\right)$$

$$V_3 = \frac{2v_3 I_0}{9}\left(3 + \cos(\phi_R + \frac{2\pi}{3})\right)$$

One can from this observe that both detector D2 and D3 will correctly detect the sagnac phase shift around a point on the interference curve where the response is relatively linear.

In a non-ideal system the output signal is a bit more complex. Firstly $A_2 \neq A_3$, $B_2 \neq B_3$ and $C_2 \neq C_3$, wich means that the 3x3 coupler is nonsymmetric. This removes the signal from the quadrature point on the interference curve. Still, the quality of the commercial couplers available today are usually quite good, so this aspect is not as important as it used to be.

A larger problem is the nonideal contrast factor k, and phase angle Φ_F introduced by coupling effects in the fiber coils. These factors may vary over time and with different rotation rates. From Eq. 2.45 we observe that Φ_F depends on the degree of polarization. By using unpolarized light this factor vanishes. To overcome the variations due to the contrast factor a signal recovery scheme has been proposed [14]. This scheme uses a single equation which relates the rotation rate to the output voltages

$$\frac{(V_2 - V_3) + f_1 V_1}{(V_2 + V_3) - f_2 V_1} = f_3 \frac{\sin(f_6\Omega + f_4)}{\cos(f_6\Omega + f_5)} \tag{2.47}$$

where Ω is the rotation rate and

$$f_1 = \frac{v_3 A_3 - v_2 A_2}{v_1 D_1} d_s$$

$$f_2 = \frac{v_3 A_3 + v_2 A_2}{v_1 D_1} d_s$$

$$f_3 = \frac{\sqrt{\left[v_2 B_2 \cos(C_2) - v_3 B_3 \cos(C_3)\right]^2 + \left[v_2 B_2 \sin(C_2) + v_3 B_3 \sin(C_3)\right]^2}}{\sqrt{\left[v_2 B_2 \cos(C_2) + v_3 B_3 \cos(C_3)\right]^2 + \left[v_2 B_2 \sin(C_2) - v_3 B_3 \sin(C_3)\right]^2}}$$

$$f_4 = arctan\left[\frac{v_2 B_2 \cos(C_2) - v_3 B_3 \cos(C_3)}{v_2 B_2 \sin(C_2) + v_3 B_3 \sin(C_3)}\right]$$

$$f_5 = arctan\left[\frac{v_2 B_2 \sin(C_2) - v_3 B_3 \sin(C_3)}{v_2 B_2 \cos(C_2) - v_3 B_3 \cos(C_3)}\right]$$

The constants f_1, f_4 and f_5 are all close to 0 (equal to 0 for an ideal coupler)

The six coefficients (f_1 to f_6)is determined by a calibration procedure. This involves registration of the output voltages at well known rotation rates in the range of rotation in which the gyro is supposed to operate. The coefficients can then be found by using a nonlinear equation solver, and are described in section 3.2. For a better performance, a temperature factor (and other interesting effects) may also be included in the coefficients.

2.4 Differential gyroscope in a ship hull for torsion measurement

In the introduction to this thesis some differences between an ordinary gyroscope and a differential one was outlined. The concept of measuring torsion angle in large sized objects such as boats was also introduced. In the following, some aspects of this application is further examined, and some requirement for the system are proposed.

In large sized object such as boats, the hull can not be seen as a totally rigid body. The boat will bend and twist in different ways. The task for this thesis is to develop a system that can measure the torsion angle directly in such objects.

Picture two coordinate systems positioned at each end of the boat, with centers on the axis of rotation. The two systems will rotate compared to eachother when the object is exposed to rotational momentum as shown in Figure 2.7. This motion can be decomposed into a DC term, a long term drift caused by deformation of the object, and an AC term. If one assumes that the AC term has sinusoidal behavior, the angle of rotation between the two coordinate systems can be described as

$$\alpha(t) = DC(t) + \alpha_0 \sin(\omega t) \tag{2.48}$$

where α_0 is the amplitude of the AC term and ω is the angular frequency.

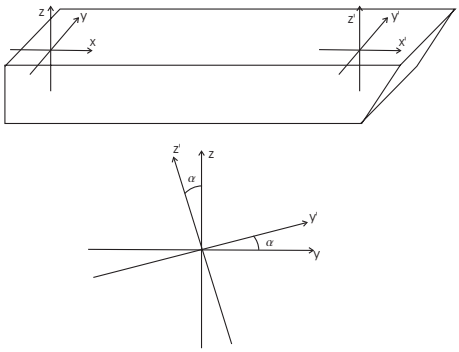

Figure 2.7: Boat with coordinate system

The DC component is assumed to be very slowly varying (otherwise the boat will break), and therefore difficult to detect. This thesis does not aim to detect such a variation, but focuses on the AC term (assumes DC term to be neglible).

The AC component is assumed to have an amplitude above 1 mrad, and a frequency from a few tenths of a Hertz to around 10 Hz. This leads to the main requirement for the system to develop; the system must be able to detect a signal

$$\alpha(t) = \alpha_0 \cdot \sin(\omega t) \tag{2.49}$$

where

$\alpha_0 > 1$mrad

$f \approx 3 - 60$rad/s$(= 0.5 - 10Hz)$

The system developed here measures the torsion at two points, so the placement of the sensors is not trivial. One idea can be to place the sensors around critical points, places where the construction is weak or the torsion is critical.

Requirement for the system is given by the need to convenient installation on the ship. If the system is going to be used, it must be easy to mount and to remove. In other words, the system is not supposed to be built into the boat, and be left on board for the lifespan of the hull. This sets some requirements on what type of connectors to use, because it must be possible to separate the two coils and the source/detection part.

The last requirement is that the system should preferrably be a low cost system. From this follows that expensive components like polarization maintaining fibers and integrated optics circuits should be avoided.

2.4.1 Simplifications and drawbacks

Ordinary gyroscopes usually have to work over a large dynamic range and must handle steady rotation rates. For the application of measuring torsion in large sized objects with the use of a differential gyroscope, one can make some simplifying assumptions about the range and frequency in which the system should operate. This can again simplify the signalprocessing and design.

First of all, one can assume that the angle of rotation is small, othervise the object would be seriously damaged. This can limit the operating range as compared to an ordinary gyro. This can for example simplify the model by not requiring a closed loop operation, where a feedback loop in the modulation is used. In the former subsection it was assumed that the torsion angle was in the area of 1mrad with a frequency up to 10Hz. This information can substantially narrow the dynamic range.

Another advantage here compared to an ordinary fiber optic gyroscope for navigation purposes is the reduced requirements to the scale factor. In navigation grade gyroscopes errors in the scale factor will add to the total error with time. Strong requirements are consequently composed on the scale factor. In the application involved in this project, the DC term is of no interest, so errors introduced by the scale factor will not increase with respect to time. It is also not critical if the measured rotation rate is 1% too small or too high.

The most intuitive problem a differential setup gives, compared to an ordinary gyro, is the induced noise caused by different external forces working on the coils and the noise induced in the fiber connecting the two coils and the coils to the source/detector. A typical length between the two coils can be 100m and if the source and detector part is in the middle, one has to expect around 50m of fiber between the source part and each coil. This fiber can of course pick up problems from external effects, and some preliminary tests have been done (see section 3.2 and 4.2). The connecting fiber will also experience torsion itself. This should ideally influence only the polarization, unless the fiber is bent enough to cause loss somewhere in the connecting fiber. This problem is examined further in section 3.3.

The setup with the source/detector part in the middle, and the sensor coils at each end (of the boat) has been assumed in the experimental work. This gives a symmetric setup, which gives some advantages. One advantage lies in understanding the noise effects, since the interfering light will propagate symmetrically around the middle of the Sagnac loop (which is placed close to the source/detector part). One thing that can cause a problem here, is that the connecting fiber will set up a Sagnac interferometer on its own. Even though the fiber connecting the two coils will lie close to the fiber connecting the coils to the directional coupler, the system will enclose an area. From appendix A.1, the Sagnac effect was shown to be proportional to the area of the fiber system. Figure 2.8 shows this problem. To make an estimate, consider the fiber connecting the two coils to be 100m, the fiber connecting the coils to the coupler 50m each, and the distance between the fibers 3mm (diameter of a standard coating). This produces a rectangle with area $A_b = L \cdot b = 100 \cdot 3 \cdot 10^{-3} = 0.3m^2$. Here, L is the length of the rectangle and b is the height. The effective area of the coils used in the demonstrator is $A_{eff} = 68m^2$. The difference between the two areas is large, but since the rotation rate is usually larger for the Sagnac interferometer made up by the connecting fibers, this interferometer can cause problems. An easy method for reducing this problem is twisting the connecting fibers.

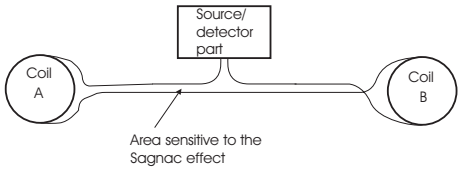

Figure 2.8: Differencial gyroscope setup in boat, showing how the fiber connecting the parts can form an area sensitive to the Sagnac effect

2.4.2 Errors due to oscillations at several internal vibration modes

From section 2.1 it was proposed a serial configuration as an optimal configuration for the application of interest. In the discussion below, a serial configuration is consequently assumed. It would now be interesting to take a closer look at what is actually measured, and whether small misalignments will introduce unrecoverable errors. To simplify the deduction, it is assumed that the boat behaves as an elastic beam. This implies that the object can bend and rotate in four different ways, illustrated in Figure 2.9

The beam can bend in the vertical direction (in the xz-plane), the horizontal direction (xy-plane), in the transversal direction(yz-plane), and one can observe torsion.

First, view the boat from the side, the xz-plane. The boat can here be bent in the z-direction (symmetrical around amidships). The coils constructing the differential gyroscope are situated in the yz-plane, and therefore always normal to the bending. Consequently this type of bending will not influence the rotation signal, even if the coils are misalingned in the z direction.

When the boat is viewed from above, in the xy-plane, the same arguments apply. The two coils will be normal to the rotation, and therefore not give any Sagnac phase shift.

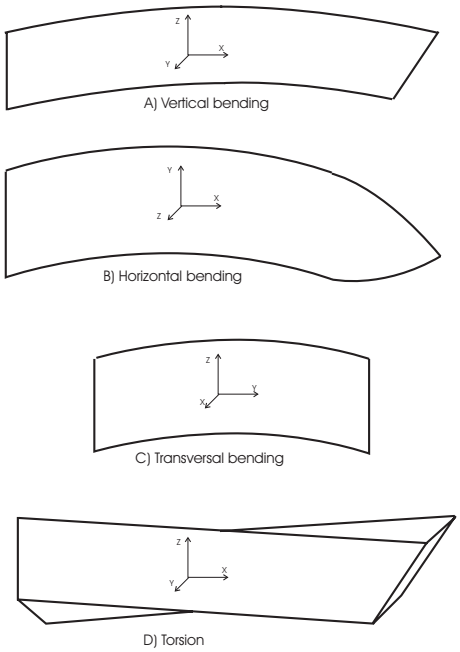

Figure 2.9: Bending modes in boat

Next, view the boat from the front, in the yz-plane. If only torsion was introduced, the gyroscope would observe the same rotation no matter where in the plane the coils where positioned. This is because a radial displacement away from the axis of rotation will not influence the rotation itself. If one includes the transversal bending as well, which means bending in the z-direction symmetric around the z axis, the differential gyroscope can also become sensitive to this effect. If a sinusoidal model is used, the angle of bending, β, is given by.

$$\beta = \arctan(\cos(y))$$

Here, y is the distance from the boat's longitudinal axis.

If the two fibercoils constituting the differential gyroscope is situated on the z axis , they will not experience any rotation due to this transversal bending. Also if the two coils are situated opposite each other, i.e. have the same y-position, they will experience the same rotation and will therefore cancel the contribution from transverse bending. On the other hand, if they are misaligned in the y- direction they will experience different rotation, and therefore be sensitive to bending.

The Sagnac phase difference becomes

$$\Delta\phi = \Delta\phi_{torsion} + \Delta\phi_{bending} = \frac{2\pi L \cdot D}{\lambda_0 c_0}(\Omega_t + \Omega_{tb}) = \frac{2\pi LD}{\lambda_0 c_0}(\alpha_0\omega_t \cos(\omega_t t) + f(\beta)) \quad (2.50)$$

where $\Delta\phi_{torsion}$ is the Sagnac phase difference due to torsion, $\Delta\phi_{bending}$ is the Sagnac phase difference due to bending, $\Omega_t = \alpha_0\omega_t \cos(\omega_t t)$ is the rotation rate due to torsion, and

$\Omega_{tb} = f(\beta)$ the rotation rate due to transversal bending and a function of the angle of bending. In conclusion, to avoid errors due to transversal bending, the gyroscope coils must be situated close to the axis of bending (z-axis).

Until now, it has been assumed that the two coils are perfectly aligned in the yz-plane. This assumption will now be examined in more detail. View the boat again from the side (xz-plane), as in Figure 2.9. If now one coil is misaligned with an angle γ_z to the z axis, the effective area for detection of the torsion will become smaller. The Sagnac phase shift is proportional to the area of the coil $\Phi_s = \frac{8\pi A \cdot N}{\lambda_0 c_0}\Omega$ (appendix A.1) and the two coils will therefore experience different phase shifts under rotation. This misalignment gives three types of errors. First, the misaligned coil will not experience the differential rotation as it should, and consequently give a smaller rotation signal than the boat actually goes trough. Second, the common rotation will not be fully compensated, so a phase shift proportional to the overall rotation of the boat will be introduced. And third, the misaligned coil will also become sensitive in a the xy plane, since the gyroscope now have a component in the z-direction. This component will be proportional to the horizontal rotation of the boat

$$\Phi_{xz} = \Phi_A - \Phi_B = \Phi_c + 1/2\Phi_t - \Phi_c \cdot \cos(\gamma_z) + 1/2\Phi_t \cdot \cos(\gamma_z) + \Phi_{vertical} \cdot \sin(\gamma_z) \quad (2.51)$$

$$= \Phi_c(1 - \cos(\gamma_z)) + \frac{\Phi_t}{2}(1 + \cos(\gamma_z)) + \Phi_{vertical} \cdot \sin(\gamma_z) \quad (2.52)$$

If the two coils are equally misaligned by an angle γ , common mode will be rejected again, but the components now sensing in the horizontal plane will now add eachothers phase-shifts, rather than canceled, and this will introduce errors. Also the sensitivity to torsion will be reduced by $\cos(\gamma)$. If the misalignment is caused by vertical bending, the sensitivity to torsion will not be reduced, since the coils still are placed normal to the axis of (torsonial) rotation, but one will still have the errors induced by horizontal rotation. In this way, vertical bending gives an indirect error, by making the coils sensitive to rotation around a different axis.

When the boat is viewed from the top (xy-plane), the same arguments can be used by replacing the misalignment angle γ_z with γ_y and horizontal rotation with vertical rotation. The phase shift then becomes

$$\Phi_{xy} = \Phi_c(1 - \cos(\gamma_y)) + \frac{\Phi_t}{2}(1 + \cos(\gamma_y)) + \Phi_{horizontal} \cdot \sin(\gamma_y)) \quad (2.53)$$

2.4.3 Estimate of errors

From the above discussion and from assumed magnitudes of the bending (i.e. that vertical misalignments are larger than horizontal misalignment), one recognizes the vertical bending of the boat and angular misalignment as the most critical factors. Both factors are proportional to both the angle between the normal of the coil and the axis of rotation of the boat, and to the speed of the rotation(navigation) of the boat. Estimates of the magnitude of these effects will now be given.

First, consider the vertical bending of the ship. If the area where the sensor is placed is bent an angle β_1 compared to the horizontal axis, the sensors will pick up a rotation due to manouevering of the ship. This would introduce an error in the rotation rate of

$$\Delta\Omega = 2 \cdot \sin(\beta_1) \cdot \Omega_{horizontal}$$

where $\Omega_{horizontal}$ is the rotation of the ship due to manoeuvering. The factor 2 is caused by the fact that both sensors will detect manoevring of the boat. To get a numerical estimate, assume $\beta_1 = 1^o = 0.0175rad$ and $\Omega_{horizontal,max} = 90^o/20s = 0.079$ rad/s. This gives

$$\Delta\Omega = 2.75 \cdot 10^{-3} rad/s$$

This is on the same order of magnitude as the rotation rate expected for the torsion angle, and might consequently introduce too much noise for the torsion angle to be detected.

Likewise, if the two sensors are misaligned by an angle β_2, the sensors will pick up rotation due to manouevering given by

$$\Delta\Omega = \sin(\beta_2) \cdot \Omega_{horizontal}$$

Also, in this case of misalignment of the two sensors, the rotation due to torsion will be reduced by $1 - \cos(\beta_2)$.

From the above estimates, it has become apparent that the bending of the boat will limit the performance. Methods for reducing the longitudinal bending working on the gyroscopes, would consequently be of interest.

3 EXPERIMENTAL

3.1 Characterization of components

3.1.1 Source

An erbium source (fiber amplifier using spontaneous emission as a power source) was used in this project. This source is a broadband source with peak at 1530 nm and a 1560-1570nm shoulder (Figure 3.1). This gives a very short coherence length, which improves the signal to noise ratio, since backscattering/backreflection does not contribute to the interference signal. The source used in these experiments did not give a significant 1530nm peak at low power, but the peak was observed when the source gave an output above 4mW.

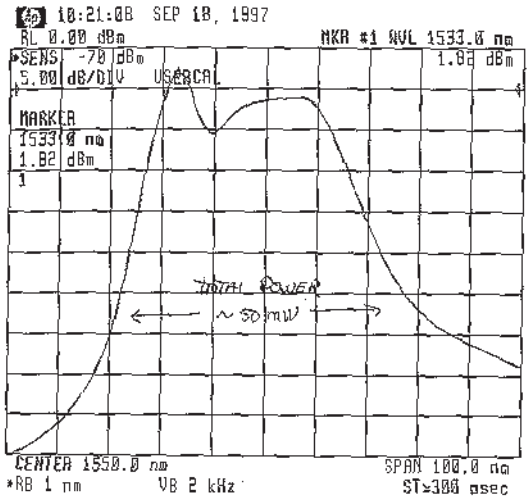

Figure 3.1: Data sheet from the Erbium source showing the frequency spectrum

The total power used in the experiments was around 2mW, which gave a very symmetric wavelength spectrum (Figure 3.2). According to appendix A.3 this should reduce errors compared to a higher output power due to unsymmetrical spectrum. From Figure 3.2 one can also observe that the source have a bandwidth of around 40nm, which proves that the Erbiumsource is a broadband source. The Erbium source amplifies spontaneous emmission which is unpolarized. This makes the output light depolarized.

3.1.2 Fiber

The optical fiber used in these experiments is an ordinary telecommunication fiber. The fiber had an attenuation (factor) of 0.20 dB/km at 1550 nm. With a total system of less than 2km the attenuation due to imperfect fiber was neglible compared to loss in different components.

It was necessary to measure the index of refraction in order to measure the length of the

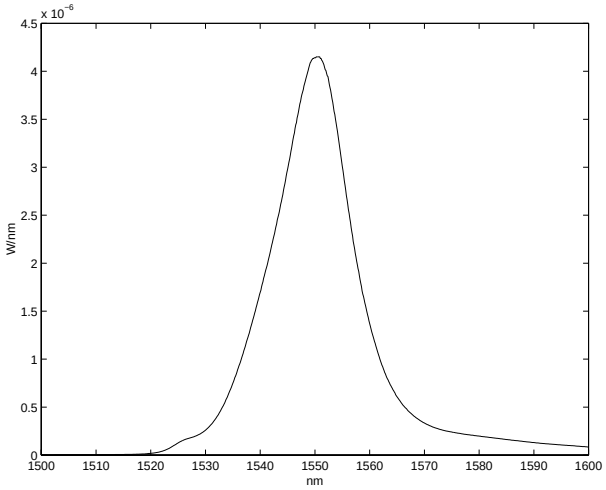

Figure 3.2: Measured frequency spectrum for a representative power(around 2mW)

fiber in each coil. The index was measured in the following way. A pig-tailed connector was spliced to a part of the fiber (around 5m). Laser pulses was sent from a source through the fiber and detected at the other end. A signal-analyzer (Tektronix CSA803 Communication signal analyzer) measured the time the light used from the source to the detector. The fiber for measurement was then cut off, and the same measurement was done with only the connector part. The time difference between the two measurements, $\Delta t = 23.02ns$, gave the time the light used in the fiberpart that was cut of. The length of this fiber, L, was measured. The measurement of the length was assumed to be the limiting factor, and the accuracy was estimated to be $\pm 3mm$

$$L = 4.682m \pm 3mm$$

The index of refraction n was now given by

$$n = \frac{c_0 \cdot \Delta t}{L} = 1.470 \pm 0.001$$

3.1.3 Couplers

The ideal split ratio for the two 2x2 couplers are 50/50 (3dB), since the light passes through the coupler in both directions.

The split ratios were measured. The first coupler had a split ratio of 46.6/53.4 ($\pm 0.2\%$) with a 3.37 $\%$ loss, and the second coupler had a split ratio of 46.8/53.2 ($\pm 0.2\%$) with a 2.74 $\%$ loss. The total loss from source to detector due to the couplers then become

$$Loss = 89\% \pm 1\%$$

Only $11\%(9.63dB)$ of the input power reaches the detector because of the couplers.

Since this system is strictly reciprocal, no phase shifts are introduced by the couplers seen from the detector.

An important parameter in the fiber components has been the polarisation dependent loss(PDL), which indicates the degree of polarisation of the output light. Under the tests, it was noticed that the power at the output could be altered by using the polarization controller which was placed between the second coupler and the coils. This indicates that the interfering light was partially polarized. And, since the source sends out unpolarized light, some of the components must filter the light in such a way that some states of polarization are reduced or lost. Consequently, the PDL measurements indicate which components that "filter" the light.

The test was carried out as follows. Light from a source was sent to a monochromator input of a spectrum analyzer (HP 70951B Optical Spectrum Analyzer), which selected only a narrow frequency spectrum. A polarizer was put at the monochromator output, and the light went to a polarization controller from here. After the polarization controller, the light propagated through the component one wanted to measure, and then to a detector. The light that propagate through the component of interest are consequently monochromatic (approximately) and polarized. The spectrum analyzer scans over the wavelength range of interest using a tunable filter (monochromator), and the polarization controller scans over every polarization state. This means that when light of a specific frequency propagates through the components under test, it has a "random" state of polarization (SOP). Multiple scans must therefore be used, to include most of the SOP's. The signal analyzer uses its first scan as a reference, and look at the deviation (max and min) from this reference in the next scans. If every polarization state has the same loss, no PDL is measured. One problem was that this method included polarization-dependent loss in the polarization controller. However, the test give an qualitative knowledge even though the accuracy is poor.

The two 2x2 couplers gave a PDL measurement as in Figure 3.3.

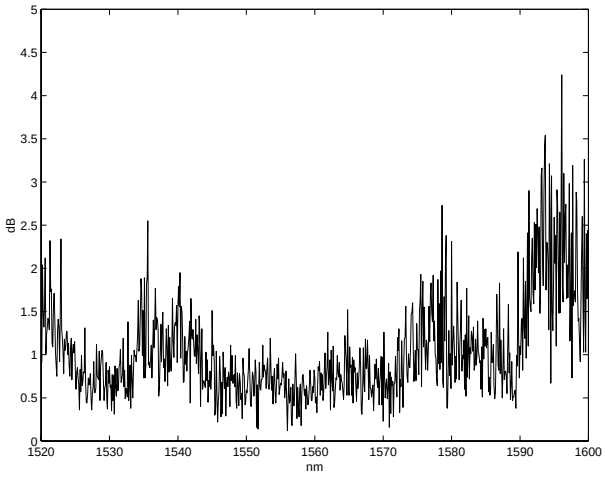

Figure 3.3: PDL measurement of two 2x2 couplers

The couplers do have some polarization dependent loss. The increase in PDL near 1600nm may be because the polarization effects in the coupler increase with the wavelength, but this

is outside the spectral range of the source (from 1530nm to 1570nm). Consequences of the PDL is discussed in section3.3.

The 3x3 coupler had some polarization dependent loss as well, shown in Figure 3.4

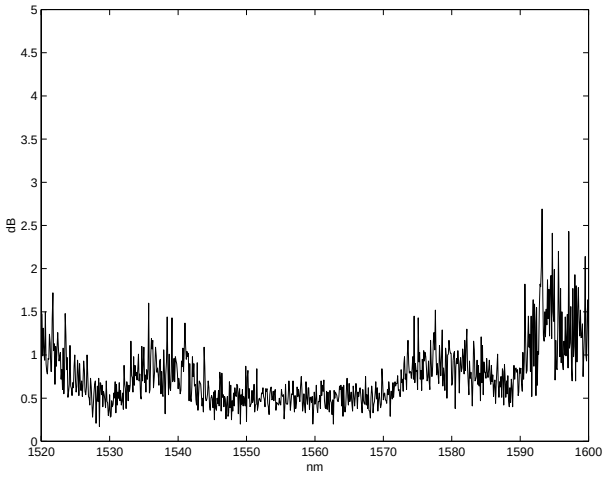

Figure 3.4: PDL measurement for a 3x3 coupler

The scattering matrix for the 3x3 coupler (see appendix A.4) was measured in the following way. Light was sent in turn into fiber 1,2,3 in Figure A.5, and the output light from fiber 4,5,6 was measured each time. The input and output fiber were reversed to check the reciprocity. If deviations where found (light sent from fiber 1 to 4 vs. light sent from 4 to 1), the average was used. The square of each element of the scattering matrix was now found, the matrix was normalized and each element was easily calculated by a square root operation. The matrix becomes

$$M = \begin{bmatrix} 0.556 & 0.525 & 0.589 \\ 0.575 & 0.575 & 0.513 \\ 0.519 & 0.596 & 0.556 \end{bmatrix}$$

The square of element a_{ij} gives the transmittance from port j to port i. The light can therefore be traced around the interferometer, and the losses due to the coupler can be found. At output port 1 (in Figure A.5): 19.6% of the light is detected, and at output port 3: 17.3% of the light reaches the detector. Compared to the two 2x2 couplers, the configuration with the 3x3 coupler requires less light. The coefficients given above are the real parts, phase shifts were not measured. One method for determinig the phase shifts are given in [15], but this experiment was not performed here.

3.1.4 Fiber Coils

This section describes the manufacturing of the sensor coils. The section is very detailed, since a lot of time and effort were used here, but also because the construction the coils played a critical part in the performance of the system.

In the early experiments, the spool diameter was 0.16 m. The spools were made of PVC, and had a very thin mantel. Around each spool, 410m of fiber was wound. Problems in the winding process resulted in significant tension in the fiber, which again induced birefringence. This birefringence, together with expansion/contraction in the PVC coil due to external effects (temperature,vibrations etc.) might have been one of the reasons for the problems with drift in polarization, and sensitivity to external effects.

Figure 3.5: Aluminium spool with epoxy (stycast) glue

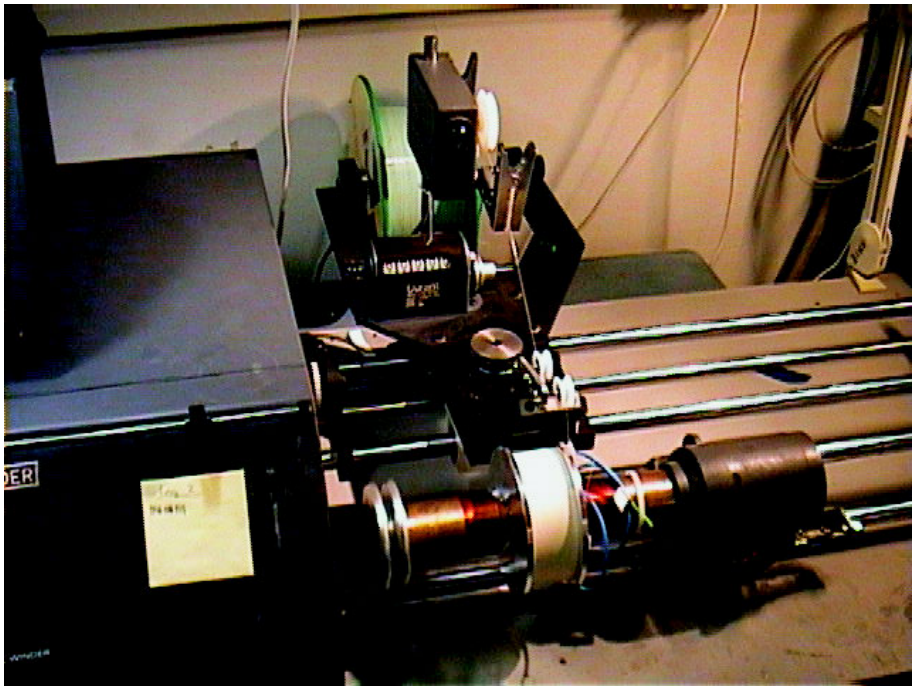

Figure 3.6: Aluminium spool in winding machine

For the demonstrator, a spool of aluminium was made. The spool was solid, exept from a 20mm hole in the midle. A massive spool was chosen to reduce temprature gradients, and to lower the resonant frequencies in the aluminium spool. The drawing is shown in appendix C. Before the fiber was wound around the spool, the spool was first sanded, and then washed with trichloretylene(to get rid of grease) and aceton. The spool should now be absolutely clean, and with enough friction to prevent the fibers from sliding away from each other. To protect the fiber from damaging and to reduce external nonreciprocal effects (acoustic signals), the fibers where covered in epoxy. A hard epoxy was chosen, Stycast 1264, to prevent the fiber from extracting and contracting due to temperature variations. A thin layer of Stycast was put between the first fiber layer and the aluminium spool, a thin layer was also put between each layer of fiber, and over the outer fiber layer. The epoxy needed 48 hours to cure. During the first 20 hours the coil had to be rotated at a slow rotation rate, for the epoxy to be symmetrically distributed. The fiber was wound in a winding machine, with 16 layers, each containing 140 turns.

The transmission losses of 94% $(-13dB)$ of the emitted light came out at the other end of the fiber coil.

An Optical Time Domain Reflectometer (OTDR), was used to examine the loss distribution in the fiber coil(Anritsu MW9076B). The OTDR emits light into the fiber under test, and measures the reflections coming back to the OTDR, and thus estimates the loss in the fiber.

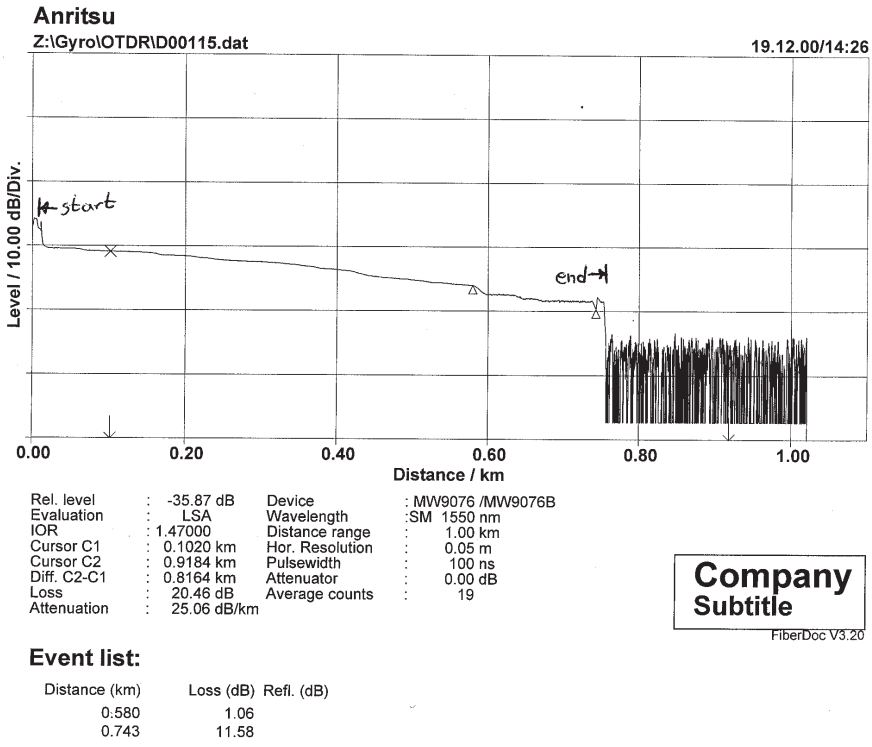

Figure 3.7: Optical loss distributed in a fiber coil

From Figure 3.7 it can be seen that there are high losses at the start and end of the fiber coil, but also losses continously distributed over the fiber rounds (exept from the first layer). The input and output fiber of the coil was mounted 45^o compared to the direction of the fiber rounds which induced a sharp bend at the input and output. In later versions of the coil, this

bend was minimized by making an almost parallell cut into the outside of the aluminium coil with a small hole at the end (Figure 3.8). This reduced these losses to neglible amounts.

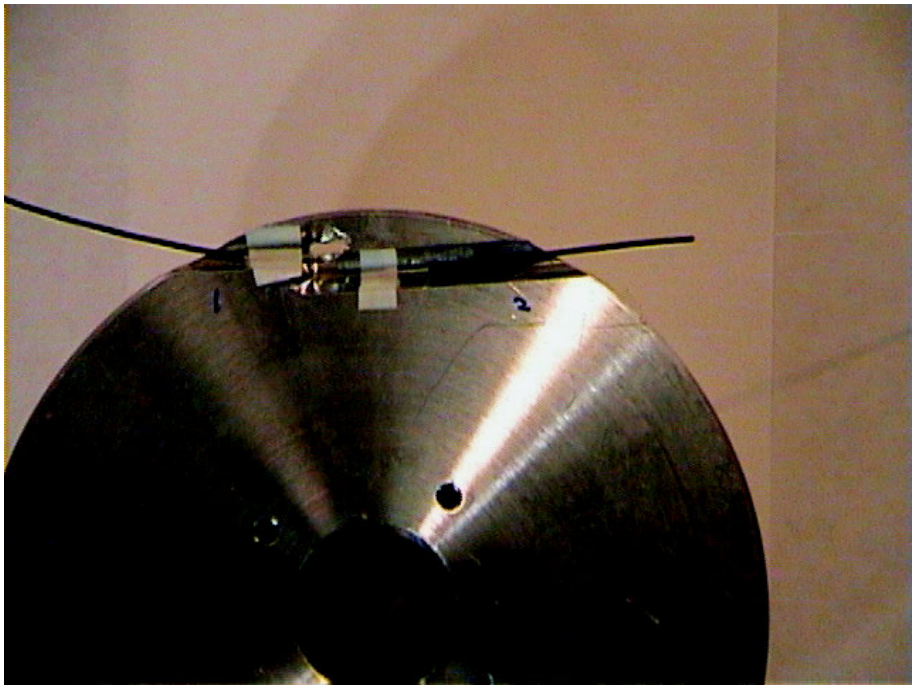

Figure 3.8: Aluminium spool showing input and output fiber

The diameter of the coil was supposed to be large enough to avoid bending induced loss [16]. At 1550 nm, light propagating in ordinary telecom fiber induces losses due to bending when the diameter is 5cm or less. The coil used here had a diameter of 10cm. The reason for the high losses therefore seem to arise from microbends caused by crossing fibers. Each layer did not lie perfectly on top of the previous layer. Fibers where therefore crossed and the above layers pressed the fibers together to induce microbends. The fact that the first layer did not seem to have any loss strengthen this hypothesis.

Consequently, a new coil had to be made. This time no epoxy was used, and each round was as close to the previous round as possible. This made each layer much smoother, to try to reduce the number of microbends. But, it was not possible to avoid microbends at the start and end of each layer. As more layers were put on top of each other, it was more difficult to get the rounds close together, and each layer seemed more elastic. During production of the coil, loss measurements were made for each layer added to the coil. The number of layers in this coil was reduced from 16 to 14 since the the last layers gave high losses (these induced losses to all the underlying layers), but the number of rounds per layer was increased to 150.

The OTDR loss test measurements of the new coils are shown in Figure 3.10. The input and output losses are now reduced, but there are still losses due to microbends. There is also large losses after about 345m. This length of the fiber is close to an end of a layer, where avoiding microbends was more difficult. The loss was measured to be:
$Loss = 4.47dB = 64.3\%$.

The length of the fiber was measured both by counting the turns while winding, and by using a pulsed laser. The counting machine seemed to give an exact number of turns, so this

Figure 3.9: Aluminium spool

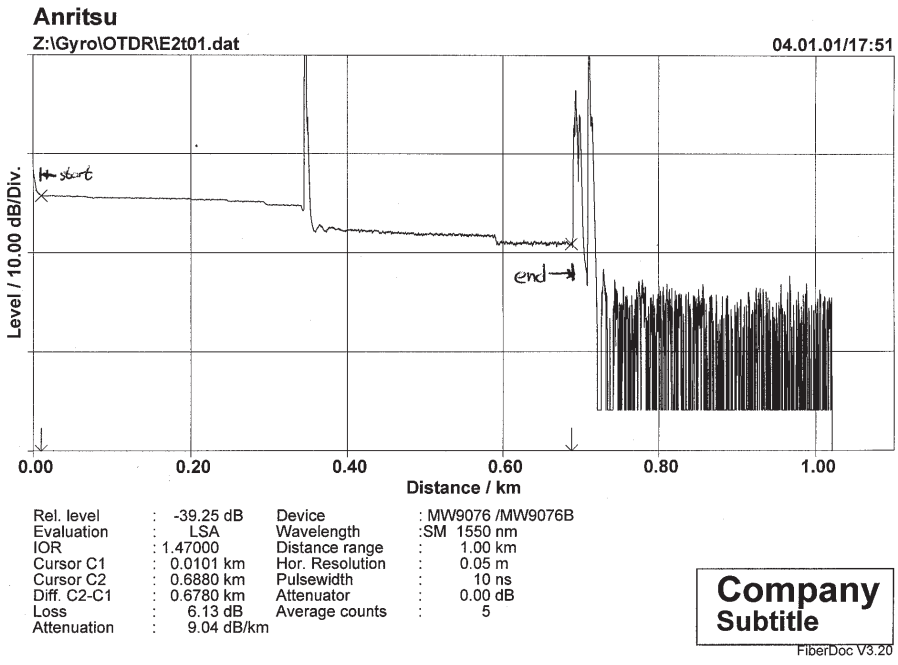

Figure 3.10: Loss test of fiber coil used in demonstrator

would give an uncertanty in length of less than 10mm, if the coil diameter was known. To determine the diameter, the length was measured as descibed under the measurement of the index of refraction, exept that now the length was the unknown.

$$L_{coil1} = \frac{c_0 \cdot \Delta t}{n} = 677.30m \pm 0.05m$$

If the number of turns are correct, this would give the average diameter D

$$D = \frac{L_{coil}}{\pi \cdot N} = 0.1030m \pm 0.5mm$$

Here, N is the number of turns. Consequently the height of each layer (average) would be $D_{layer} = 0.1026/14 = 0.19mm$. If each layer was perfectly placed, the average height would be $0.22mm$. The measured height is therefore reasonable.

An equal coil was made as the second sensor. The length and diameter for this coil was measured as descibed above, and found equal to the first coil.

Polarization dependent loss was measured here as well, and Figure 3.11 shows the result from the second coil

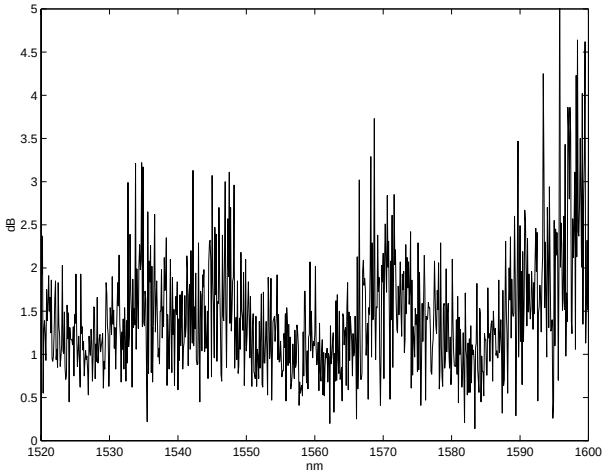

Figure 3.11: PDL measurements from the second coil

One can observe that some of the losses in the fiber coil are polarization dependent and therefore contribute to filter the light as described previously.

3.1.5 Piezoelectric Transducer

For modulation of the light, a piezoelectric transducer (pzt) where used. The first cylinder used, had a radius of $12mm$, which expands/contracts when voltage is applied. The length of the fiber was $12.6m$. Due to the small radius of the cylinder, light was coupled out of the fiber core and lost. This pzt had a $43\%(2.4dB)$ loss at $1550nm$.

Due to the high losses, a pzt with larger radius was made. The radius now was $25mm$ and the length of the fiber was $10m$. This pzt had at $1550nm$ a loss of $16.2\%(0.77dB)$ which was a substantial improvement from the first.

A PDL measurement was done here as well, and the results are shown in Figure 3.12. The pzt had less polarization dependent loss than the coils and the couplers.

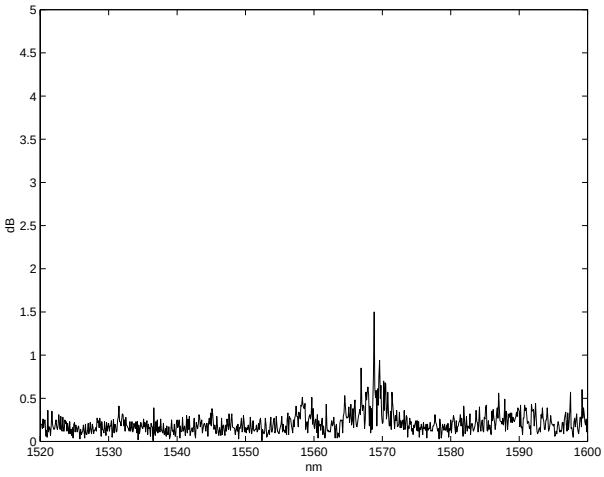

Figure 3.12: PDL measurements for the pzt

3.2 Preliminary study

After the study of different designs for the differential gyroscope, the serial design was chosen. To study this design in more detail, an experimental test setup was built. The aim for this first “model” was to verify the concept of the differential gyroscope based of the Sagnac effect, and to get a better understanding of noise mechanisms and limitations.

The components used for this preliminary study are mainly described in the previous section. Availability of the components was emphasized more than quality and requirements for the application involved. As new components became available and problems where solved, changes in the test setup was done. The first test setup included an erbium source, two 2x2 couplers, two PVC coils with around 410m of fiber, a detector including a detector circuit built on a breadboard, and an oscilloscope (setup shown in Figure 3.13).

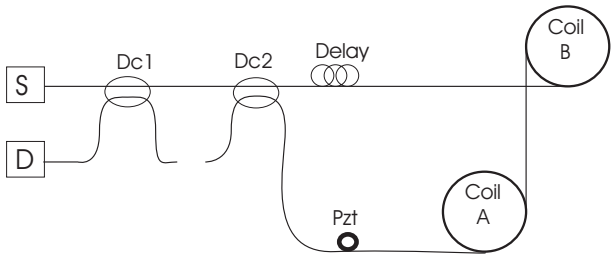

Figure 3.13: Differential gyroscope with two 2x2 couplers

The system was constructed, and when one coil was rotated, a sinusoidal signal was observed at the oscilloscope. This signal was proportional to the current generated at the detector, and consequently proportional to the sine of the rotation rate. When both coils were rotated together, a damped signal was observed compared to the first case (one coil rotation), but the common mode was not totally rejected. One reason was a length difference between the two coils of fiber due to problems in the winding process. This difference was minimized by splicing a length of fiber to the shortest coil. But, common mode rotation did still give a signal at the output. This “unwanted” signal was located to the fiber connecting the coils to the rest of the gyroscope. Until now, no polarization control was done in the system.

When the coils were rotating, the input and output fiber of the coil were bent in phase with the rotation since the couplers and the detector was at rest on a table. This induced a change in polarization for the two counterpropagating waves. The change in polarization changed the visibility V in the interference signal ($I = A + V \cdot \cos(\Delta\phi)$), and this was misinterpreted as a rotation signal. Further comments are made in section 3.3.

First, polarization controllers(pc’s) was included in the system. One between the two directional coupler, and the other between the second directional coupler and one of the coils. It was now possible to maximize the visibility, but since a polarization controller only gave a fixed change in the state of polarization (SOP), and not a fixed SOP, bending still induced a signal at the output. To avoid the problem of bending, the optical part of the differential gyroscope was put on a platform. To simulate common mode rotation, the entire platform was rotated. The drawback with this method was a reduced amplitude of the rotation (dynamic range), and a loss of control over the rotation (the platform was rotated

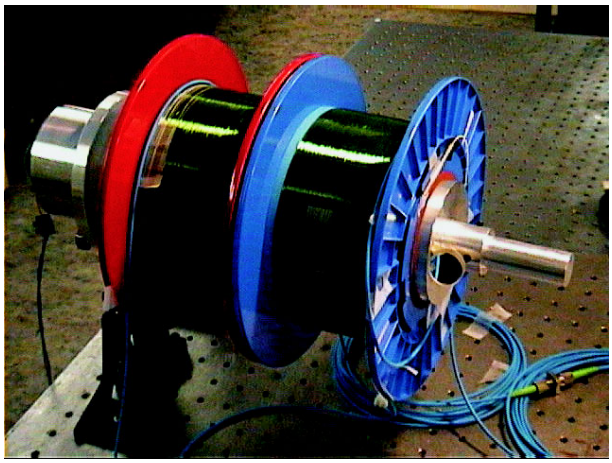

Figure 3.14: Both coils put on the shaft of the DC motor

manually).

Now, no signal was observed under common mode rotation, and therefore strenghtened the theory for the serial configuration.

The purpose of the polarization controllers is to obtain a similar SOP for the two counterpropagating waves, which gives the highest possible visibility. Since the erbium source sends out depolarized light, the pc between the two directional couplers did not change the visibility of the system. This pc was therefore removed. When controlling the second pc, a significant change in visibility was observed at the oscilloscope. This indicates that the optical components in some way filter the polarization of the light, and has been dicussed in the previus section.

The 2x2 couplers in the first model did not split the light 50/50 between the two output arms. This gave a substantial reduction of the output power. These two couplers were consequently changed with 50/50 couplers (3dB) to increase the power at the output (see section 3.1 for details).

3.2.1 Controlling the angular velocity

To control rotation rate, the coils were put on the shaft of a DC motor. The DC motor was controlled by a function generator, and a sinusoidal signal was used, which gave a sinusoidal rotation rate. When one sensor-coil was put on the shaft the torsion in a boat was simulated, and when both sensor-coils were put on the shaft, common mode rotation was simulated. Both modes (differential and common) however, could not be simulated at the same time.

Assuming the frequency of the tilting (rotation) to be known, and that the shaft of the motor actually rotates sinusoidally, the only factor needed to determine the rotation rate is the amplitude of the rotation. This amplitude was determined by sending visible laser light to a mirror positioned at the motor shaft, and observing the reflected beam at a nearby wall. The amplitude α_0 is then given by

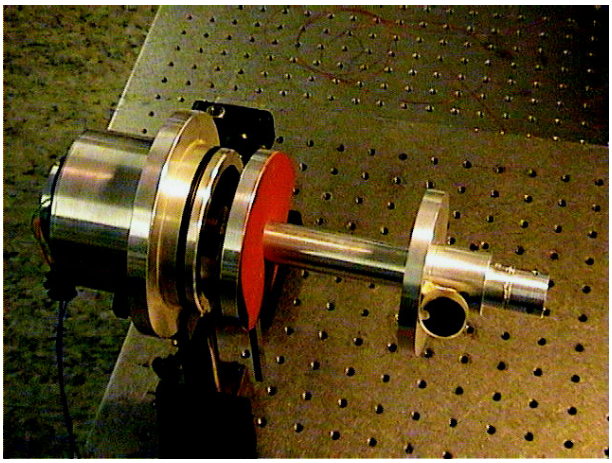

Figure 3.15: DC motor used for simulating boat movement

$$\alpha_0 = \frac{tan^{-1}(\frac{heigth\ \ of\ \ spot\ \ at\ \ maximum}{length\ \ to\ \ wall}) - tan^{-1}(\frac{heigth\ \ of\ \ spot\ \ at\ \ minimum}{length\ \ to\ \ wall})}{2} \tag{3.1}$$

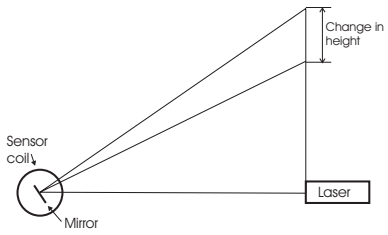

Figure 3.16: Geometrical description of how the amplitude of the rotation was determined

With the assumptions made above, the rotation rate is now known at all places since

$$\Omega = \frac{d}{dt}(\alpha_0 \sin(\omega t)) = \alpha_0 \omega \cdot \cos(\omega t)$$

where Ω is the rotation rate, α_0 is the amplitude of the rotation, and ω is the angular frequency of the rotation.

There are of course different and much better ways to control the rotation rate. But, this method is simple and easy to build and use, and does give enough accuracy to demonstrate the principle of a differential gyroscopes, so little effort was used to improve this verification method.

A problem encountered, was the DC motor deviation from sinusoidal tilting or rotation at low frequency and amplitude. This made it difficult to measure the smallest rotation rate possible for the fiber coils to detect. Therefore at low rotation rate a linear DC motor was introduced. The motor was connected to the coils by two extension bars made of PVC. This motor could give very small amplitudes and frequencies, but it also introduced “unwanted”

mechanical vibrations in the coil reducing the signal to noise ratio substantially. Few tests where therefore done with this motor.

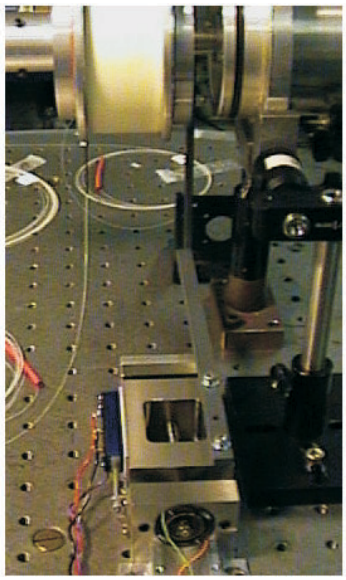

Figure 3.17: Linear DC motor used for small rotation rates

3.2.2 Demodulation with 2x2 configuration

The signal at the oscilloscope was given by equation 2.26. To retrieve the phase difference $\Delta\phi_R$, which is proportional to the rotation rate, a modulation/demodulation technique had to be applied. A common technique for gyroscopes will here be called stable bias modulation/demodulation, and is explained in section 2.3.1. A piezo electric transducer (pzt) was included in the system between the second coupler and one of the coils. The oscilloscope was replaced by a phase-locked amplifier, and an internal oscillator in the phase-locked amplifier produced a sine wave for the pzt (see Figure 1.3.A for design of the system). The amplitude of the phase-locked signal was sent to an A/D-converter and registered in a computer using a LabView program (the LabView program is listed in appendix D).

To lower the modulation frequency to a measurable level, a delay line had to be applied (see section 2.2). If not, the modulation frequency would have been around 120kHz. A delay line of 1550m was inserted in the system between the second coupler and the coils at the opposite side of the pzt. The total length between the pzt and the coupler (through the sensor coils and the delay line) was now 2410m. This should give an optimum modulation frequency of

$$f_{mod} = \frac{1}{2t} = \frac{c_0}{2L \cdot n} \approx 42kHz$$

This frequency coincided with one of the pzt's eigenfrequencies, so a modulation frequency of 30kHz was used. The use of a nonideal modulation frequency is described in [7].

The power observed at the detector are given from equation 2.26

$$V = V_L P_0 J_1(\phi_b)\sin(\Delta\phi_R) = V_L P_0 J_1(\phi_b)\sin(\frac{2\pi LD}{\lambda_0 c_0}\Omega)$$

where V_L is the generated amplitude from the phase-locked amplifier, P_0 is the input power, $J_1(\phi_b)$ (≈ 1.8) is the Bessel function from the first harmonic(see section 2.2), and $\Delta\phi_R$ is the Sagnac phase shift.

The rotation rate Ω was determined by the equation

$$\Omega = \frac{\lambda_0 c_0}{2\pi LD}\sin^{-1}(\frac{V}{V_L P_0 J_1(\phi_b)}) = \frac{1}{B}\sin^{-1}(\frac{V}{A}) \tag{3.2}$$

The factor B was calculated to be $B = 0.886$ (from the Sagnac effect). The factor A was determined by calibration, since both P_0 and $J_1(\phi_b)$ were difficult to calculate/measure. For this first model, B was determined by rotating one sensor coil by a known rotation rate, and solving the above equation (Eq 3.2) for the factor B. This calibration procedure must of course be improved before practical use, but the method was found sufficient for laboratory tests.

One possible method to calibrate the unknown factors before commercial use is first to measure the output at different rotation rates over the entire operating range, and at different temperatures or other important external factors (i.e. pressure).Then calculate the factors by an equation solver, with the external effects as variables. And in the end store the factors in the monitoring program (computer or microprocessor), with a sampling frequency of $1kHz$.

After measuring the factor A in the LabView program, monitoring of the output signal at different rotation amplitudes and frequencies where performed to test the systems repeatability and predictability.

In the figure below, a 1s sample of the output signal is shown, when the applied rotation had the shape

$$\alpha = \alpha_0 \sin(\omega t) = 0.0065\sin(25.1t)rad \tag{3.3}$$

The red graph represents the output on the computer (measured signal), while the blue (dotted) graph is a generated graph (in Matlab) from Eq. 3.3. The blue graph therefore representing the actual tilting/rotation. It must be emphasized that one parameter is determined by calibration, and that the phase of the calculated signal are fitted to the measured signal to make it easier to compare the two rotation rates (the phase of the calibration signal was not registered during the recording in the gyroscope).

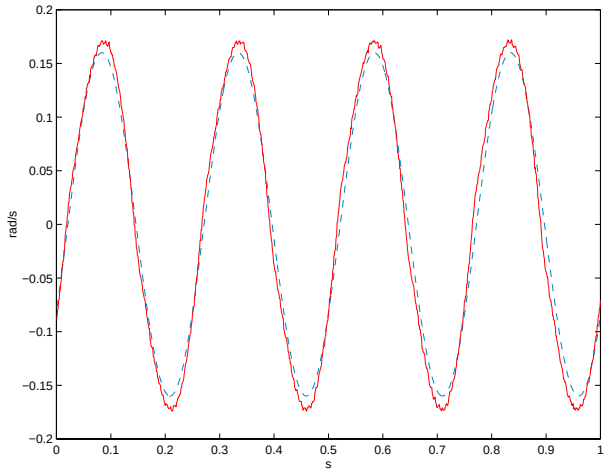

Figure 3.18: Example of registered rotation rate for first model, $\Omega = 0.163\cos(25.1t)$rad/s. Red graph:experiment, Blue (dotted) graph : theory

The two graphs in the figure are very similar, and therefore indicate the accuracy in the gyroscope. It is also worth noticing the large signal to noise ratio (> 30 in Figure 3.18).

Another 1s example is given i Figure 3.19. Here the frequency is around 3Hz and the amplitude of the tilting is $\alpha_0 = 0.0167$rad.

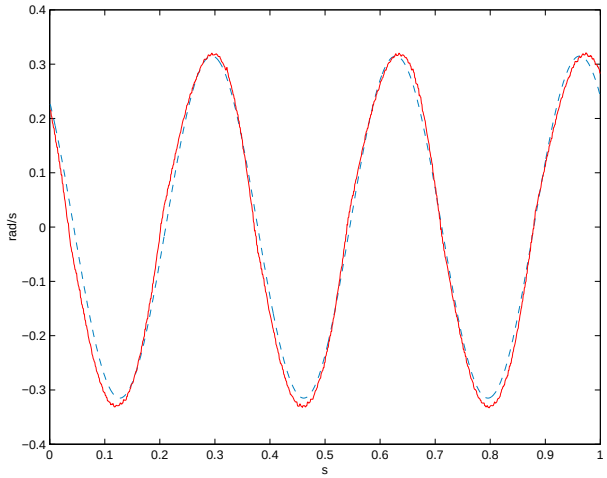

Figure 3.19: Example of registered rotation rate for first model, $\Omega = 0.315\cos(18.8t)$rad/s. Red graph:experiment, Blue (dotted) graph : theory

The two graphs are defined as in Figure 3.18. The Sagnac interferometer still follows the mechanical tilting, as expected.

The accuracy of the DC motor must be taken into account. The calculated rotation depends on an ideal sinusoidal rotation, and is therefore not necessarily correct. This is important to keep in mind when numeric results are presented.

Now, both sensors where put on the shaft of the DC motor, to simulate common mode rotation. A sinusoidal signal was sent to the DC motor, and the rotation rate was measured

both by the Sagnac interferometer and the laser spot (equal to the preceeding examples).

A frequency and an amplitude similar to the second example was used ($f \approx 3$Hz , $\alpha_0 = 0.0168$rad). The result is shown in Figure 3.20.

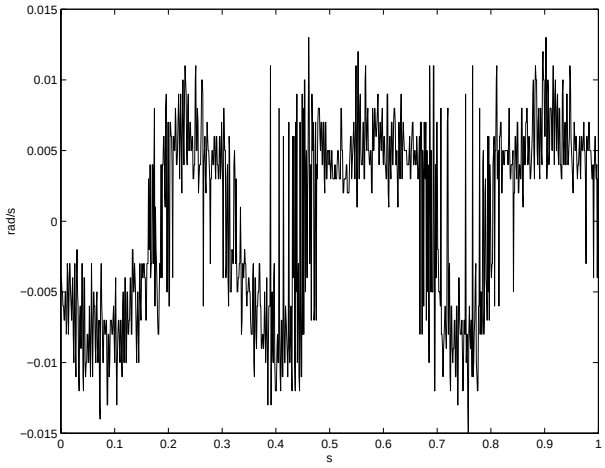

Figure 3.20: Example of registered rotation rate for the test setup

The signal is reduced compared to Figure 3.18 by a factor 32. This factor was in section 2.1 defined as the common mode rejection factor. Consequently, $\xi = 32$. The origin of the noise limiting this factor, are discussed in the next section.

As mentioned earlier in this section, a linear DC motor was used in order to reduce the amplitude and frequency of the rotation/tilting. The motor introduced mechanical vibrations that made the measured signal difficult to understand (Figure 3.21), but after applying a proper filter, the rotation signal was retrieved. In Figure 3.22 the filtered signal is shown. A Chebyshev type 1 filter was used with the cut off frequency of 10Hz. From the laser spot observed on the wall, the rotation did not seem totally sinusoidal, but if the rotation is fit to a sinusoidal pattern the calibration signal is as shown in the blue graph in Figure 3.22.

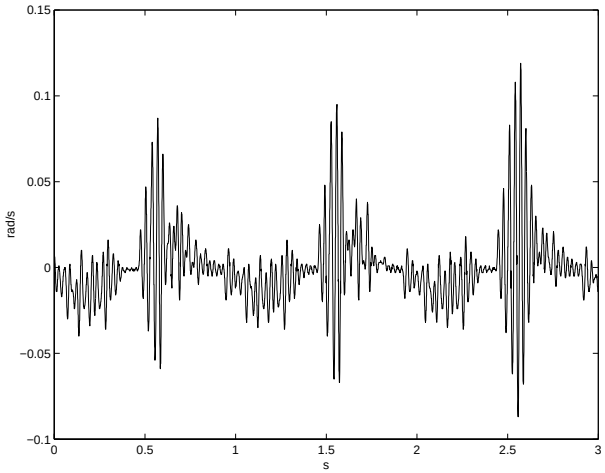

Figure 3.21: 3s sample from the measured signal before filtering when the rotation was approximately $\Omega = 0.013\cos(\omega t) rad/s$, $\omega = 6.28$

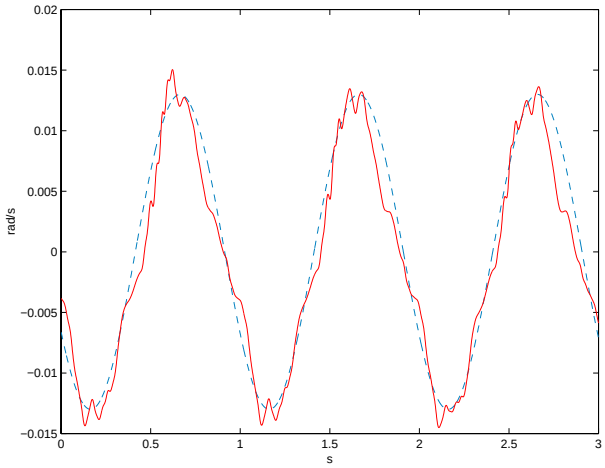

Figure 3.22: 3s sample from the measured signal after filtering when the rotation was approximately $\Omega = 0.013\cos(\omega t) rad/s$, $\omega = 6.28$. *Red graph:experiment, Blue (dotted) graph : theory*

The two graphs give almost the same amplitude and frequency, which at least gives hope for detecting rotation rates down to $3 - 4mrad/s$ ($\alpha_0 = 1mrad$ $f = 0.5Hz$). The origin of the large noise in the measured signal (before filtering), caused by mechanical vibrations from the DC-motor, was not fully investigated. One intuitive solution is that the mechanical vibrations have a large enough frequency to give a Sagnac phase shift as measured (even though the amplitude is very small). Another plausible explanation could be that the mechanical vibrations generates eigenfrequency vibrations in the coil, which modulates the fiber coil.

All the above examples are taken when the state of polarization for the two counterpropagating waves are very similar. Without any polarization control, the signal drifted slowly with time.

3.2.3 3x3 configuration

After the first tests descibed above, the two 2x2 couplers were substituted with one 3x3 coupler. The pzt and the phase-locked amplifier were removed, and the signal from the detector circuit was digitized and processed on line using a PC. The sampling frequency was also here set to $1kHz$.

First, the mathematical operations for retrieving the rotation rate as described in section 2.2 were tested. The rotation rate should be found according to equation 2.47

$$\frac{(V_2 - V_3) + f_1 V_1}{(V_2 + V_3) - f_2 V_1} = f_3 \frac{\sin(f_6\Omega + f_4)}{\cos(f_6\Omega + f_5)}$$

where V_1, V_2 V_3 are the output voltages, Ω the rotation rate, and $f_1 - f_6$ are constants. To find the constants, the following procedure was used. The factor f_6 was calculated (theoretically), since it is given by the Sagnac effect ($f_6 = \frac{2\pi LD}{\lambda_0 c_0}$). One now have five

factors to determine. The output voltages was measured for known rotation rates, giving five nonlinear equations. To make sure the solved constants were correct, more than five rotation rates were measured, yielding an overdetermined set of equations. The set of nonlinear equations were solved in a nonlinear equation solver (Matematica). Here a problem arised though, since the solutions varied with the set of equations used, and in some cases, no solution was found. When trying to implement the different solutions in the experimental setup, the different solutions did only give a correct result for a small range of rotation rates.

After the first failure, a simplified model was tested. This model is descibed in [8]. This model also assumes an ideal system, but it is much more surveyable and easier to implement. The idea is that in an ideal Sagnac interferometer with a 3x3 coupler, the difference between the two output signals containing the rotation rate, is proportional to the sine of the Sagnac phase shift

$$V_2 - V_3 = A \cdot \sin(\Delta\phi_R) \tag{3.4}$$

Here A is a constant and V_2 and V_3 are as defined above

The model was implemented in the LabView program, and the constant A was found by measuring at a known rotation rate. This model showed to be more repeatable and predictive. Examples of the measured rotation rate are given in Figure 3.23 and Figure 3.24. Like in the previous subsection, the red graph represents the measured signal, and the blue graph represents the calibration signal (calculated rotation, Eq. 3.1).

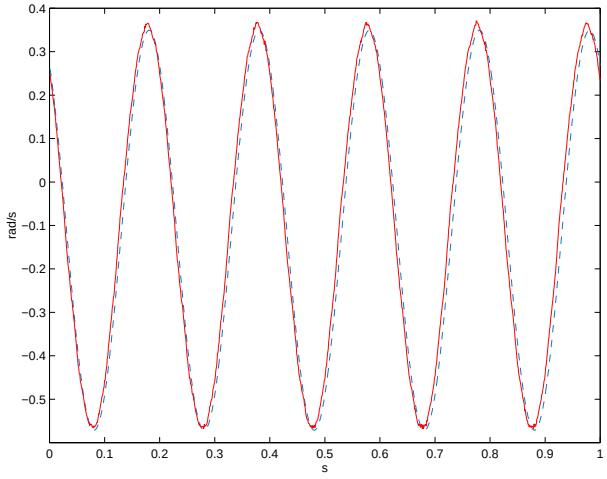

Figure 3.23: Example of registered rotation rate for first model with the use of a 3x3 coupler. Here, $\Omega = 0.460\cos(\omega t) rad/s$, $\omega = 31.4$ *Red graph:experiment, Blue (dotted) graph : theory*

Figures 3.23 and 3.24 indicate good agreement between the measured rotations rate and the calculated rotations. But, the signal is not balanced around zero, due to unequal split ratios (gives unequal voltage measurements for the two detectors). This can make the integration from rotation rate to angle of rotation more difficult.

Both of these measurements are taken when the SOP for the two counterpropagating waves

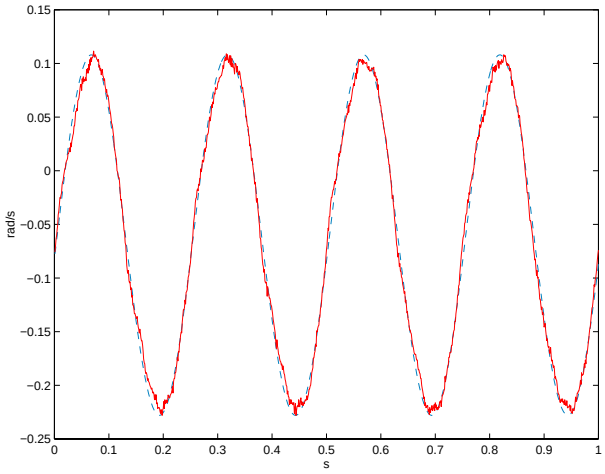

Figure 3.24: Example of registered rotation rate for first model with the use of a 3x3 coupler. Here, $\Omega = 0.168\cos(\omega t)rad/s$, $\omega = 25.1$. *Red graph:experiment, Blue (dotted) graph : theory*

are similar. It was however, more difficult to determine when the SOP's was most similar, compared to the stable bias modulation/demodulation technique.

The problems relating to the polarization fading are indicated in Figure 3.25. The figure shows the measured signal when the SOP's are very similar (green graph), and measured signal when similarity between the SOP's are close to minimum (red graph). The blue graph is still the calibrated signal. The difference in phase between the two measured signals are due to the fact that the two signals are recorded at different times, and are consequently of no importance.

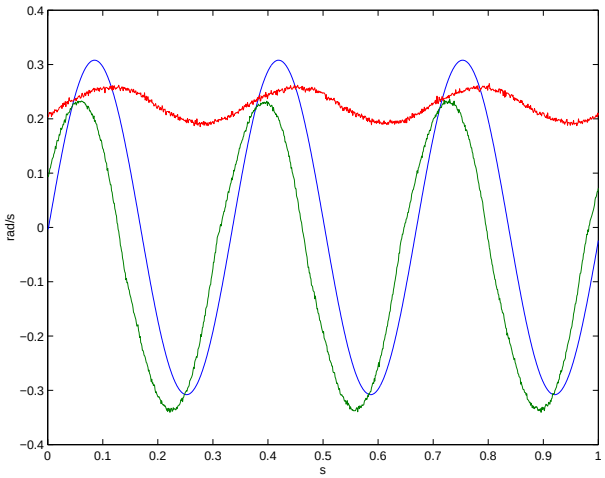

Figure 3.25: Rotation rate for different SOP. The blue graph represent the calibrated signal, the red graph represent the rotation signal when the SOP's are similar, and the red graph indicate when the SOP's are not similar. Here, $\Omega = 0.308\cos(\omega t)rad/s$, $\omega = 18.8$

The two signals have the same frequency, but the amplitudes are very different. While the green graph give a good estimate of the actual rotation, the red graph gives much smaller rotation rate.

When it comes to common mode rejection, the 3x3 “demodulation” method also reduces the signal. Both coils where now put on the shaft of the DC motor, and the motor was started. Figure 3.26 shows the rotation signal when the rotation rate was as in Figure 4.22

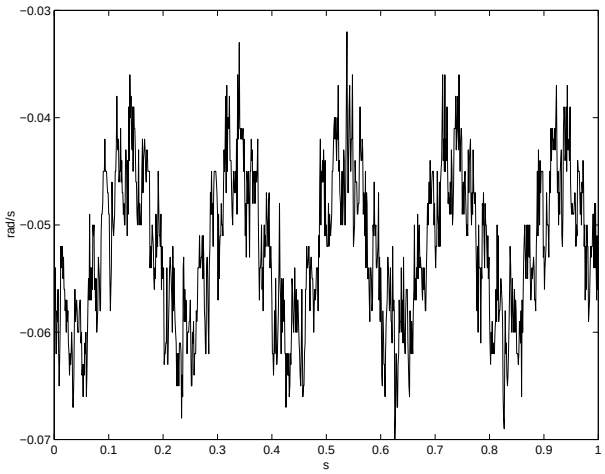

Figure 3.26: Common mode rotation for a 3x3 setup with $\Omega = 0.46\cos(\omega t)rad/s$, $\omega = 31.4$ *rotation rate applied*

The common mode rejection factor was here measured to be

$$\xi = 38$$

which was close to the factor measured in the stable bias setup.

3.3 Polarization

One of the main problems during the experiments was how to control the polarization. In the test setup, no polarization controlling devices were used. Two different kinds of polarization problems were then experienced; long term signal fading, and rotation dependent polarization fluctuations.

The long term polarization fading was caused by external effects (i.e. temperature and pressure) working on the fiber and slowly changing the polarization. The visibility of the interference is dependent of polarization. If the two interfering waves have orthogonal polarization, no interference will be observed, and if the polarization is equal, maximum visibility will be obtained ($V = 1$). The long term polarization fading will consequently change the visibility, which again will change the intensity.

$$I = A + V(t) \cdot \cos(\Delta\phi_R)$$

This slow drift in intensity was observed (Figure 3.27), and made it difficult to compute the scale factor, and compare samples taken at different times. The figure show the maximum amplitude over two hours. A constant sinusoidal signal was sent to the DC motor, and the system was left alone for a couple of hours. Within that period of time, the measured rotation rate changed almost $0.1 rad/s$ due to polarization fluctuations.

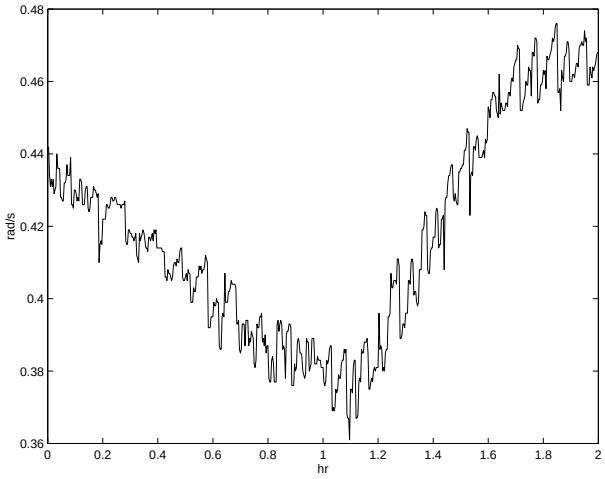

Figure 3.27: Max amplitude recorded during two hours illustrating long term polarization fluctuations

The introduction of polarization controllers in the configuration made it possible to change the polarization so that the SOP for the output waves was similar, and visibility close to maximum was obtained. This would not solve the fading problem, unless the polarization controller would be controlled continously. A feedback loop from the detector to the polarization controller was considered, but since it was difficult to use this to solve the rotation dependent polarization fluctuations described below, no such feedback loop was built.

The second problem was fluctuations due to rotation. In ordinary fiber gyroscopes the optical components are fixed compared to eachother. This is not the case in the experimental test setup here. The two sensor coils will rotate compared to each other and to the rest of the optical components. This induces stresses and strains in the fiber connecting the components, which in turn change the polarization depending on how the fibers connecting the parts are moving relative to each other. This may be the reason for the observed common mode signal. Like for the long term signal fading, the polarization fluctuations changes the visibility, and consequently the intensity. The fluctuations (bending) have the same frequency as the rotation, which makes them difficult to separate from the signal generated due to the the Sagnac effect.

An important comment here, is that the problem described above will not occur in an practical implementation on a ship. On a ship, everything will be fixed compared to each other, while the ship is rotating.

It must be emphasized that polarization fluctuations are only a possible reason for the common mode signal. But, the polarization controller showed clearly that bending of the fiber changed the polarization in the two counterpropagating waves differently, otherwise the visibility would not change while moving the coils in the polarization controller.

In section 3.1 the polarization dependent loss (PDL) for some of the components was introduced. Both the couplers and the fiber coils showed some PDL. One knows that the source sends out unpolarized light, but since some of the components filter out some of the SOP’s, the light interfering at the output is partially polarized. Consequently, if the two polarizations change compared to eachother, the visibility will change as well, since the visibility is polarization dependent (for polarized and partially polarized light).

One of the most common methods to solve polarization problems in fiberoptic gyroscopes is to use polarization preserving fibers. In polarization preserving fibers, the light will only propagate in one state of polarization (ideally), and the interfering waves will consequently have a fixed and similar SOP at the output. A second method now becoming increasingly popular is the use of depolarizers. Such a depolarizer has been studied in appendix A.6.

When the Lyot depolarizers were introduced, the long term polarization fluctuations were reduced as well. The two hour test were performed (described above), and the results for the stable bias modulation/demodulation setup are shown in Figure 3.28

The results for the 3x3 demodulation setup are shown in Figure 3.29 From these results one can see that the depolarizers improve the stabilization of the output, and are consequently a possible solution to the long term polarization fading. In these plots one has assumed that the rotation rate was constant over the time of measurement. This is not exactly true. The rotation rate was reduced after the two hours, and consequently contributed to the small fading observed in the figures.

When operating the system in common mode, the common mode signal was substantially reduced when the depolarizers were used, and will be described in detail in the next section. However, this strengthens the theory of the rotation dependent polarization fluctuations described earlier in this section.

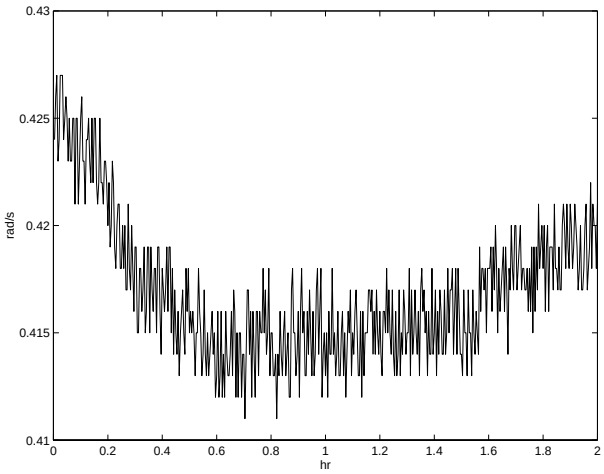

Figure 3.28: Maximum amplitude taken over 2 hours illustrating long term polarization fading with the stable bias modulation/demodulation including depolarizers

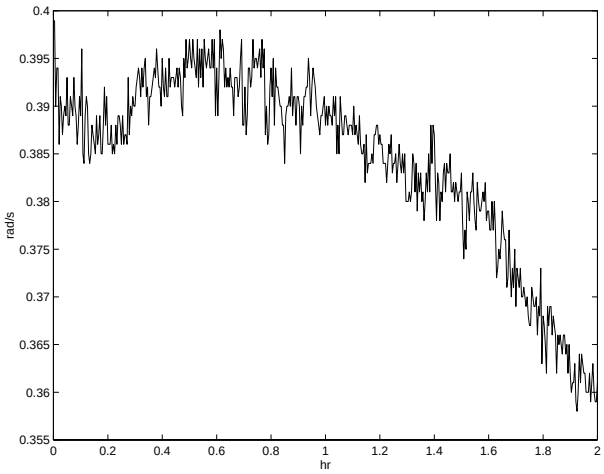

Figure 3.29: Maximum amplitude taken over 2 hours illustrating long term polarization fading with the stable bias modulation/demodulation including depolarizers

3.4 Technology demonstrator

The experimental test setup was used to verify the concept of a differential gyroscope, to get a better understanding of limiting factors and noise, and to develop demodulation techniques. From this preliminary study a setup was recommended, and a demonstrator was built. Both the “stable bias” and the “3x3” demodulation techniques were tested in the demonstrator.

The fiber coils with an aluminium spool were described in section 3.1, and had a fiberlength of 677m. The average diameter was 0.103m. The Sagnac effect should consequently be larger in this demonstrator, and therefore be able to detect smaller rotation rates than the preliminary test setup. As concluded in section 2.1 a serial configuration was chosen, and for this setup an extra fiber length was used between the coupler and the coils, and between the two coils. This was done to be able to simulate external effects on the fiber connecting the parts in a boat, and to make the system more realistic. The system was thought implemented on a large ship, so the lengths were chosen to be 50m between the couplers and the coils, and 100m between the two coils. Also, as a possible solution to the polarization problems, Lyot depolarizers were introduced, one at each side of the Sagnac interferometer (between the coupler and the coils).

3.4.1 Stable bias modulation/demodulation

The final model had a design as shown in Figure 3.30 for the “stable bias” modulation/demodulation,

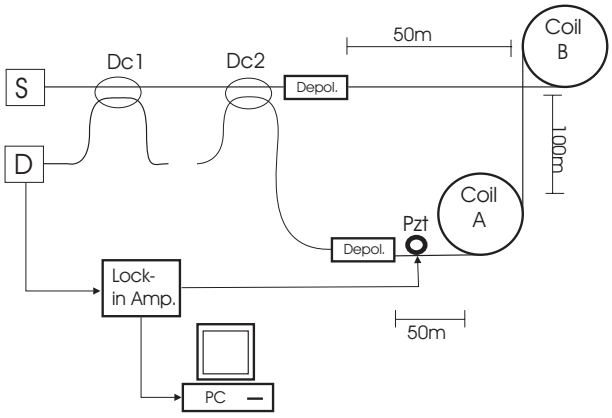

Figure 3.30: Final model for the 2x2 configuration

The figure gives a misleading picture of the fiber connecting the coils and the directional coupler. As mentioned in section 2.3 the fiber connecting the parts must be placed so that they do not introduce a new Sagnac interferometer. Therefore, the fiber connecting the two coils were put close together to the fibers connecting the coils to the directional coupler.

The total loss for this system was

$$Loss = 17.9dB = 98.4\% \pm 0.5\%$$

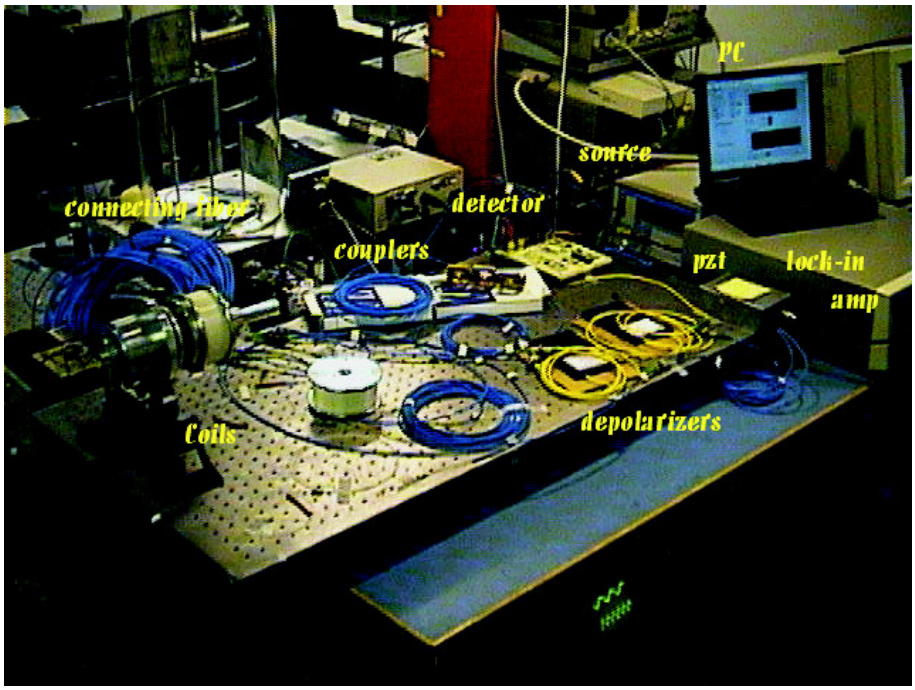

Figure 3.31: Setup using the stable bias modulation/demodulation techique

As described in section 3.2, the measured signal had the form

$$V = V_L P_0 J_1(\phi_b)\sin(\Delta\phi_R) = V_L P_0 J_1(\phi_b)\sin(\frac{2\pi LD}{\lambda_0 c_0}\Omega) = A \cdot \sin(\frac{2\pi LD}{\lambda_0 c_0}\Omega)$$

The factor A was determined by calibration. In this demonstrator, the calibration procedure was done as follows. The signal was measured for different rotation rates, and the factor A was calculated for each rotation rate. The mean of the calculated factors was used.

New rotation rates were applied, and the rotation rate was measured according to the formula

$$\Omega = \frac{\lambda_0 c_0}{2\pi LD}\arcsin(\frac{V}{A})rad/s$$

Figure 3.32 and Figure 3.33 shows examples of a 1s sample from two different rotation rates

The two figures show good similarity between the calculated and the measured signal for two different rotation rates. It must be commented again, that the factor A was calibrated from the calulated signal, and that the phase of the calculated signal was fitted to the measured, to make it easier to compare the calculated and the measured signal.

Figure 3.34 shows the deviation from the calculated rotation rate in $\%$. Different sinusoidal rotation rates were applied, and the amplitude $\Omega_{max} = \alpha_0\omega$ was used in the plot. It can be seen that the deviation for small rotation rates are larger (in $\%$) for small rotation rates. It is also worth noticing that all but one of the measured results give a lower measured rotation

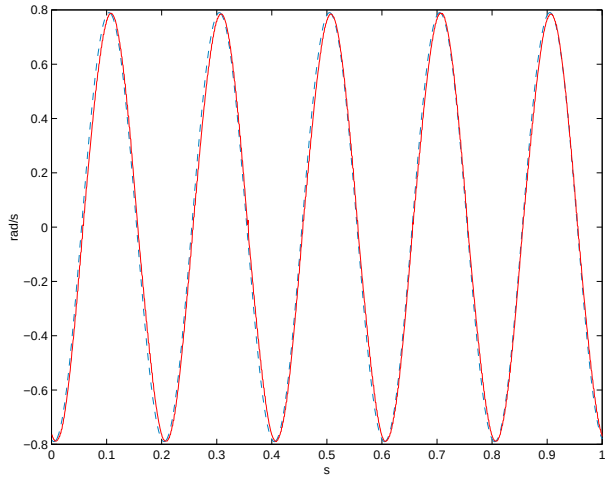

Figure 3.32: *1s sample for the measured signal when the applied rotation rate was* $\Omega = 0.79\cos(\omega t) rad/s\ ,\ \omega = 31.4$. *Red graph:experiment, Blue graph : theory*

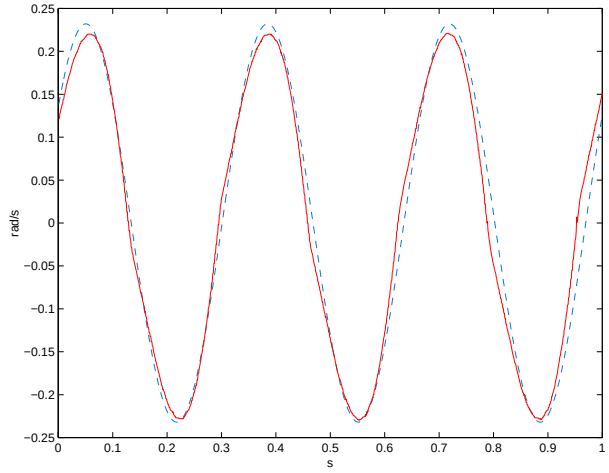

Figure 3.33: *1s sample for the measured signal when the applied rotation rate was* $\Omega = 0.23\cos(\omega t) rad/s\ ,\ \omega = 18.8$. *Red graph:experiment, Blue graph : theory*

rate than the calculated. This indicates that the factor A was recorded to high during the calibration procedure.

Figure 3.35 show rotation in common mode for the rotation $\Omega = 0.376 \cdot \cos(25.1t)$rad/s.

In section 2.1 the common mode rejection factor was introduced. The factor was introduced to give an indication of the common mode rejection. The common mode rejection factor was measured to be

$$\xi(0.376) = \frac{0.38}{1 \cdot 10^{-3}} = 380$$

This is a substantial improvement compared to the factors measured in the preliminary study. The noise was in the same order or below the resolution of the A/D converter, and this is the reason for the constant amplitude in the plot. The exctinction factor was in the

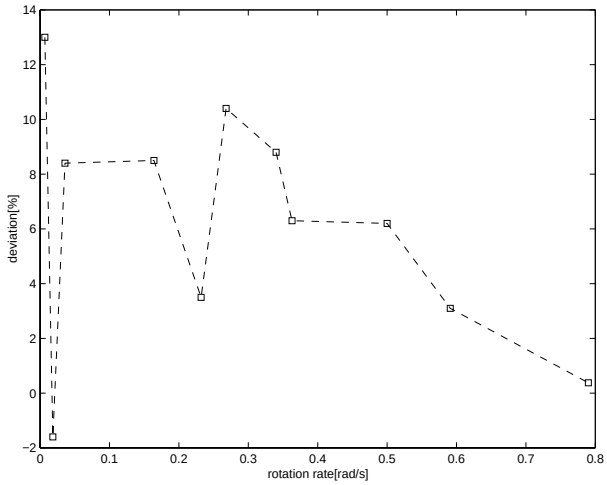

Figure 3.34: Deviation from the calculated rotation rate as a function of the rotation rate. The squares represents the measurements

technology demonstrator much more dependent on the rotation rate, than in the preliminary study. The reason is that in this test, other sources than difference in length and diameter dominated the noise. As one can see from the figure, not even after the lowpass filtering did, the measurement show any sign of common mode rotation. The reason for the improvement in common mode rejection factor was the deplorarization of the light, as discussed in section 3.3, so that rotation dependent polarization fluctuations were reduced.

3.4.2 3x3 demodulation

The setup for the ”3x3” demodulation is shown in Figure 3.36.

The total loss in the 3x3 configuration was measured to be

At output port 1:

$Loss = 15.1dB = 96.9\% \pm 0.5\%$

At port 3:

$Loss = 14.6dB = 96.5\% \pm 0.5\%$

The demodulation method described in section 2.2 was tested, but failed once again in determining the coefficients (see section 3.2). So the simplified method described in the preliminary study was used again. The factor A was determined by calibration as described for the “stable bias” setup.

$$V_2 - V_3 = A \cdot \sin(\Delta\phi_R)$$

After the calibration, different rotation rates were applied. Two examples are shown in Figure 3.37 and 3.38.

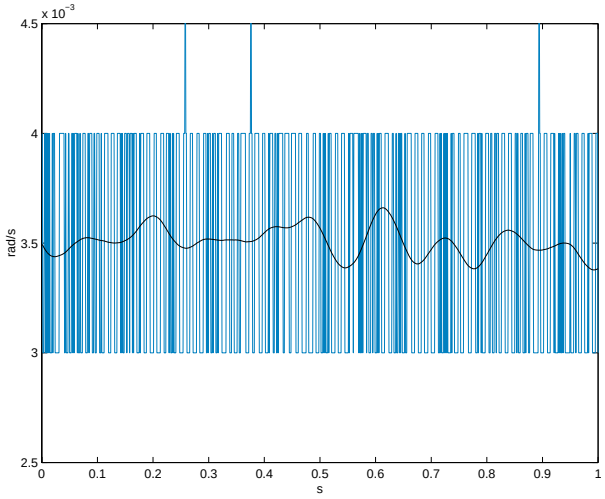

Figure 3.35: *1s sample for the measured signal when a common mode rotation signal of* $\Omega = 0.376\cos(\omega t) rad/s$, $\omega = 25.1$ *was applied. The blue graph represents the measured signal, while the black graph indicates the signal after a lowpass filter (Chebyshev type1 with 10Hz cutoff)*

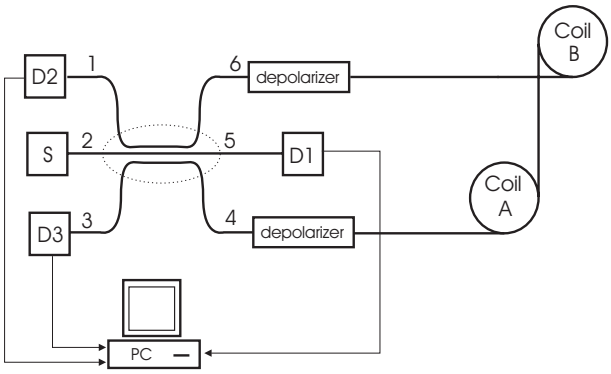

Figure 3.36: *Final model for the 3x3 configuration*

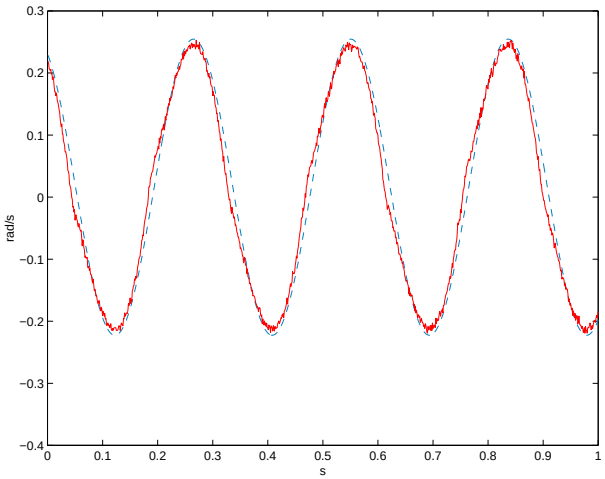

Figure 3.37: *1s sample for the measured signal when the applied rotation rate was* $\Omega = 0.24\cos(\omega t) rad/s$, $\omega = 22.0$. *Red graph:experiment, Blue graph : theory*

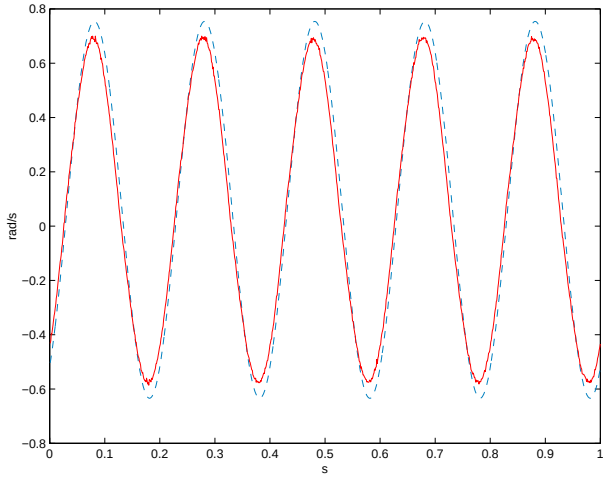

Figure 3.38: 1s sample for the measured signal when the applied rotation rate was $\Omega = 0.69\cos(\omega t) rad/s$, $\omega = 31.4$. *Red graph:experiment, Blue graph : theory*

Both figures show a relatively good similarity between the measured and the calculated signal. But, as in the preliminary study, the oscillation is not symmetric around zero, which can be a problem when integrating to obtain angle of rotation. The deviation from the calculated rotation rate as a function of the rotation rate are shown in Figure 3.39.

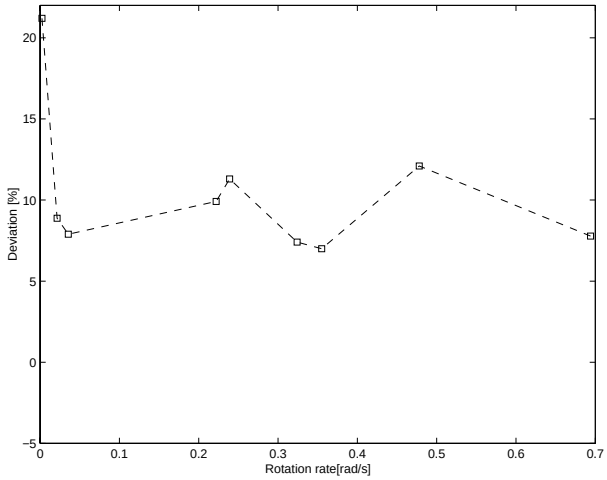

Figure 3.39: Deviation from the calculated rotation rate as a function of the rotation rate. The squares represents the measurements

As seen from Figure 3.39 the calibration was poor. All the measured results yielded a rotation less than the actual rotation. The deviation from the calculated signal was relatively constant for the different measurements (around $+8\%$). This indicates that an improved calibration (measurement of factor A), would improve the results substantially.

The common mode rejection factor was measured and found to be

$$\xi(0.333) = \frac{0.333}{5 \cdot 10^{-3}} = 67$$

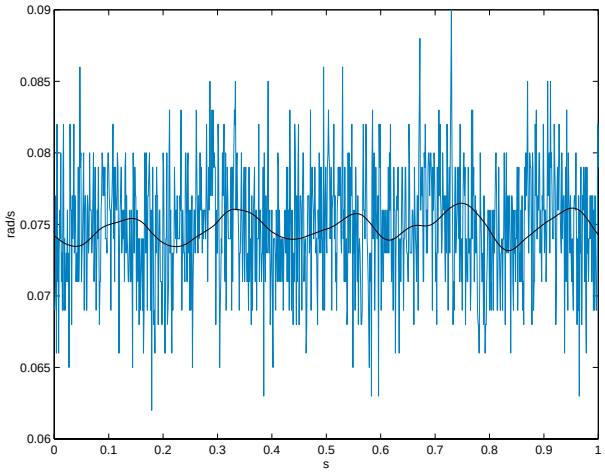

Figure 3.40: 1s sample for the measured signal when a common mode rotation signal of $\Omega = 0.333\cos(\omega t) rad/s$, $\omega = 31.4$ *was applied. The blue graph represent the measured signal, while the black graph indicates the signal after lowpass filtering (Chebyshev type1 with 10Hz cutoff)*

This is not as good as for the stable bias modulation/demodulation. One possible reason is that the lock-in amplifier reduces noise since it only detects modulation frequencies in a very narrow band. But, from Figure 3.40 the filtered signal could be recognized as a rotation signal, and this can not be explained with the reduced noise.

If the lowpass filtered signal are used in the common mode rejection factor, the factor would be

$$\xi = 266$$

Which is a very good result.

4 RESULTS AND DISCUSSION

This thesis discuss a wide range of problems regarding a differential fiberoptic gyroscope for hull monitoring applications. Since no similar work was found, both requirements for the application involved, and the concept of differential rotation measurements had to be developed. Requirements and considerations regarding implementation was commented in section 2.3, and the concept of a serial configuration was described in section 2.1.

The theoretical study stated some distinct differences between the requirements for an ordinary and the differential fiberoptic gyroscope.

In the application of hull monitoring, the static component of the torsion is of little interest. One can consequently remove all DC components without loss of important data. This leads to some useful simplifications. First, the system will not accumulate noise as a function of time. Since the noise in the system are relatively constant over time, one can reduce the requirements to the scale factor. And, reduced requirements to the scale factor reduce the requirements for the demodulation techinque. Open loop configurations are therefore of interest. Another advantage due to the removal of DC components is the simplified integration, since monitoring displacement (torsion angle) requires integration of the rotation rate.

The differential gyroscope is complicate as compared to the ordinary due to the increase in length and reduced control over the connecting fiber. This leads to a reduced control over sources of error.

In the preliminary test setup, design problems were investigated. First, the Sagnac effect was verified by observing the intensity at the detector when one coil was rotated. By introducing two sensor coils instead of one, and by connecting the two coils according to section 2.1, the differential gyroscope concept was tested. When both coils were rotated together, a reduced signal was observed compared to one coil rotation. The experiments showed that the difference in effective area of the two coils was crucial. When this area was almost equal in the two coils (within the limits given in section 3.1), and problematic effects such as polarization fluctuations were eliminated, a very good common mode rejection was observed. From the preliminary studies it was suggested that the signal observed under common mode rotation could arise from polarization fluctuations due to bending of the connecting fiber. This hypothesis was strengthened by the testing the demonstrator. The demonstrator included Lyot depolarizers, and tests showed a significant improvement in the common mode rejection.

The preliminary studies also included studies of noise effects. Special attention was given acoustic pickup. Sound appeared as noise in the system, and was dominating when a delay coil was used in the stable bias configuration. Both noise from the coils and from the connecting fiber were studied, and are discussed in the next section.

The next step was to find techniques for retrieving the rotation signal. Two demodulation techniques were proposed, the “ stable-bias” and the “3x3”. Other demodulation techniques may be applied as well. We have chosen a well established method, the stable-bias, and one method still under devekopment, the 3x3 demodulation. The stable-bias was chosen to be sure that at least one of the demodulation techiques gave a correct demodulation. The 3x3

demodulation techique was chosen due to its simplification of the design, and because of its growing use in interferometric systems. The 3x3 demodulation technique is passive, which is an advantage both to cost and to reduce the complexity of the system. It has been an objective of this thesis to gain experience with such 3x3 couplers in interferometric systems.

If the two demodulation methods are to be compared, the stable bias showed the best results. The signal from this modulation/demodulation technique was easier to calibrate, and gave a signal balanced around zero (no voltage observed when no rotation was applied). The scale factor accuracy was not very different for the two demodulation techniques. The great advantage of the 3x3 method is the simplicity in its design, since it does not depend on a modulation signal. The model for retrieving the rotation signal assumed an ideal system, and was one of the reasons why the 3x3 setup did not perform as well as the stable bias setup, together with the problem of setting the polarization controllers. Both methods follow the calibrated signal to a certain degree, but they both had a problem with signal fading (the 3x3 method a bit worse than the stable bias).

In the demonstrator, two Lyot depolarizers were used. These depolarizers solved some polarization fading problems as discussed in section 3.3. Some drift in the signal was still observed, and this lead to a problem in the calibration procedure. The introduction of the depolarizers also reduced the signal observed during common mode rotation.

There was no time to develop a setup where both common mode and differential mode could be applied at the same time. The detection of a small differential rotation when a large common mode rotation was present, has therefore not been verified experimentally. It was also difficult to verify that the sensor coils could detect a signal down to $1mrad$ with a frequency of around $0.5Hz$ as required, due to the distortion of sinusoidal rotation of the DC motor at such low rates. The experiments done with the linear motor indicated that a small rotation was observed, but that the accuracy was reduced. One possible reason for the reduced accuracy might be the inaccurate calibration. It is important to keep in mind that the dynamic range of the Sagnac interferometer is defined by the length and diameter of the coil. The resolution can consequently be customized to the application of interest.

One of the criterias for the sensor (described in section 2.3) was that it should be easy to install and take down (in a ship). The system developed here should meet these requirements. The system mainly consist of three parts. A main part containing source, coupler(s), pzt (if necessary), detector with detector electronics, phase-locked amplifier(if necessary), and monitoring electronics (PC, microprocessor, etc.). The two other parts are the two sensor coils. The entire system is connected with pig-tailed fibers (as simulated in the final model), and is consequently easy to install and remove. If one part fails, it should also be easy to substitute this part. Conclusively, the practical implementation of such a system should be possible. The greatest problem is to get the two sensor coils aligned, as commented in section 2.3.

4.1 Noise

4.1.1 Fundamental limit in rotation sensing

The fundamental limit for rotation sensing arise from the quantum noise limit, and is called photon shot noise. The uncertanty $\delta\Omega$ in the measurement caused by shot noise can be expressed as [17]

$$\delta\Omega \approx \frac{c_0 \lambda_0}{2LD\sqrt{n_{ph}\eta_D \tau}} \tag{4.1}$$

where L is the length of the fiber, D is the diameter of the fiber coil, n_{ph} is the number of photons leaving the interferometer, η_D is the quantum efficiency of the photo detector, and τ is the averaging time.

The derivation of this formula will not be presented here, but can be found in [18].

By applying constants typical for the system developed in this thesis, an estimate for the shot noise can be made

$$L = 1.6km \ , \ D = 0.1m \ , \ \eta_D = 0.3 \ , \ \tau = 0.1s$$

$$n_{ph} = 6 \cdot 10^{14} photons/s \ \ (corresponds\ to\ 0.2mW) \ , \ \lambda_0 = 1550nm$$

$$\Rightarrow \ \ \delta\Omega = 3.43 \cdot 10^{-7} rad/s \tag{4.2}$$

This noise is below the rotation rate of interest, and will consequently not degrade the system.

4.1.2 Acoustic noise

In the test setup, a delay fiber had to be applied in the system in order to reduce the modulation frequency. According to section 2.1, this delay line will make the system more responsive to acoustic noise. One of the coils was exposed to a significant acoustic field, and the output was measured. Already at a few kHz the acoustic noise had begun to show up. Figure 4.1 illustrates a rotation signal when 7kHz was applied.

If the loudspeaker was moved close to one of the connecting fibers, a similar result was obtained, but theere was much less noise. Even though the connecting fiber is more responsive to the frequencies applied, acoustic signals work over a larger area when applied to a coil. This is the reason why the signal was noisier when a acoustic signal was applied to the coil.

In the demonstrator, there was no need for a delay line, since the fiber length in the coils had been increased. The modulation frequency was now $f_{mod} = \frac{1}{2\Delta t} = 63kHz$ (see section 3.2 for explanation). This reduced the responsivity to acoustic noise substantially. The same

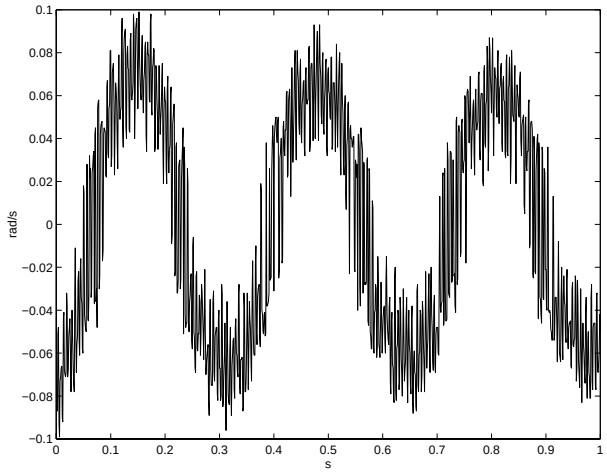

Figure 4.1: A rotation signal when a 7 kHz acoustic signal is applied close to one coil

test as above was carried out, but little increase in noise was found within the operating range of the loudspeaker, which was at least $20kHz$. But the system will pick up acoustic signals around the modulation frequency, and this will introduce noise. Some of this noise can be filtered out by signal processing, but this has not been studied here.

4.1.3 Thermal gradient induced noise

One major problem for fiber gyros is temperature gradients [19]. If one part of the fiber coil is heated, the fiber will change its index of refraction and consequently change the phase of the propagating light (the phase shift due to length change is small compared to the change in index [7]). This change in index of refraction will be observed at different times for the two counterpropagating waves. When integrating this effect over the heated area, the phase change can be significant. From the Sagnac formula one can see that the Sagnac effect is not dependent of the index of refraction. It is important to distinguish the thermal noise from the Sagnac effect, even though both operate in a Sagnac interferometer. The Sagnac effect is a relativistic effect, and gives a contribution to the phase that is not dependent of the index of refraction. Thermal gradients cause a change in index of refraction, and this phenomenon on the other hand is a time-varying phenomenon.

The phase shift due to thermal gradients was also observed experimentally, and one of the reasons for choosing an aluminium spool for the demonstrator, was the high thermal conductivity. In the preliminary study, one also suspected that some of the large fluctuations when the coil was heated was caused by polarization fluctuations as experienced with the bending of the fiber. The error introduced by thermal gradients was reduced in the demonstrator, but not removed as seen in Figure 4.2 and 4.3

One can see from the two figures that thermal gradients can have a significant effect on the measured signal. It was specially when a rotation was applied that the large differences was measured.

There was no time for further investigation around this problem.

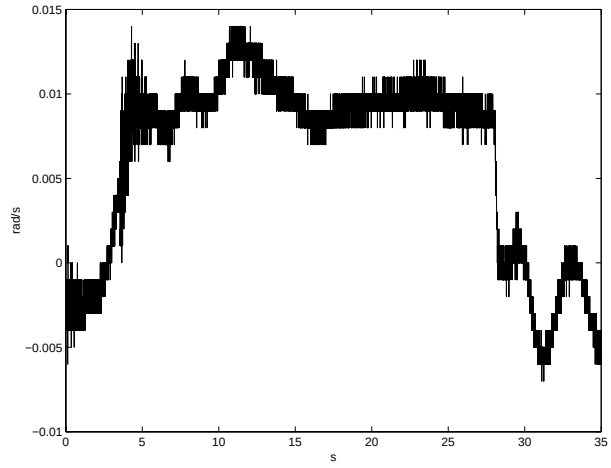

Figure 4.2: A 35s sample of the signal output when one of the sensor coils was heated. Here, no rotation was applied

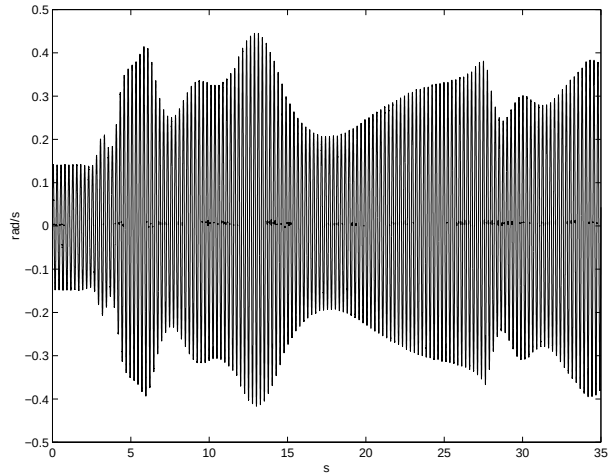

Figure 4.3: A 35s sample of the signal output when one of the sensor coils was heated. Here, a rotation rate with amplitude of $0.28rad/s$ was applied

4.2 Demonstrator performance characteristics

As a conclusion, some specifications for the demonstrator will be given. The list below is not complete. A missing factor is the lower frequency limit where the rotation rate can be measured accurately. A $0.5Hz$ with $1mrad$ amplitude was recognized, but no tests at lower rotation rates was carried out. This factor was difficult to measure, due to problems with the DC motors at such a low rotation rate, and a theorectical limit is dependent on the electrical part of the system, which was not a major issue in this project. An estimate is therefore not included.

According to section 2.1, the rate of the common mode rotation does not have any influence on whether common mode is rejected or not. Common mode rejection is idealy only dependent on the difference in effective area between the two coils, given by the common mode rejection factor, and can be tailored by careful engineering of the coils. Maximum common mode rotation for a given rejection factor will be determined by the acceptable

Max. rotation rate differential mode	$\Omega_{max} = 1.42 rad/s$ (stable bias mod./demod.)
	$\Omega_{max} = 1.11 rad/s$ (3x3 demod.)
Expected operating range	$3 \cdot 10^{-3} - 1.06 rad/s$ $\alpha_0 = (1 - 18 mrad)\ ,\ f = (0.5 - 10) Hz$
Common mode rejection factor	$\xi = \frac{1}{1 - \frac{L_1 D_1}{L_2 D_2}} = 100$ (theoretical from uncertanty)
	$\xi = 67$ (measured 3x3 demod.)
	$\xi = 380$ (measured stable bias mod./demod.)
Scale factor accuracy	$\approx 10\%$

Figure 4.4: Specifications for the demonstrator

influence on the internal rotation measurement. Another practical limit is determined by alignment accuracy and cross coupling due to the internal vibration modes (see section 2.3.

In the demonstrator, one expects the phase shift to stay within the first interference fringe. This consequently limits the differential rotation

$$\Delta\phi_R + \Phi = \pi$$

$$\Rightarrow \quad \Omega_{max} = \frac{(\pi - \Phi)\lambda_0 c_0}{2\pi L D}$$

Here, Φ are a phase constant given by the constant bias (1.8 for the stable bias, and $\frac{2\pi}{3}$ for the 3x3 demod.), and the other parameters are as defined in section 2.1.

The expected operating range is given by the requirements for the system discussed in section 2.3. The scale factor accuracy is based on the measurements (Figure 3.39 and 3.34), since there are many factors contributing to this number. The poor result here is partly caused by the calibration procedure, and this should be an area for further improvement.

4.3 Further Work

This thesis represents an early stage of a sensor development. Much work is therefore still to be done. First of all, the design chosen here is not necessarily the best suited for all applications. Other designs can be developed and different demodulation techiques can be applied.

The system had very large optical losses, especially in the fiber coils. This did not cause any serious problem in this project, since the output power from the erbium source was more than sufficient. However, if a light emitting diode (LED) is used, the output power is more limited, and the high loss can cause problems. In both cases the losses should be reduced in order to cut costs.

The system has been set up in a laboratory thus it has been possible to control most external effects. Consequently, very little signal processing has been necessary. By applying the right signal processing techiques, the system can be substantially improved, especially if the system is placed in a more “noisy” environment. This leads to the need for a more realistic testing. We have shown that the sensor system works within the boundaries set by the test equipment (particularly the DC-motor), but the limits for the system has not been fully explored. A test setup, where a larger dynamic range can be tested, and with improved accuracy, is therefore of interest.

There is also a need for developing a method for aligning the two sensors on a ship, and with the possibility for calibration on board. The calibration procedure should be improved as well, and a method here is commented in section 3.2.

Further development in components is also potentially an area for improvements.

Some fluctuations caused by change in polarization was still observed, and causes for this should be further investigated.

References

[1] Sagnac G (1913): L'ether lumineux dmontrepar l'effet du vent relatifd'ether dans un interferometre en rotation uniforme, *Comptes rendus de l'Acadmie des Sciences* **95**, 708–710.

[2] Jensen A, Taby J, Pran K, Sagvolden G, Wang G (2001): Measurement of global loads on a full scale ses vessel based on strain measurements using networks of fibre optic bragg sensors and extensive finite element analyses, *J Ship Research* **45**, 204–214.

[3] Wang G, Pran K, Sagvolden G, Havsgaard G, Jensen A, Johnsen G, Vohra S (2001): Ship hull structure monitoring using fiber optic sensors, *Smart Materials and Structures* **10**, 472–478.

[4] Mochalov A, Popov P (1999): A system for measuring deformations of large-sized objects, In: *Optical Gyros and their Application*, RTO AGARDograph 339.

[5] Saleh B, Teich M (1991): Fundamentals of Photonics, Wiley.

[6] Jin W, Culshaw B, Xu Y (1996): Multiplexing of fiber optic gyroscopes, In: *Fiber Optic Gyros: 20th Anniversary Conference*, 140–151.

[7] Lefevre H (1993): The Fibre-Optic Gyroscope, Artech House.

[8] Kråkenes K (1990): Fiber-Optic Sagnac Interferometer for Detection of Acoustic Signals, , NTH.

[9] Knudsen S (1996): Fiber-Optic Acoustic Sensors based on Michelson and Sagnac Interferometers: Responsivity and Noise Properties, , NTH.

[10] Vakoc J, Digonnet M, Kino G (1999): A novel fiber-optic sensor array based on the sagnac interferometer, *Journal of Lightwave Technology* **17**, 11.

[11] Martin J, Winkler J (1978): Fiber-optic laser gyro signal detection and processing technique, *SPIE Proceedings* **139**, 98–102.

[12] : SR850 DSP Lock-In Amplifier: Operating Manual and Programming Reference.

[13] Pavlath G, Shaw H (1982): Birefringence and polarization effects in fiber gyroscopes, *Applied Optics* **21**.

[14] Trommer G (1999): Passive all-fiber open loop gyroscope, In: *Optical Gyros and their Application*, RTO AGARDograph 339.

[15] Gottwald E, Pietzsch J (1988): Measurement method for determination of optical phase shifts in 3x3 fibre couplers, *Electronics Letters* **24**, 5.

[16] Tsao C (1992): Optical Fibre Waveguide analysis, Oxford University Press.

[17] Ezekiel S, Arditty H (1982): Fibre-Optic Rotation Sensors and Related Technologies, Springer-Verlag.

[18] Yariv A (1976): Introduction to Optical Electronics, Rinehart and Winston.

[19] Shupe D (1980): Thermally induced nonreciprocity in the fiber-optic interferometer, *Applied Optics* **19**, 5.

[20] Arditty H, Lefevre H (1981): Sagnac effect in fiber gyroscopes, *Optics Letters* **6**, 8.

[21] Post E (1967): *Review of Modern Physics* **39**.

[22] Bohm K, Petermann K, E.Weidel (1982): Sensitivity of a fiber-gyroscope to environmental magnetic fields, *Optics Letters* **7**, 180–182.

[23] Ezekiel S, Davis J, Hellwarth R (1982): Intensity dependent nonreciprocal phase shift in a fiberoptic gyroscope, *Springer Series in Optical Sciences* **32**, 332–336.

[24] M.J.Adams (1981): An introduction to Optical Waveguides, Wiley.

[25] Guillaumond D, Meunier J (2000): A novel method of gain flattening of an erbium superflourescent fibre source for fibre-optic gyroscope applications, In: *14th International Conference on Optical Fiber Sensors*.

[26] Sheem S (1980): Fiber-optic gyroscope with$[3x3]$ directional coupler, *Applied Physics Letters* **37**, 10.

[27] Sheem S (1981): Optical fiber interferometers with $[3x3]$ directional couplers: Analysis, *Jounal of Applied Physics* **52**, 6.

[28] Priest R (1982): Analysis of fiber interferometer utilizing 3x3 fiber coupler, *Journal of Quantum Electronics* **18**, 10.

[29] Derickson D (1998): Fiber Optic Test and Measurement, Prentice Hall.

[30] Lefevre H (1980): Single-mode fibre fractional wave devices and polarization controllers, *Electronics letters* **16**, 778–780.

[31] Martini G (1987): Analysis of a single-mode optical fiber piezoceramic phase modulator, *Optics ans quantum electronics* **19**, 179–190.

[32] Mochizuki K (1984): Degree of polarization in jointed fibers: the lyot depolarizer, *Applied Optics* **23**, 19.

[33] Bohm K, Petermann K, Weidel E (1983): Performance of lyot depolarizers with birefringent single-mode fibers, *Journal of Lightwave Technology* **1**, 1.

This page is intentionally left blank.

APPENDIX

A THEORY OF BASIC COMPONENTS

A.1 Sagnac Effect

The fiber optic gyroscope (FOG) utilizes the Sagnac effect [1]. In this section a heuristic derivation of the Sagnac formula will be given. The focus will be on the kinematic derivation [17], since this method is more intuitive. The electrodynamic approach is given in [20]. First the effect will be found in vacuum, and then it will be shown that the equation will be equivalent when the light propagates in a medium.

Consider the simplified interferometer where light propagates in both directions in a circular path in vacuum, Figure A.1

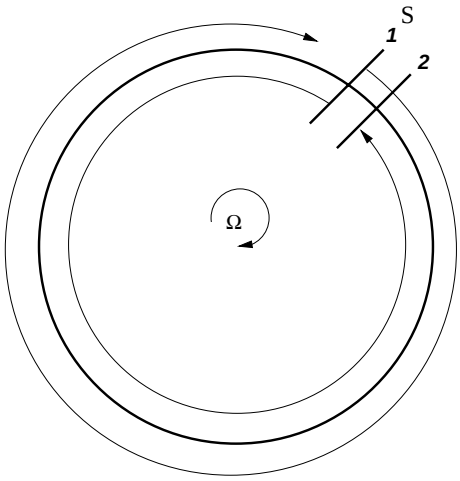

Figure A.1: Rotating disc

At point S1, there is a beamsplitter, which splits incoming ligth in two counterpropagating waves, and recombines the light when the two beams have completed one lap.

First, consider the situation when the circular path (or disc) is at rest in an inertial frame of reference. Then the two counterpropagating waves experience equal path length for every lap, and both waves travel at the speed of light in vacuum, c_0.

This gives a lap time, t_v

$$t_v = 2\pi \frac{R}{c_0} \tag{A.1}$$

where R is the radius of the disc.

If the disc is rotating with an angular velocity Ω in the clockwise direction (cw represents clockwise wave, while ccw represents counterclockwise wave) compared to an observer at rest in the inertial reference system described above, the counterclockwise wave will only have to cover the distance

$$L_{ccw} = 2\pi R - R\Omega t_{ccw} = c_{ccw} t_{ccw} \tag{A.2}$$

to complete one turn. Here $R\Omega$ is the tangential velocity and t_{ccw} is the time it takes to cover the distance L_{ccw}

On the other hand, the clockwise wave (cw) must propagate a distance

$$L_{cw} = 2\pi R + R\Omega t_{cw} = c_{cw} t_{cw} \tag{A.3}$$

to complete one lap. t_{cw} is the time the light uses to cover the distance L_{cw}. Since the light propagates in vacuum

$$c_{cw} = c_{ccw} = c_0$$

Consequently the difference in lap time for the two counterpropagating waves Δt_v is

$$\Delta t_v = t_{cw} - t_{ccw} = \frac{2\pi R}{c_0 - R\Omega} - \frac{2\pi R}{c_0 + R\Omega} \approx \frac{4\pi R^2 \Omega}{c_0^2} \tag{A.4}$$

where we have taken into account that $c_0 \gg R\Omega$. With a continous wave of frequency ω, this gives a phase difference $\Delta\phi_{Rv}$

$$\Delta\phi_{Rv} = \omega \cdot \Delta t_v = \frac{4\pi R^2 \Omega \omega}{c_0^2} = \frac{2\pi L D \Omega}{\lambda_0 c_0} \tag{A.5}$$

with L as the circumference of the disc, D the diameter of the coil, λ_0 the wavelength of the light (in vacuum).

Consider now the interferometer above put in a dielectric medium of refractive index n. If the light is propagating in a medium, the two waves will experience different velocity. We now have to use relativistic velocity in our derivations [21].

Still referring to Figure A.1, the cw and ccw speed of light become

$$c_{cw} = \frac{\frac{c_0}{n} + R\Omega}{1 + \frac{R\Omega}{n c_0^2}} = \frac{c_0}{n} + R\Omega(1 - \frac{1}{n^2}) + ...$$

$$c_{ccw} = \frac{\frac{c_0}{n} - R\Omega}{1 - \frac{R\Omega}{n c_0^2}} = \frac{c_0}{n} - R\Omega(1 - \frac{1}{n^2}) + ...$$

Thus, the difference in lap time is

$$\Delta t = t_{cw} - t_{ccw} = 2\pi R \frac{2R\Omega - (c_{cw} - c_{ccw})}{c_{cw}c_{ccw}} = 2\pi R \frac{2R\Omega - 2R\Omega(1 - \frac{1}{n^2})}{\frac{c_0^2}{n^2}} = 2\pi R \frac{2R\Omega}{c_0^2}$$

Which is independent of the properties of the medium.

In the case of the fiber gyro the circular path in Figure A.1 will consist of a fiber coil with N turns (and length L).

$$\Rightarrow \Delta t = \frac{4R^2 N}{c_0^2}\Omega = \frac{LD}{c_0^2}\Omega$$

where D is the diameter of the circular path. This produces a phase difference (non-reciprocal)

$$\Delta\phi = 2\pi \frac{\Delta t}{\lambda_0 / c_0} = \frac{2\pi LD}{\lambda_0 c_0}\Omega \tag{A.6}$$

In conclusion, the phase shift is proportional to the rotation rate. It is worth noticing that the phase shift depends on the fiber length, coil diameter and the wavelength. This makes rotation sensors built on this effect very flexible in design and dynamic range.

The sensitivity/responsivity can also be expressed in terms of the coil area and the number of turns on the coil.

$$\Delta\phi_R = \frac{8\pi N \cdot A}{\lambda_0 c_0}\Omega \tag{A.7}$$

A.2 Reciprocity

One of the main ideas and advantages of the Sagnac interferometer is that the two counterpropagating beams of light propagate in the same fiber, and consequently have traveled exactly the same lenght when the system is at rest. Ideally, external effects working on the fiber will work on both light beams and therefore give no contribution to the phase difference between the two waves. In other words, what happens to one wave will also happen to the wave propagating in the opposite direction. Some effects are nonreciprocal, dependent of the direction of the propagating light, and these effects will give a phase difference. The Sagnac effect is a truly nonreciprocal effect [17]. Other examples are magnetic phenomena, nonlinear phenomena and time varying phenomena. The latter phenomena will be dealt with at the end of this section, while magnetic and nonlinear phenomena are assumed to be neglible in this thesis [22], [23].

The reciprocity of the Sagnac interferometer will now be examined a bit closer.

Consider the simple interferometer in Figure A.2.

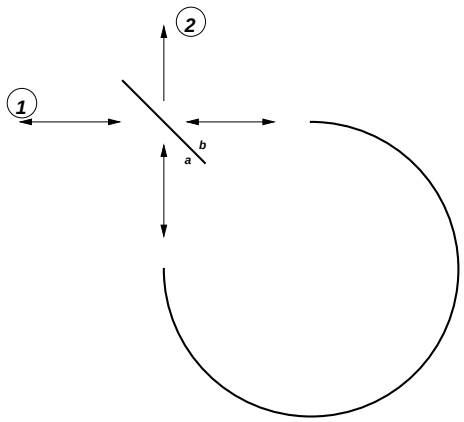

Figure A.2: A simple configuration of the Sagnac interferometer

The incoming light enters the interferometer at port 1, and the output can be detected at either port 1 or port 2. It will now be proven that port 1 is reciprocal, while port 2 is not.

The phase of the two counterpropagating waves detected at port 2 are given by (when the system is at rest)

$ccw : \phi_{ra} + \phi_l + \phi_{rb}$

$cw : \phi_t + \phi_l + \phi_t$

where ϕ_{ra} is the phase shift induced by reflection from the mirror from side a, ϕ_{rb} is the phase shift induced by reflection off the mirror from side b, ϕ_t is induced by transmission through the mirror, and ϕ_l is the phase shift from propagation through the coil. The difference $\Delta\phi$ is therefore

$$\Rightarrow \Delta\phi = \phi_{ra} + \phi_{rb} - 2\phi_t \neq 0$$

The two counterpropagating waves will experience different path lengths due to different phase shifts at the beamssplitter. On the other hand, if port 1 is investigated

$$\Delta\phi = \phi_{cw} - \phi_{ccw} = (\phi_{ra} + \phi_l + \phi_t) - (\phi_t + \phi_l + \phi_{ra}) = 0$$

Therefore, port 1 is reciprocal while port 2 is not. Adding another beamsplitter in front of port 1, a reciprocal configuration for practical use is obtained

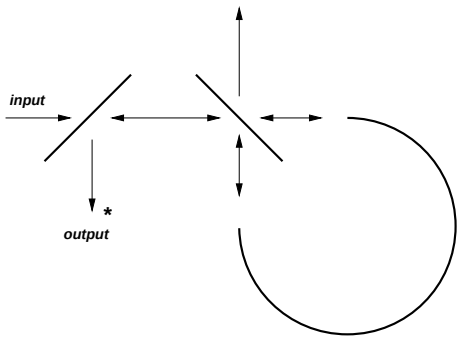

Figure A.3: Reciprocal configuration of the Sagnac interferometer

If the beamsplitter was lossless (ideal), one would obtain a phase difference of π (destructive interference) at port 2 due to conservation of energy. Even though port 2 (in Figure A.2) is not entirely reciprocal, it could still be used in the Sagnac interferometer. The use of a nonreciprocal port would only give a constant bias in the interference equation (see chapter 1.3). However, a problem arises when the properties of the coupler change with temperature, pressure, etc. Then the two counterpropagating waves will most likely be affected differently, and an error will occur. In the setup with the 3x3 coupler, a nonreciprocal port is used. The argument for using such a port is that manufacturing of couplers have advanced much, and the quality have become good enough for low to medium performance systems.

As mentioned at the beginning of this section, the only nonreciprocity one wants to measure is the Sagnac effect. Other nonreciprocal effect must consequently be avoided or substantially reduced. One important non-reciprocity is time varying parameters influencing the phase. These time varying parameters are local perturbations (varying in time) that change the phase of the light in the fiber. Many phenomena vary over time (temperature, pressure, etc.), and if the variation is fast enough, it will introduce nonreciprocal phase shifts.

A.3 Optical Fibers

Optical fibers are made of silica glass of high chemical purity. The core is doped giving an index of refraction around 1.5, slightly greater than the cladding. Light entering the core with an angle of incidence smaller than the angle of total internal reflection (determined by the index difference), is trapped within the core. Therefore, the light can propagate over large distances with minimal loss.

A brief resume of the foundation of the theory behind optical fibers will be given below. A more detailed derivation can be found in [24] and [16].

Assume the media (fiber) to be lossless and isotropic. This is not entirely true in real life, but the development of fibers has reached so far that this is a good approximation. The theory is built on Maxwell's equations, and from these equations the wave equation can be deduced. For optical fibers this equation can generally be written

$$\nabla^2 A = \epsilon\epsilon_0\mu_0\frac{\partial^2 A}{\partial t^2} \tag{A.8}$$

where A represents the electric field E or the magnetic field H. No current density nor an applied external electric field have been assumed. In polar coordinates this wave equation is written

$$\frac{1}{r}\frac{\partial}{\partial r}(r\frac{\partial A}{\partial r}) + \frac{1}{r^2}\frac{\partial^2 A}{\partial \theta^2} + \frac{\partial^2 A}{\partial z^2} = \epsilon\epsilon_0\mu_0\frac{\partial^2 A}{\partial t^2} \tag{A.9}$$

To solve this equation, one assumes that a solution exists, and that this solution is separable with respect to r, θ, z and t.

$$A = F_1(\vec{r})F_2(\theta)F_3(z)F_4(t)$$

Assume further that the z and t dependence is

$$F_3(z)F_4(t) = e^{i(\omega t - \beta z)}$$

which is valid for monochomatic waves. Here, ω is the angular frequency, and β is the wavenumber, or propagation constant, to be determined.

By also assuming the dependence

$$F_2(\theta) = e^{\pm il\theta}$$

where l is a positive integer (l=0,1,2,...) equation A.9 becomes

$$\frac{d^2F_1}{dr^2} + \frac{1}{r}\frac{dF_1}{dr} + (\beta^2 - \frac{l^2}{r^2})F_1 = 0 \tag{A.10}$$

or

$$\frac{d^2F_1}{dr^2} + \frac{1}{r}\frac{dF_1}{dr} - (\gamma^2 + \frac{l^2}{r^2})F_1 = 0 \tag{A.11}$$

depending on whether β or γ is real. Here $\beta^2 = \omega^2\mu_0\epsilon\epsilon_0 = -\gamma^2$. The first equation is the Bessel equation, while the latter is the modified Bessel equation. These equations have the solutions

$$F_1 = A_1J_l(\beta r) + A_2Y_l(\beta r) \tag{A.12}$$

$$F_1 = B_1W_l(\gamma r) + B_2K_l(\gamma r) \tag{A.13}$$

respectively. J_l, Y_l, W_l and K_l are the Bessel functions.

There can be no singularities in the core of the fiber, the solution in the cladding must be regular and zero at infinity. Moreover A (E and H) is continous at the boundary between the core and the cladding. These boundary conditions enable two solutions to be fitted. The result is

$$F_1 = AJ_l(\frac{Ur}{a}) \quad , \quad 0 < r < a \tag{A.14}$$

$$F_1 = BK_l(\frac{Wr}{a}) \quad , \quad a < r < \infty \tag{A.15}$$

where $U = a(n_1^2k_0^2 - \beta^2)^{1/2}$ and $W = a(\beta^2 - n_2^2k_0^2)^{1/2}$, and U and W satisfy the relationship $V^2 = U^2 + W^2$.

From A.14 and A.15 the eigenvalue equation can be derived

$$\frac{UJ_{l-1}(U)}{J_l(U)} = \frac{-WK_{l-1}(W)}{K_l(W)} \tag{A.16}$$

The equation is called the dispersion relation. The equation defines the confined modes, the modes that contain their energy within the core while propagating in the fiber. Light that is not propagating in one of these modes looses energy along the direction of propagation. With a given index of refraction, together with a fixed radius of the core, β, the constant of propagation is the only parameter defining the modes.

If the parameter Vdefined above, is below a certain limit ($V < 2.405$), only one mode can propagate in the fiber. The fiber is then called a single mode fiber. Such a fiber is used in the experiments described in this text.

A.4 Source

The source is a crucial part in any fiber sensor system. Extensive research and development have been carried out concerning sources in optical gyros, but they can still be the limiting factor in high performance systems. In this project, the source has not been a major issue. Well-known arguments have been used, and availablility have played a major part in deciding which source to use. Different light sources are discussed in [7] and [17]

In the early days of the interferometric fiber optic gyroscope (I-FOG) technology, monochromatic or quasi monochromatic laser sources were used. The problem encountered was unwanted interference signals. Light was reflected from splices (backreflection) and returned to the output. The reflected waves interferred with the two transmitted waves and multiple-wave interference appeared instead of the expected two-wave interference. Another problem was Rayleigh backscattering, which also produced interference patterns at the output.

Much of this “unwanted” interference was solved using a source with short coherence time, a broadband source. Because optical gyroscopes operate around zero path difference, a coherent source was not necessary. Hence, only light that has traveled almost the same lenght will interfere (a path difference smaller than the coherence length). The backreflected and backscattered light that reaches the output now only apear in the DC term. This reduces the visibility slightly, but does not degrade the signal otherwise. There is a possibility for unwanted interference if two backreflected or backscattered waves are scattered/reflected symmetrically around the half way point in the Sagnac loop. When the waves are combined at the output, they will operate within the coherence length of each other and consequently interfere. This might be a limitation in high performance gyroscopes, but will assumably not cause any problems in this project [7].

In appendix A.1 the Sagnac phase shift was introduced and shown to be

$$\Delta\phi = \frac{2\pi LD}{c_0\lambda}\Omega$$

The Sagnac phase shift thus depends on the wavelength. One obvious question is which wavelength to use. Assume that each frequency component will only interfere with its own frequency (neglecting interference with nearby frequencies) traveling in the opposite direction. This gives an interference equation [5] with the counterpropagating components with the same frequency

$$I = 1/2I_0(1 + cos(2\pi\frac{\Delta L_R}{\lambda}))$$

where the path length difference $\Delta L_R = \frac{LD\Omega}{c_0}$ is independent of the wavelength.

When no rotation is applied, all the frequency components interfere constructively, and no error is introduced. As rotation is introduced, each frequency component will give a slightly different contribution to the overall intensity. See Figure A.4

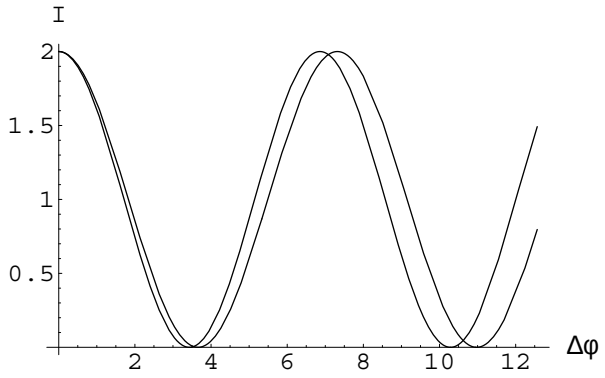

Figure A.4: Interference equation with the minimum and maximum wavelength of an Er-doped fiber amplifier

If the frequency spectrum $\sigma(\sigma = \frac{2\pi}{\lambda})$ is symmetric around a center frequency, the average intensity will be on the intensity curve of the center frequency except close to destructive interference. In this case, no error will be introduced except close to $\Delta\phi = \pi$. With larger phase differences, errors will be introduced, but this is of no concern to this project , since extended dynamic range is not an issue.

In the case of a asymmetric frequency spectrum, the intensity averaging will not coincide with the interference curve of the center frequency. An Erbium source is usually nonsymmetric with a 1530nm peak and a 1550-60 nm shoulder. One way to obtain a symmetric spectrum from a nonsymmetric source is using a stable band-limited reflector around a wavelength where the frequency spectrum is flat [25]. This makes the spectrum detected at the output symmetric.

Conclusively, an erbium source give a broadband output, and are therefore used in this project.

A.5 Coupler, polarization controller and Piezoelectric Transducer

In this section, the most important results for some of the components are summarized, and factors that are important for this project are pointed out.

A.5.1 2x2 couplers

Directional couplers are used to split and recombine light. They are usually produced by putting two fibers stripped of outer coating close together and then fusing them.

The theorectical background will not be given here, but can be found in [5]. The idea is that electromagnetic waves propagating in two waveguides close together will interact due to overlapping evanescent fields. If the waveguides are planar, the optical power after an interaction length L has been proved to be

$$P_1(L) = P_1(0)\cos^2(CL) \tag{A.17}$$

$$P_2(L) = P_1(0)\sin^2(CL) \tag{A.18}$$

Here $P_i(L)$ is the optical power in waveguide i after a length L, and C is a coupling coefficient. The point is that the split ratio ($\frac{P_1(L)}{P_2(L)}$) depends on the length of the coupling region. By ajusting the length such that $L = \frac{\pi}{2C}$, a 50/50 split is achieved, which is the desired split for optical gyro's.

A.5.2 3x3 couplers

The easiest way to describe 3x3 couplers is by using transfer matrices [26] [27]. The transfer matrix, M is given as

$$E_{out} = ME_{in}$$

where E_{in} is the electric field sent into the coupler, and E_{out} is the electric field after the coupler. For a 3x3 coupler this matrix looks like

$$M = \begin{bmatrix} a_{16}e^{j\phi_{16}} & a_{26}e^{j\phi_{26}} & a_{36}e^{j\phi_{36}} \\ a_{15}e^{j\phi_{15}} & a_{25}e^{j\phi_{25}} & a_{35}e^{j\phi_{35}} \\ a_{14}e^{j\phi_{14}} & a_{24}e^{j\phi_{24}} & a_{34}e^{j\phi_{34}} \end{bmatrix}$$

each element a_{ij} describes the amplitude coupling from arm j to i according to Figure A.5, and ϕ_{ij} the phase.

If the coupler is considered lossless, conservation of energy gives

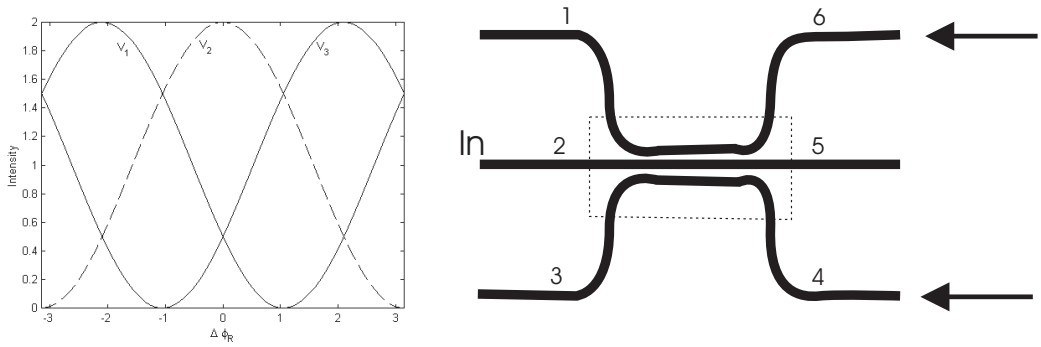

Figure A.5: Simplified illustration of a 3x3 directional coupler with interference graph for port 1 and 3

$$E_{out}^{\dagger}E_{out} = E_{out}^{\dagger}M^{\dagger}ME_{out} = E_{in}^{\dagger}E_{in}$$

The symbol † represents hermitian conjugate.

$$\Rightarrow M^{\dagger}M = I = MM^{\dagger} \tag{A.19}$$

where I is the identity matrix. Equation 2.24 can be expanded into element equations, and solved by assuming some of the coefficients to be real [28].

In an ideal lossless 3x3 coupler, the power coupling coefficients are $a_{ij}^2 = 1/3$ and the phases shifts $\Phi_{25} = \Phi_{34} = 120^o$ and $\Phi_{35} = \Phi_{24} = -120^o$. This is shown in Figure A.5. Light enters the coupler at port 4 and 6 (in phase). At port 1 and 3, the light from port 4 and 6 will interfere. The phase difference between the interfering waves will be 120^o which adds a bias to the interference equation from chapter 1.

The phase shifts are important to notice. Because of these, the use of a 3x3 coupler in a Sagnac interferometer makes the interferometer operate around its quadrature point (the point where the response is largest for the smallest rotation rates). This reduces the need for modulation, and will be examined further in section 2.2. The cost of using a 3x3 coupler instead of two 2x2 couplers in a gyroscope is loss of reciprocity.

A.5.3 Polarization controllers

A polarization controller (pc) [29] has been used in this project to make the state of polarization of the two counterpropagating waves similar at the output. The polarization controller changes the polarization within the fiber, by intruducing controlled birefringence. The pc usually consist of three coils of fiber, where one coil has twice the number of turns. By rotating the coil normal to the input and output fiber, one rotates the fast (compression) and slow (tension) axes in the coil compared to the incoming electric field. In this way, every state of polarization can be obtained. One such coil is shown in fig Figure A.6.

Points A' and B' are fixed so that a rotation of the plane of the coil induces opposite twists in the section $A'A$ and $B'B$. Compression in the fiber gives a slightly higher refractive

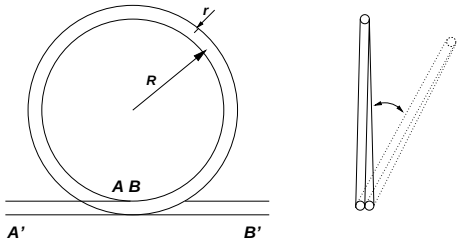

Figure A.6: Lateral and axial view of a polarization controller

index, while tension gives a slightly lower index. This changes the phase delay between the two modes (polarizations). If the fiber originally is isotropic, the change in refractive index becomes

$$\Delta n_x = \frac{n^3}{4}(p_{11} - 2\sigma_{12})(\frac{r}{R})^2 \tag{A.20}$$

$$\Delta n_y = \frac{n^3}{4}(p_{12} - \sigma_{12} - \rho p_{11})(\frac{r}{R})^2 \tag{A.21}$$

Here Δn_x is the change in refractive index in the fast axis, Δn_y is the change in the slow axis, n is the original refractive index, r is the radius of the fiber, R is the radius of the coil p_{ij} is given by the photoelastic tensor p_{ijkl}, and σ is the Poisson's ratio.

The change in refractive index given by the equations are very small, but when it is integrated over a length of fiber, the effect becomes significant. Derivation of these equation are given in [30].

By selecting the number of turns in the coil, and setting the radius of the coil correct, one can change the phase delay between two modes by π, and consequently get any specified state of polarization (SOP). Most interesting is the quarter-wave retarder $(\pi/2)$, converting linearly polarized light into left circularly light, and the half-wave retarder (π), which changes lineraly polarized light by $\pi/2$. The pc normally consist of two quarter-wave retarders and one half wave retarder. This makes it possible to change the polarization to any SOP.

A.5.4 Piezoelectric Transducer

Phase modulators are important in many fiber optic sensors. The most common fiber-optic phase modulator is called a pzt (piezoelectric transducer) [31], and consist of a piezoceramic cylinder with fiber wound around it. When voltage is applied to the cylinder, it expands or contracts proportional to the voltage. This expantion induces tension in the fiber, and this results in a phase shift as the optical path is altered.

The phase shift is usually separated in an integral (mean) phase shift and a differential phase shift. The integral phase shift $\Delta\Phi_I$ is given by

$$\Delta\Phi_I = (2\pi)^2 \frac{NCV}{\lambda}(n + (1+v)(\frac{n^3}{2})((p_{11}+p_{12})\frac{r}{2R} - p_{12})) \tag{A.22}$$

Here, N is the number of turns, C is a parameter depending on the geometry and material, V is the applied voltage, λ is the wavelength, n is the index of refraction, v is Poisson's ratio of the fiber, $p_{ij} = \frac{q_{ij}E}{1+v}$ are the strain-optic constants, r is the fiber radius, and R is the radius of the pzt without voltage applied.

The integral phase shift is measured when an unpolarized light source is used. The differential phase shift on the other hand is associated with the fiber birefringence and is given by

$$\Delta\Phi_D = (2\pi)^2 \frac{NCV}{\lambda}(1+v)n^3(p_{11} - p_{12})\frac{r}{R} \tag{A.23}$$

Usually the integral phase shift is much larger than the differential. For derivation of these equations, see [31].

A.6 Jones matrix representation of a Lyot Depolarizer

One promising way to handle the polarization problem in fiber-optical gyroscopes is to use depolarized light [32], [33].

The Lyot depolarizer changes the different spectral components in polarized light from the input to the output in such a way that averaged over the spectrum, the light appears unpolarized. It consists of two highly birefringent fibers with length ratio 2:1, and spliced to each other at an angle of 45^o compared to the principal axis.

First, consider a single linearly birefringent fiber. The complex optical field amplitudes of the two polarization eigenstates are denoted A_x and A_y, and propagation constants β_x and β_y. The propagation in a lossless birefringent fiber can then be described by

$$\frac{dA_x}{dz} + j\beta_x A_x = j\kappa(z)A_y \tag{A.24}$$

$$\frac{dA_y}{dz} + j\beta_y A_y = j\kappa^*(z)A_x \tag{A.25}$$

where $\kappa(z)$ is the random coupling coefficient, z is the direction of propagation, and * denotes complex conjugation [33]. Assume the random coupling coefficient to be much smaller than the propagation constants $|\kappa(z)| \ll \beta_x, \beta_y$. Here, $\kappa = 0$ gives the zeroth order approximation

$$A_x(z) = A_x(0)e^{-j\beta_x z}$$

$$A_y(z) = A_y(0)e^{-j\beta_y z}$$

By inserting these equations into the right hand side of Eq. A.24 and A.25 and integrating, the first order approximation is obtained

$$A_x(z) = e^{-j\beta_x z}\left[A_x(0) + jA_y(0)\int_0^z \kappa(z')e^{j(\beta_x-\beta_y)z'}dz'\right]$$

$$A_y(z) = e^{-j\beta_y z}\left[A_y(0) + jA_x(0)\int_0^z \kappa(z')e^{-j(\beta_x-\beta_y)z'}dz'\right]$$

This gives the Jones matrix $\underline{\underline{M}}$ of a linearly birefringent fiber

$$\underline{\underline{M}} = e^{-j\overline{\varphi}}\begin{bmatrix} e^{-j\delta z'} & j\int_0^{z'}\kappa(z)e^{2j\delta z - j\delta z'}dz' \\ j\int_0^{z'}\kappa^*(z)e^{-2j\delta z + j\delta z'}dz' & e^{j\delta z'} \end{bmatrix} \tag{A.26}$$

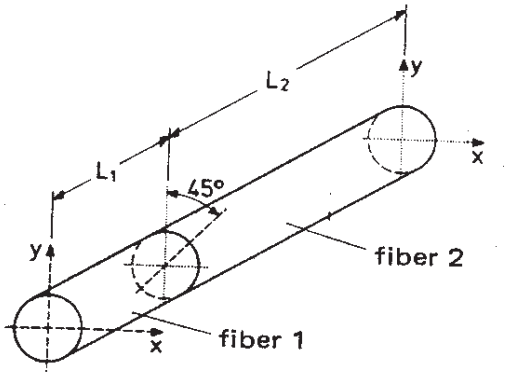

Figure A.7: Lyot depolarizer with coordinate system

where $\delta = \frac{1}{2}(\beta_x - \beta_y)$ and $\overline{\varphi} = \frac{1}{2}(\beta_x + \beta_y)z'$

The Jones vector theory now states that the polarization after a lenght L is the polarization at $z = 0$ times the Jones matrix $\underline{\underline{M}}$ of the system, in this case the birefringent fiber

$$\vec{A}(z = L) = \underline{\underline{M}}(z' = L)\vec{A}(z = 0)$$

where $\vec{A} = \begin{bmatrix} A_x \\ A_y \end{bmatrix}$ represents the two eigenstates of the polarisation.

A fiber optic depolarizer is shown in Figure A.7 and can be descibed by the Jones matrix $\underline{\underline{M}}_D$

$$\underline{\underline{M}}_D = \begin{bmatrix} m_{11} & m_{12} \\ m_{21} & m_{22} \end{bmatrix} = \underline{\underline{M}}_2 \cdot \underline{\underline{R}} \cdot \underline{\underline{M}}_1 \tag{A.27}$$

where $\underline{\underline{M}}_1$ and $\underline{\underline{M}}_2$ represents fiber 1 and 2 respectively, and $\underline{\underline{R}}$ describes the rotation of 45^o

$$\underline{\underline{R}} = \frac{1}{\sqrt{2}} \begin{bmatrix} 1 & 1 \\ -1 & 1 \end{bmatrix} \tag{A.28}$$

Inserting Eq. A.26 and A.28 into Eq. A.27 the coefficients of $\underline{\underline{M}}_D$ becomes

$$\sqrt{2}m_{11} = e^{-j\Delta^+} + je^{-j\Delta^-}K_1^* - je^{-j\Delta^+}K_2$$
$$\sqrt{2}m_{12} = e^{-j\Delta^-} + je^{-j\Delta^+}K_1 + je^{-j\Delta^-}K_2$$
$$\sqrt{2}m_{21} = -e^{-j\Delta^-} + je^{j\Delta^+}K_1^* + je^{j\Delta^-}K_2^*$$
$$\sqrt{2}m_{22} = e^{j\Delta^-} - je^{j\Delta^-}K_1 + je^{j\Delta^+}K_2^*$$

with

$$K_1 = \int_0^{L_1} \kappa_1(z) e^{2j\delta_1 z} dz$$

$$K_2 = \int_0^{L_2} \kappa_2(z) e^{2j\delta_2 z} dz$$

and

$$\Delta^+ = \delta_2 L_2 + \delta_1 L_1$$

$$\Delta^- = \delta_2 L_2 - \delta_1 L_1$$

To obtain depolarized light, one must require

$$\overline{|m_{11}|^2} = \overline{|m_{12}|^2} = \overline{|m_{21}|^2} = \overline{|m_{22}|^2} = \frac{1}{2}$$

and

$$\overline{m_{ij} m_{nm}^* = 0} \quad for \quad ij \neq nm$$

without polarization coupling, these requirements are fullfilled if

$$|\frac{d\Delta^+}{d\sigma}|, |\frac{d\Delta^-}{d\sigma}|, |\frac{d(\Delta^- \pm \Delta^+)}{d\sigma}| \gg \tau_c \tag{A.29}$$

where σ is the spectral frequency. This equation states that the polarization dispersion in the two fiber lenghts, and the difference between the polarization dispersion in the fibers should significantly exceed τ_c, the coherence time of the light. To meet this requirement of short coherence time, a broadband source must be used.

In the case of polarization coupling, Eq. A.29 is not sufficient for perfect depolarisation. To analyse the problem, a somewhat arbitrary parameter is defined

$$\epsilon = \frac{\overline{|m_{11}|^2} - 1/2}{\overline{|m_{11}|^2}} \simeq 2\overline{|m_{11}|^2} - 1 \tag{A.30}$$

The ϵ approximately corresponds to the relative amount of light that is still polarized after propagating through the depolarizer.

$$\epsilon = -2Re\{j \int_{\sigma} \left[\int_0^{L_2} \kappa_2 e^{2j\delta_2 z} dz - \int_0^{L_2} \kappa e^{-2j\delta_1 x} \right] S(\sigma) d\sigma\} \tag{A.31}$$

with $x = L_1 - z$ and $S(\sigma)$ normalized spectral intensity distribution of the light source. A Lorentzian spectrum will be assumed in the following. This spectrum is symmetric, and are consequently not an ideal model for the erbium source. However, the use of a Lorentian spectrum simplifies the discussion, and at low power output, the erbium source used in the experiments was relatively symmetric.

$$S(\sigma) = \frac{2\tau_c/\pi}{1 + (\sigma - \sigma_c)^2 (2\tau_c)^2} \tag{A.32}$$

where $S(\sigma)$ is the normalized spectral intensity distribution ($\int S(\sigma) d\sigma = 1$), σ is the angular frequency $\sigma = \frac{2\pi c}{\lambda}$, σ_c is the center emission frequency, τ_c the coherence time ($\tau = \frac{1}{\Delta\sigma}$, with $\Delta\sigma$ the spectral width at full width at half max).

Assume the two fibers to be cut from the same fiber, $\delta_1 = \delta_2 = \delta$. Expanded around the center frequency

$$\delta = \delta_0 + \frac{\Delta\tau}{2}(\sigma - \sigma_c)$$

Performing the integration yields

$$\epsilon = -2Re\{j \int_0^{L_2} \kappa_2 e^{2j\delta_0 z} e^{-\Delta\tau z/2\tau_c} dz - j \int_0^{L_1} \kappa_1 e^{-2j\delta_0 x} e^{-\Delta\tau x/2\tau_c} dx\}$$

To perform the two integrals, an assumption is made

$$e^{-\Delta\tau x/2\tau_c} \approx \{ \begin{array}{ll} 1 & for \Delta\tau x < 2\tau_c \\ 0 & for \Delta\tau x \geq 2\tau_c \end{array}$$

This simplifies the equation to

$$\epsilon = -2Re\{j \int_0^{l_c} \kappa_2 e^{2j\delta_0 z} dz - j \int_0^{l_c} \kappa_1 e^{-2j\delta_0 x} dx\} \tag{A.33}$$

with $l_c = 2\tau/\delta\tau$.

Here, ϵ is random since the polarisation coupling is random, and κ_1 and κ_2 are uncorrelated. This gives

$$\epsilon_{rms} = \sqrt{< \epsilon^2 >} = 2\sqrt{h \cdot l_c} = 2\sqrt{2h\tau_c/\Delta\tau} \tag{A.34}$$

where

$$h = \frac{1}{L} < | \int_0^L \kappa(z) e^{2j\delta z} dz|^2 >$$

is called a polarization-holding parameter. $<>$ denotes averaging. Equation A.34 states that the relative amount ϵ_{rms} of intensity which is still polarized at the output is proportional to the square root of the polarization coupling during the lenght L_c.

B CALCULATION OF TWO INTERFERING GYROSCOPES

This appendix contains the computation reffered to in section 2.1. Consider the the waves to be monochromatic, and with complex amplitudes:

$$U_{1a} = A(r)e^{-i\Phi_{1a}}$$

$$U_{2a} = A(r)e^{-i\Phi_{2a}}$$

$$U_{1b} = A(r)e^{-i\Phi_{1b}+\theta}$$

$$U_{2b} = A(r)e^{-i\Phi_{2b}+\theta}$$

Here are Φ_{1i} the wave propagating in clockwise direction in gyroscope i, and Φ_{2i} the counterclockwise wave. θ is the phase difference caused by a different pathlength between the gyroscope B and the 2x2 coupler that combines the signal from the two gyroscopes, compared to gyroscope A.

The interference signal at the output is given by:

$$I_{tot} = |U_{1a} + U_{2a} + U_{1b} + U_{2b}|^2 = (U_{1a} + U_{2a} + U_{1b} + U_{2b})(U_{1a}^* + U_{2a}^* + U_{1b}^* + U_{2b}^*)$$

$$I_{tot} = A^2 + A^2e^{-i(\Phi_{1a}-\Phi_{2a})} + A^2e^{-i(\Phi_{1a}-\Phi_{1b}-\theta)} + A^2e^{-i(\Phi_{1a}-\Phi_{2b}-\theta)} + A^2e^{-i(\Phi_{2a}-\Phi_{1a})}$$
$$+A^2 + A^2e^{-i(\Phi_{2a}-\Phi_{1b}-\theta)} + A^2e^{-i(\Phi_{2a}-\Phi_{2b}-\theta)} + A^2e^{-i(\Phi_{1b}+\theta-\Phi_{1a})} + A^2e^{-i(\Phi_{1b}+\theta-\Phi_{2a})}$$
$$+A^2 + A^2e^{-i(\Phi_{1b}-\Phi_{2b})} + A^2e^{-i(\Phi_{2b}+\theta-\Phi_{1a})} + A^2e^{-i(\Phi_{2b}+\theta-\Phi_{2a})} + A^2e^{-i(\Phi_{2b}-\Phi_{1b})} + A^2$$

$$I_{tot} = A^2(4 + (e^{-i(\Phi_{1a}-\Phi_{2a})} + e^{i(\Phi_{1a}-\Phi_{2a})})$$
$$+(e^{-i(\Phi_{1b}-\Phi_{1a}+\theta)} + e^{i(\Phi_{1b}-\Phi_{1a}+\theta)})$$
$$+(e^{-i(\Phi_{1a}-\Phi_{2b}-\theta)} + e^{i(\Phi_{1a}-\Phi_{2b}-\theta)})$$
$$+(e^{-i(\Phi_{1b}-\Phi_{2a}+\theta)} + e^{i(\Phi_{1b}-\Phi_{2a}+\theta)})$$
$$+(e^{-i(\Phi_{2a}-\Phi_{2b}-\theta)} + e^{i(\Phi_{2a}-\Phi_{2b}-\theta)})$$
$$+(e^{-i(\Phi_{1b}-\Phi_{2b})} + e^{i(\Phi_{1b}-\Phi_{2b})}))$$

By using the identity $e^{-ix} + e^{ix} = 2cos(x)$ and setting

$$\Phi_{1b} - \Phi_{2b} = \Delta\phi_c + \Delta\phi_d$$

$$\Phi_{1b} - \Phi_{2a} = \Delta\phi_c + \frac{\Delta\phi_d}{2}$$
$$\Phi_{1b} - \Phi_{1a} = \frac{\Delta\phi_d}{2}$$
$$\Phi_{1a} - \Phi_{2a} = \Delta\phi_c$$
$$\Phi_{1a} - \Phi_{2b} = \Delta\phi_c + \frac{\Delta\phi_d}{2}$$
$$\Phi_{2a} - \Phi_{2b} = \frac{\Delta\phi_d}{2}$$

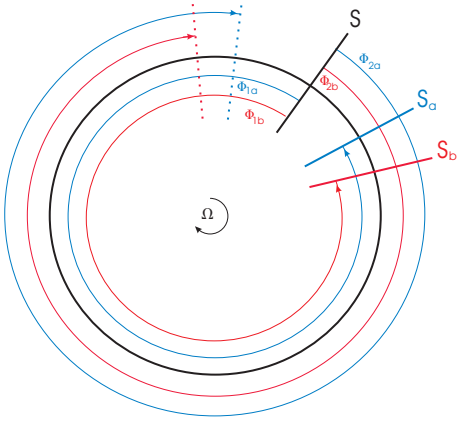

Figure B.1:

according to Figure B.1. Here is $\Delta\phi_c$ the sagnac phasedifference due to common rotation in the two gyroscopes, while ϕ_d is the phasedifference due to different rotation. This gives

$$I_{tot} = A^2(4 + 2cos(\Delta\phi_c) + 2cos(\frac{\Delta\phi_d}{2} + \theta) + 2cos(\Delta\phi_c + \frac{\Delta\phi_d}{2} - \theta) + 2cos(\Delta\phi_c + \frac{\Delta\phi_d}{2} + \theta)$$
$$+2cos(\frac{\Delta\phi_d}{2} - \theta) + 2cos(\Delta\phi_c + \Delta\phi_d))$$

To split the different phases one uses the identity
$cos(x+y) = cos(x)cos(y) - sin(x)sin(y)$ and $cos(x-y) = cos(x)cos(y) + sin(x)sin(y)$

$$I_{tot} = A^2(4 + 2cos(\Delta\phi_c) + 2cos(\frac{\Delta\phi_d}{2}cos(\theta) - 2sin((\frac{\Delta\phi_d}{2}sin(\theta) + 2cos(\Delta\phi_c + \frac{\Delta\phi_d}{2}cos(\theta))$$
$$+2sin(\Delta\phi_c + \frac{\Delta\phi_d}{2})sin(\theta) + 2cos(\Delta\phi_c + \frac{\Delta\phi_d}{2})cos(\theta) - 2sin(\Delta\phi_c + \frac{\Delta\phi_d}{2})sin(\theta)$$
$$+2cos(\frac{\Delta\phi_d}{2})cos(\theta) + 2sin(\frac{Delta\phi_d}{2})sin(\theta) + 2cos(\Delta\phi_c)cos(\Delta\phi_d) - 2sin(\Delta\phi_c)sin(\Delta\phi_d))$$

$$I_{tot} = A^2(4 + 2cos(\Delta\phi_c) + 4cos(\frac{\Delta\phi_d}{2}cos(\theta) + 4cos(\Delta\phi_c + \frac{\Delta\phi_d}{2})cos(\theta)$$
$$+2cos(\Delta\phi_c)cos(\Delta\phi_d) - 2sin(\Delta\phi_c)sin(\Delta\phi_d)$$

B.1 LabView program for 3x3 demodulation

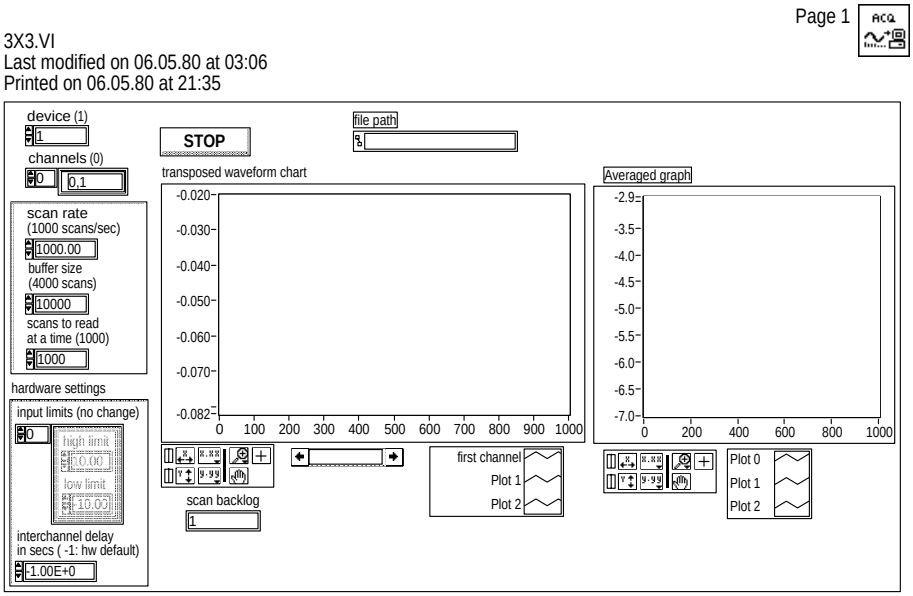

Figure B.2: Front panel of the 3x3 demodulation LabView program

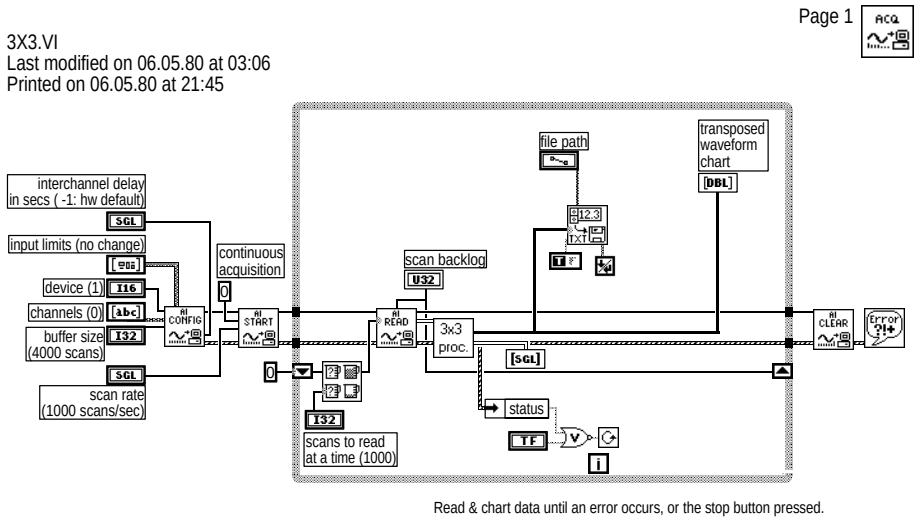

Figure B.3: Diagram of the 3x3 demodulation LabView program

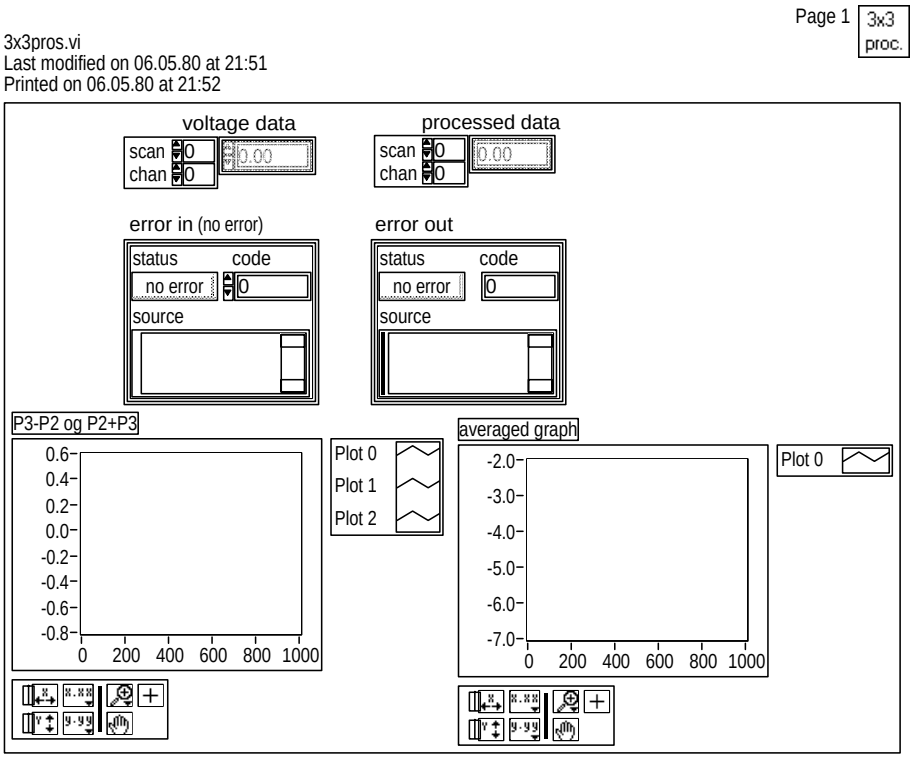

Figure B.4: Front panel of the 3x3 processing subVI of the LabView program

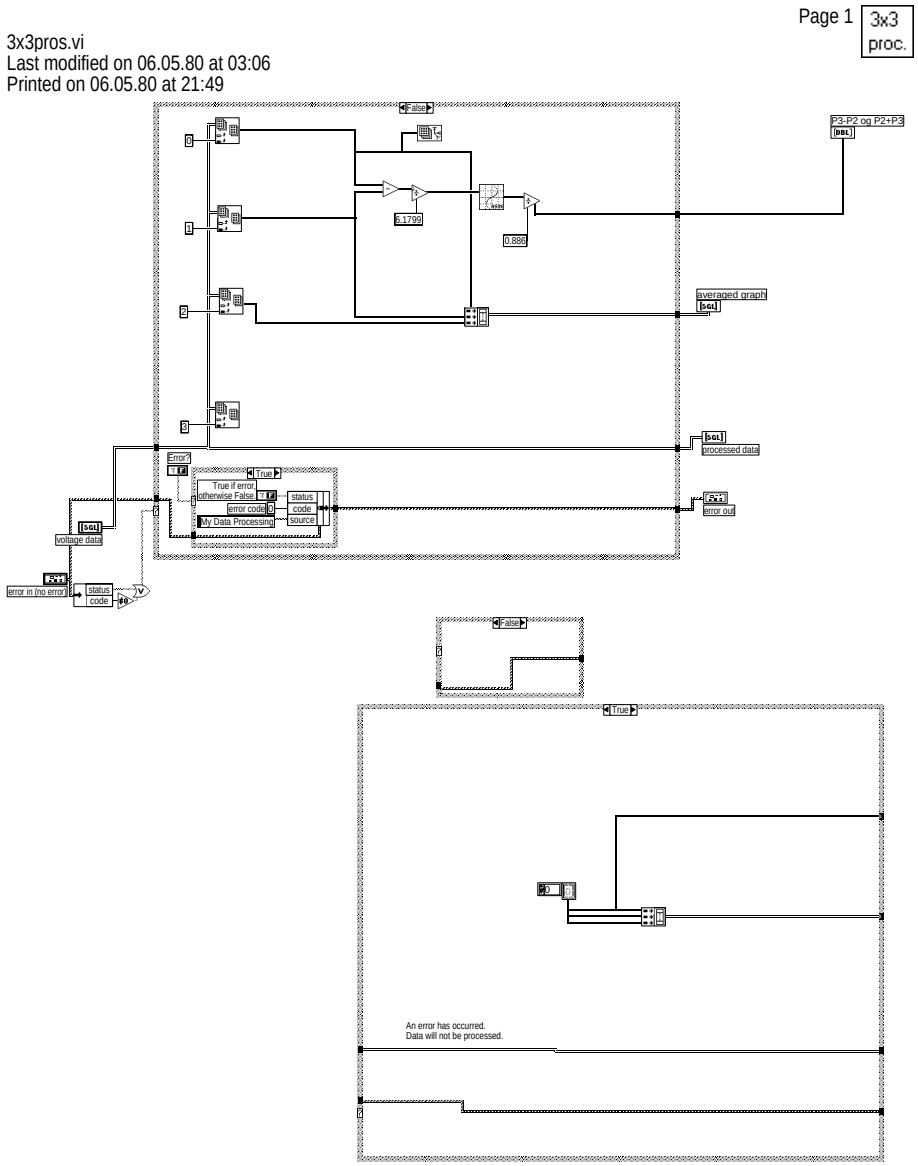

Figure B.5: Diagram of the 3x3 processing subVI LabView program

C DRAWING OF SPOOL

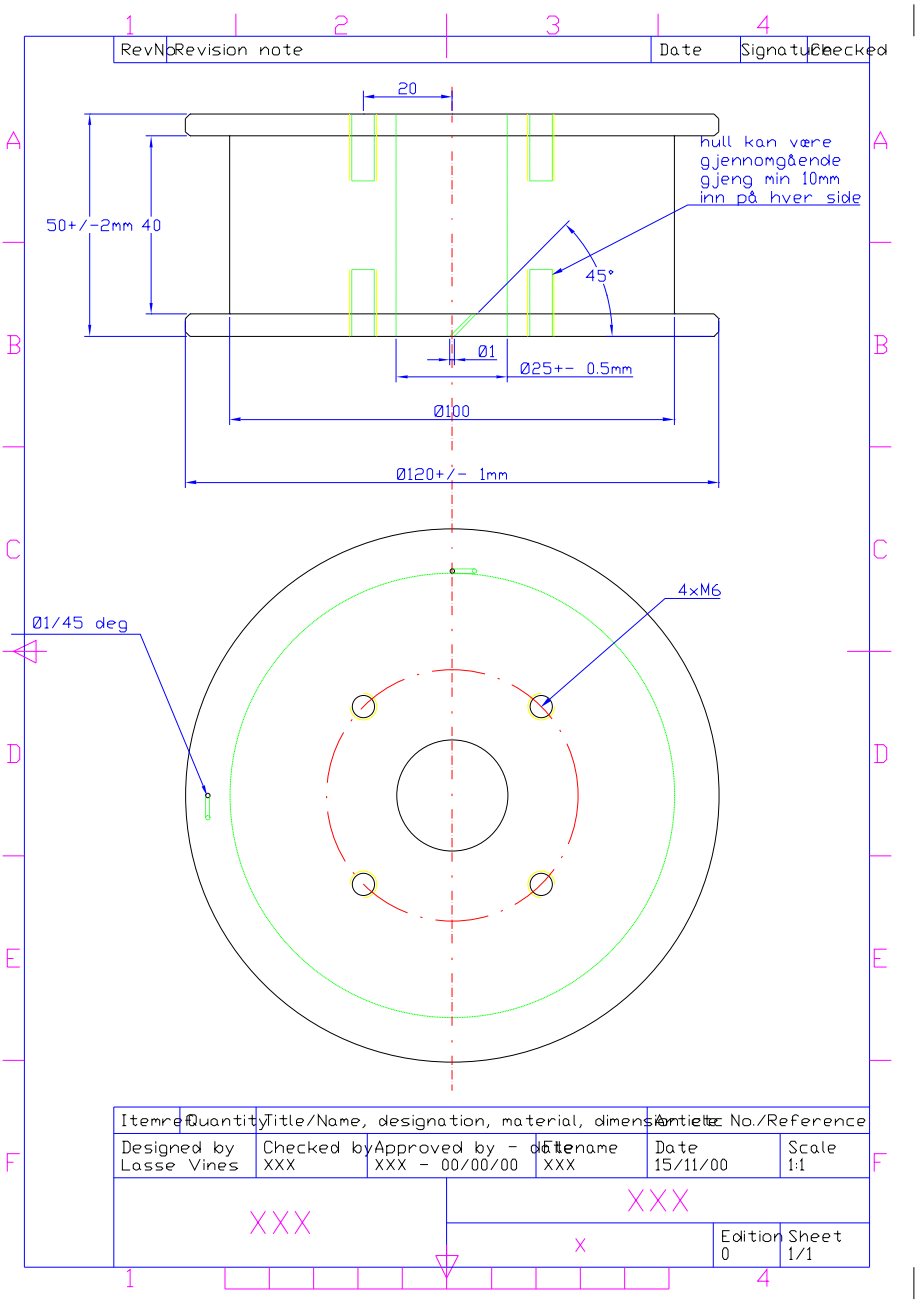

Figure C.1: Drawing of the spool for production

D LABVIEW PROGRAM FOR MONITORING AND DEMODULATION

D.1 LabView program used in Stable bias modulation/demodulation

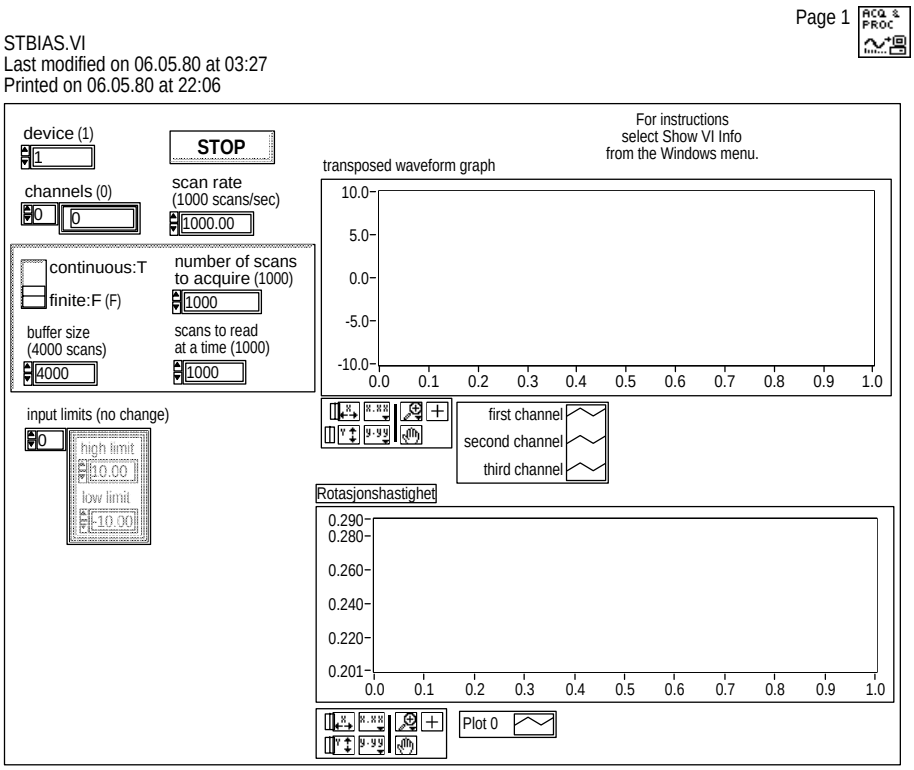

Figure D.1: Front panel of the stable bias LabView program

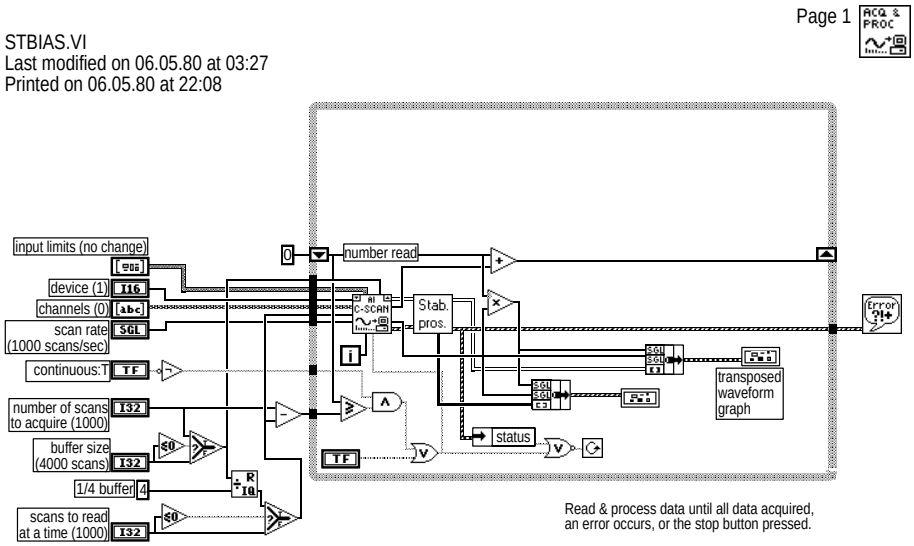

Figure D.2: Diagram of the stable bias LabView program

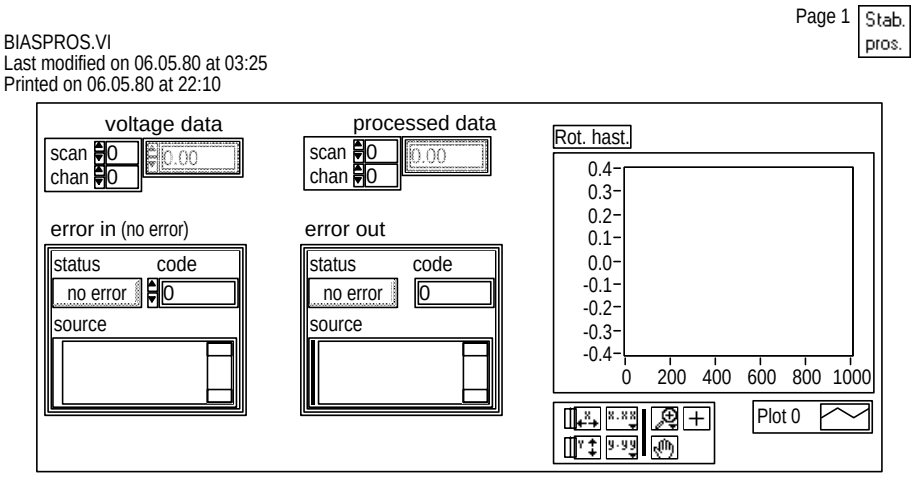

Figure D.3: Front panel of the processing subVI of the stable bias LabView program

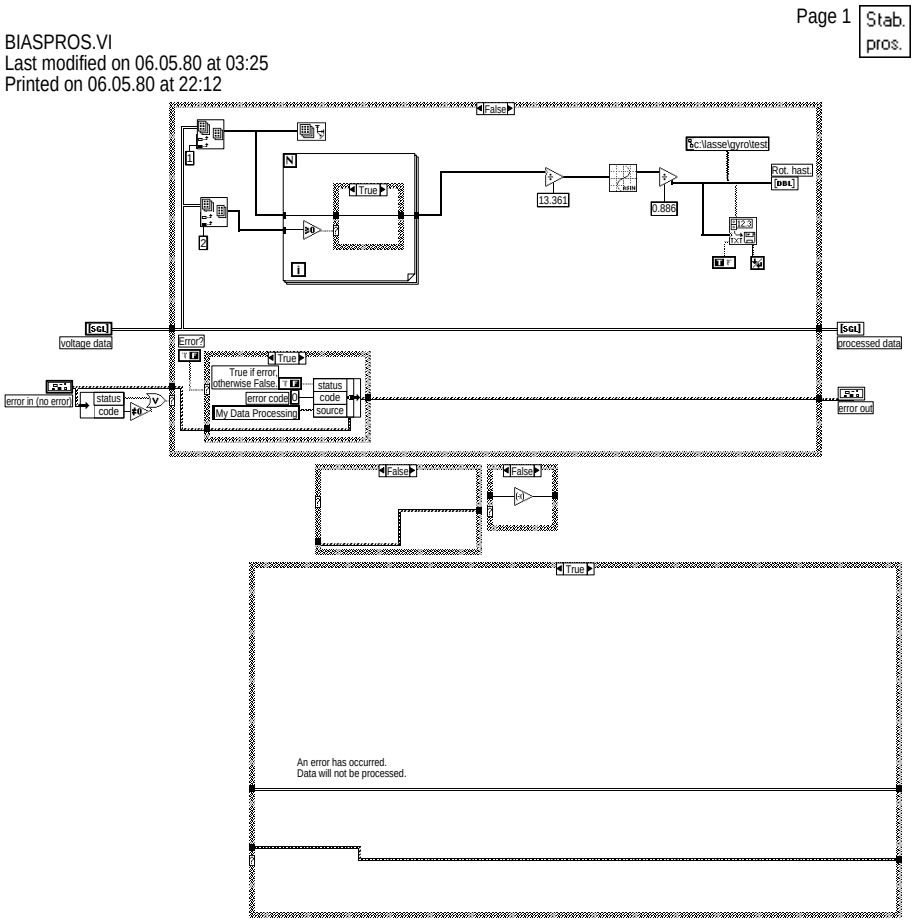

Figure D.4: Diagram of the processing subVI of the stable bias LabView program

This page is intentionally left blank.

DISTRIBUTION LIST

FFIE **Dato:** 22nd January 2002

RAPPORT TYPE (KRYSS AV)	RAPPORT NR	REFERANSE	RAPPORTENS DATO
X RAPP ☐ NOTAT ☐ RR	2001/05899	FFIE/793/116	22nd January 2002
RAPPORTENS BESKYTTELSESGRAD		ANTALL EKS UTSTEDT	ANTALL SIDER
unclassified		43	107
RAPPORTENS TITTEL		FORFATTER(E)	
Sagnac Interferometer for Differential Rotation Rate Measurement		Lasse Vines	
FORDELINGEN GODKJENT AV FORSKNINGSSJEF:		FORDELINGEN GODKJENT AV AVDELINGSSJEF:	

EKSTERN FORDELING

ANTALL	EKS NR	TIL

INTERN FORDELING

ANTALL	EKS NR	TIL
14		FFI-Bibl
1		Adm direktør/stabssjef
1		FFIE
1		FFISYS
1		FFIBM
3		Gunnar Wang,FFIE
1		Øystein Farsund,FFIE
1		Karianne Pran,FFIE
1		Geir Sagvolden,FFIE
1		Hans Erling Torkildsen,FFIE
1		Atle Skaugen,FFIE
1		Svein Jarle Haugland,FFIBM
4		Lasse Vines,FFIE
6		Arkiv-FFIE
6		Arkiv-FFIBM
0		FFI-veven

Retningslinjer for fordeling og forsendelse er gitt i Oraklet, Bind I, Bestemmelser om publikasjoner for Forsvarets forskningsinstitutt, pkt 2 og 5. Benytt ny side om nødvendig